

*Liquid crystal phase behaviour
of colloidal platelets
in external fields*



David van der Beek

Omslag:

Brownse beweging, door Janneke Huisman (oliepastel op papier, augustus 2002)

ISBN 90-393-0296-0

Liquid crystal phase behaviour of colloidal platelets in external fields

Vloeibaar kristallijn fasegedrag van
colloïdale plaatjes in externe velden

(met een samenvatting in het Nederlands)

Proefschrift ter verkrijging van de graad van doctor aan de Universiteit Utrecht op gezag van de Rector Magnificus, Prof. dr. W.H. Gispen, ingevolge het besluit van het College voor Promoties in het openbaar te verdedigen op maandag 4 april 2005 des middags te 4.15 uur

door

David van der Beek

geboren op 7 december 1976, te Sleeuwijk



Universiteit Utrecht

Promotor

Prof. dr. Henk N.W. Lekkerkerker
verbonden aan de sectie Fysische en Colloïdchemie,
Faculteit Scheikunde, Universiteit Utrecht

Co-promotoren

Dr. P. Davidson
verbonden aan het Laboratoire de Physique des Solides,
Faculté des Sciences, Université Paris-Sud XI, France

Dr. A.V. Petukhov

en

Dr. G.J. Vroege
beiden verbonden aan de sectie Fysische en Colloïdchemie,
Faculteit Scheikunde, Universiteit Utrecht



Nederlandse Organisatie voor Wetenschappelijk Onderzoek

The work described in this thesis is supported by the Council for Chemical Science (CW) with financial support from the Netherlands Organisation for Scientific Research (NWO).

Sol iustitiae illustra nos
zinspreuk van de Universiteit Utrecht

Maar voor u, die mijn naam vreest, zal de zon der gerechtigheid opgaan.
Maleachi 4:2

This thesis is based on the following publications:

Chapter 2

Evidence of the hexagonal columnar liquid crystal phase of hard colloidal platelets by high resolution SAXS

D. van der Beek, A.V. Petukhov, S.M. Oversteegen, G.J. Vroege, and H.N.W.

Lekkerkerker

accepted for publication in the European Physical Journal E

Chapter 3

Gravity-induced liquid crystal phase transitions of colloidal platelets

D. van der Beek, T. Schilling, and H.N.W. Lekkerkerker

Journal of Chemical Physics, **121**, 5423-5426 (2004)

Chapter 4

Small-angle X-ray scattering study of the magnetic-field-induced orientational order in the isotropic phase of colloidal gibbsite platelets

D. van der Beek, A.V. Petukhov, H.H. Wensink, G.J. Vroege, P. Davidson, W. Bras, and H.N.W. Lekkerkerker

to be published

Chapter 5

Magnetic birefringence study of the isotropic phase of suspensions of colloidal gibbsite platelets

D. van der Beek, P. Davidson, J. Ferré, J.P. Jamet, and H.N.W. Lekkerkerker

to be published

Chapter 6

Magnetic-field-induced shift of the isotropic-nematic phase transition in a suspension of colloidal gibbsite platelets

D. van der Beek, H.H. Wensink, G.J. Vroege, and H.N.W. Lekkerkerker

to be published in extended form

Chapter 7

The Frederiks transition in a nematic phase of colloidal gibbsite platelets

D. van der Beek, P. Davidson, and H.N.W. Lekkerkerker

to be published in extended form

Chapter 8

Liquid crystalline phases of charged colloidal platelets

D. van der Beek and H.N.W. Lekkerkerker

Langmuir, **20**, 8582-8586 (2004)

and

Nematic ordering vs. gelation in suspensions of charged colloidal platelets

D. van der Beek and H.N.W. Lekkerkerker

Europhysics Letters, **61**, 702-707 (2003)

Chapter 9

Formation of a columnar phase of charged colloidal platelets in a centrifugal field

D. van der Beek, P. Radstake, A.V. Petukhov, and H.N.W. Lekkerkerker

to be published

Other papers by the author:

Observation of a hexatic columnar liquid crystal of polydisperse colloidal disks

A.V. Petukhov, D. van der Beek, R.P.A. Dullens, I.P. Dolbnya, G.J. Vroege, and H.N.W. Lekkerkerker

submitted to the Proceedings of the National Academy of Sciences

Preparation and properties of polyamide-6-boehmite nanocomposites

C. Özdilek, K. Kazimierczak, D. van der Beek, and S.J. Picken

Polymer, **45**, 5207-5214 (2004)

Isotropic-nematic phase separation in suspensions of polydisperse colloidal platelets

F.M. van der Kooij, D. van der Beek, and H.N.W. Lekkerkerker

Journal of Physical Chemistry B, **105**, 1696-1700 (2001)

Contents

Chapter 1	General introduction	11
Part I	A closer look on the liquid crystal phases of a suspension of sterically stabilised colloidal gibbsite platelets, using a morphological and gravitational field	15
Chapter 2	Evidence of the hexagonal columnar liquid crystal phase of hard colloidal platelets by high resolution SAXS	17
Chapter 3	Gravity-induced liquid crystal phase transitions of hard colloidal platelets	27
Part II	Sterically stabilised colloidal gibbsite platelets in an external magnetic field	37
Chapter 4	Small-angle X-ray scattering study of the magnetic-field-induced orientational order in the isotropic phase of colloidal gibbsite platelets	39
Chapter 5	Magnetic birefringence study of the isotropic phase of colloidal gibbsite platelets	61
Chapter 6	Magnetic-field-induced shift of the isotropic-nematic phase transition of colloidal gibbsite platelets	73
Chapter 7	The Frederiks transition in a nematic phase of colloidal gibbsite platelets	81
Part III	Liquid crystal phases in a suspension of charged colloidal gibbsite platelets and the influence of a gravitational and centrifugal field	93
Chapter 8	Liquid crystal phases in a suspension of charged colloidal platelets	95

Chapter 9	Formation of a columnar phase of charged colloidal platelets in a centrifugal field	107
References		117
Summary		127
Samenvatting		129
Colour versions of selected figures		131
Enkele gedachten achteraf		141
Curriculum Vitae		143

1

General introduction

1.1 Colloidal particles and suspensions

Colloidal particles and suspensions abound in our world. Examples that we may encounter in everyday life are the shampoo we use to wash our hair, the milk we drink at breakfast, the clouds or fog that we see outside, the clay of which much of the Dutch soil is composed, the magnetic particles that cover the hard disk in our computers, the latex paints we apply to our homes' walls, the toothpaste we use to clean our teeth, and so on. The feature that these examples share is the size of the particles that they are composed of. This size is in the range of 0.000001 to 0.001 millimetre, or, more conveniently, from about 1 nm to about 1 μm . The term 'colloidal' refers to any particle, irrespective of its chemical composition or shape, that has at least one dimension in this range. In the examples above, the colloidal particles are insoluble and finely dispersed in a solvent, hence, such mixtures are called dispersions or suspensions. Milk is in fact a very special case because it consists of three colloidal species, *i.e.*, fat globules of about 1 μm , casein micelles that are a factor 10 smaller, 100 nm, and whey proteins that are only 3 nm in size. The main constituent of milk, however, is water, in which those particles are dispersed and which makes up more than 90% of the volume. Due to their specific surface chemistry, the colloidal particles do not aggregate or coalesce, at least they should not before the sell-by date. On prolonged standing, the milk goes bad and due to the acidification, the particles form large aggregates that settle on the bottom. In this way, the colloidal properties are completely lost. Obviously, when studying colloidal dispersions for their colloidal properties, this

Chapter 1

emphasises the need to somehow prevent aggregation. While the term ‘colloid’ defines a particle’s size, in the following we will see that the shape of a colloidal particle influences its macroscopic behaviour drastically.

1.2 Shape matters

It has been known for a long time that colloidal dispersions are ideal model systems, which, under certain conditions, closely resemble atomic systems. At the beginning of the previous century, Nobel prize laureate Jean Baptiste Perrin found that dilute suspensions of colloidal spheres showed sedimentation behaviour similar to that of a dilute (near-ideal) molecular gas. The observed concentration profile was very well described by the barometric height distribution [1,2]. Interestingly, from his measurements he was able to obtain Avogadro’s number.

At higher particle concentrations, the similarity between colloids and atoms remains. Colloidal spheres, interacting through a so-called hard potential, display a fluid to crystal phase transition on increasing concentration [3,4]. When the spheres are somehow rendered attractive, they display colloidal gas, liquid and solid (or crystal) phases, analogous to ordinary atomic or molecular substances [5,6]. This correspondence allows for a study of the underlying principles of matter in general on timescales that, due to the relatively large colloidal size, are much more convenient than the atomic timescales.

In the 1920s and 1930s, it was found that suspensions of anisotropic colloidal particles, *i.e.*, plates [7] and rods [8,9], displayed a transition from an isotropic (I) to a nematic (N) phase. The isotropic phase is the equivalent of the fluid phase of spheres, where there is no long-range orientational or positional order. The nematic phase is in fact a liquid crystal without long-range positional order but which does possess long-range orientational order. Only a decade after the abovementioned observations and actually inspired by them, Lars Onsager recognised that the nature of I-N transition lies in the anisotropic shape of the particles [10,11]. In particular, he demonstrated that the stability of the nematic phase can be explained on a purely entropic basis by considering the competition between orientational entropy (favouring the isotropic state) and the entropy of excluded volume (which favours the nematic state). As the latter becomes more important at higher concentrations, a first order phase transition from an isotropic to a nematic phase may occur if the concentration of plates or rods is sufficiently high. Thus, even plates and rods with only a hard-core interaction may form a nematic phase. This notion has been confirmed by computer simulations [12-16] and experimental studies [17-28].

In addition to the I-N transition, it was found that rod-like colloids show the nematic to smectic-A phase transition [19,29-33]. The smectic-A phase consists of stacked layers of rods, with a liquid-like in-plane order and a one-dimensional crystalline stacking of the planes. A detailed description of this phase transition came with theory [34-40] and computer simulations [41-43], showing that again hard-core interactions are enough to

induce such ordering. From computer simulations by Veerman and Frenkel [13] and later Zhang and co-workers [44], it was found that hard disks may also form another liquid crystal phase, namely the orientationally and two-dimensionally translationally ordered columnar (C) phase. This phase has also been observed experimentally in suspensions of sterically stabilised and charged colloidal plates [45-48]. Theory has proven to be useful in the understanding of the columnar phase as well [49].

Summarising, hard plate- and rod-like particles show phase behaviour that, due to their anisotropic shape, is richer and more complex than that of hard spheres. The (liquid crystal) phase behaviour of plate- and rod-like colloidal particles is by now rather well understood, which opens up the question as to how such systems behave in external fields.

1.3 Scope of this thesis

A logical prerequisite in the study of colloids in external fields is a firm understanding of the equilibrium behaviour of the particles in the absence of a field. As will be evident from the previous section, this is the case for plate-like colloids and therefore we attempt to study the phase behaviour of colloidal plates in external fields. Especially in view of the liquid crystal character of such suspensions this may be interesting.

In Part I and II of this thesis, we make use of suspensions of sterically stabilised colloidal gibbsite ($\text{Al}(\text{OH})_3$) platelets that have been developed at the Van 't Hoff laboratory [22,50]. In a recent study of this suspension, the isotropic, nematic, and columnar phases were reported [45]. However, there is one issue that was not resolved. Van der Kooij and co-workers argued that they observed a columnar phase, based on the presence of three peaks in the small-angle X-ray scattering patterns, but they noted the absence of a fourth peak that should also have been present. In Chapter 2 of this thesis, we prepared an aligned columnar phase by using the influence of the sample walls (a morphological field). This allowed us to obtain conclusive evidence for the identity of the columnar phase, making the basis of knowledge of the equilibrium behaviour complete. In Chapter 3, we study the effect of a gravitational field on the suspension and find three phases (I, N and C) at the same time. We describe our results with a simple osmotic compression model.

Part II is devoted to the study of our colloidal gibbsite suspensions in a magnetic field. In Chapters 4 and 5, we study the magnetic-field-induced alignment of the isotropic phase using small-angle X-ray scattering and birefringence measurements, respectively. From these, we are able to obtain an estimate of the diamagnetic susceptibility anisotropy of the platelets. Chapter 6 addresses the issue of the shift of the I-N phase transition in a magnetic field. In Chapter 7, we use both a magnetic and a morphological field to study the Frederiks transition in the nematic phase of our suspension. This allowed the first measurement of an elastic constant in a liquid crystal of colloidal plates.

In the last part of this thesis, Part III, we develop a new model system, *i.e.*, a suspension of charged colloidal gibbsite platelets. In Chapter 8, we study the equilibrium phase behaviour

Chapter 1

of this system. Because ordinary ways to concentrate our suspensions fail, we use a gravitational field to sample the concentration range under consideration. We find that in spite of the soft electrostatic interaction potential the particles behave as hard platelets in showing the isotropic, nematic, and columnar phase. Chapter 9 presents a short study of the charged gibbsite platelets in a centrifugal field of 900 G. Due to the relatively fast settling of the particles, sedimentation equilibrium may not have been reached. Still, we find a sediment with columnar order.

Part I

**A closer look on the liquid crystal phases of
a suspension of sterically stabilised colloidal
gibbsite platelets, using a morphological
and gravitational field**

2

Evidence of the hexagonal columnar liquid crystal phase of hard colloidal platelets by high resolution SAXS

Abstract

We report small-angle X-ray scattering (SAXS) measurements of the columnar phase of hard colloidal gibbsite platelets. We have been able to create large oriented domains of the columnar phase both perpendicular and parallel to the sample wall, varying the volume fraction of platelets and adding non-adsorbing polymer to the dispersion. In conjunction with the increased resolution of the SAXS-setup, this allowed a detailed analysis of the columnar phase, providing unambiguous evidence for the hexagonal nature of the phase.

2.1 Introduction

It has long been known that dispersions of anisotropic colloids display liquid crystal phases. The earliest reports date back to the 1920s and 1930s, when suspensions of rod- and plate-like colloids were found to exhibit the isotropic (I) to nematic (N) phase transition. Some notable examples include ribbon-like vanadium pentoxide (V_2O_5) [8] and rod-like tobacco mosaic virus [9] particles and plate-like clay particles observed by Langmuir [7] in 1938.

In retrospect, observing the I-N transition in suspensions of rod- and plate-like colloids is not very surprising. Already in the 1940s, just a few years after the mentioned experiments

Chapter 2

and actually inspired by them, Lars Onsager proposed an explanation for the I-N transition on purely entropic grounds [10,11]: the competition between packing entropy (which favours the nematic state) and orientational entropy (favouring the isotropic state) determines the I-N phase behaviour. As the packing entropy becomes more important at higher volume fractions, the particles tend to align and form a nematic phase at high enough concentration. Onsager also showed that particle shape alone is enough to induce such behaviour. Thus, even hard rods or plates without any interaction may form a nematic phase. This notion has been confirmed by computer simulations [12-16], and since the seminal work of Onsager there have been quite a few experimental studies of hard and charged rod- [17-21,23-25,28] and plate-like [22,26,27] particles (see also Chapter 8) that also corroborate that idea.

From computer simulations by Veerman and Frenkel [13], and later Zhang and co-workers [44], it was found that hard platelets may also form another liquid crystal phase, namely the orientationally and 2D translationally ordered columnar (C) phase. This phase has been observed experimentally in suspensions of sterically stabilised [45] and charged [46,47] colloidal plates.

Although the behaviour of hard platelets is now rather well understood, there is an interesting issue, raised in one of these reports [51] that is related to the inherent size polydispersity in these synthetic suspensions of platelets: it is quite surprising that such systems, with a rather high polydispersity of up to 25%, show the columnar liquid crystal phase. In contrast, crystallisation of hard spheres is suspected to be frustrated due to the so-called terminal polydispersity, with proposed values of 5% to 12% [52-56]. Nevertheless, on the basis of their small-angle X-ray scattering (SAXS) data, van der Kooij and co-workers [45] argue that the observed high-density liquid crystal phase is most likely a hexagonal columnar phase. Their argument for a hexagonal packing of the columns is founded on the observation of three low-angle scattering peaks within the powder pattern. However, they noted the absence of a fourth low-angle peak that should also be present in the scattering pattern of a hexagonal structure. Conclusive evidence would require sufficiently large monodomains with columns perpendicular to the sample wall, revealing scattering patterns with a six-fold symmetry corresponding to hexagonal packing. Usually, oriented samples are prepared by applying an external field, *e.g.* magnetic fields [57-61] (see also Chapter 7) and shear flow [62-64]. Previously, we have been able to prepare large crystals of hard colloidal *spheres* for SAXS studies [65,66] using non-adsorbing polymer as a depleting agent. In this chapter we follow the same scheme and use sterically stabilised colloidal gibbsite platelets with non-adsorbing polymer. This resulted in columnar crystals with a much better signal-to-noise ratio compared to the previous study [45]. In addition, the depletion interaction is expected to favour a perpendicular orientation of the columns with respect to the sample walls. Due to these improvements, we have been able to resolve the missing scattering peak. Our results show that we indeed could prepare large oriented domains of columnar phase, allowing us to demonstrate its hexagonal columnar nature.

2.2 Experiment

We synthesised hexagonal colloidal gibbsite ($\text{Al}(\text{OH})_3$) platelets [50] that were subsequently grafted with an end-functionalised polyisobutene and suspended in toluene to obtain a model system of hard platelets [22,45]. Transmission electron microscopy (TEM), see Fig. 2.1, and atomic force microscopy were used to determine the average corner-to-corner diameter, D , and thickness, L , of the dry particle core, although the latter might contain a contribution of the collapsed steric stabiliser. The diameter distribution is also shown in Fig. 2.1. We found $\langle D \rangle = 232$ nm and $\langle L \rangle = 13$ nm and a polydispersity of $\sigma = 20\%$ in both dimensions. In solution the thickness of the sterically stabilizing polyisobutene brush is an estimated 2 to 3 nm. This gives us effective dimensions of $D_{\text{eff}} = 237$ nm and $L_{\text{eff}} = 18$ nm.

We prepared several samples of this dispersion with effective volume fractions ranging from 0.37 to 0.40 both with and without non-adsorbing polymer (polydimethylsiloxane, $M_w \approx 423$ kDa and $R_g \approx 33$ nm [67]). The samples were thoroughly homogenised and subsequently put in flat capillaries (internal dimensions 0.3×3.0 mm²), after which they were put away to phase separate. Within a few days, phase separation was complete and yielded multiple phase equilibria [67]. Each sample at least exhibited nematic and columnar phases. Furthermore, Bragg reflections became visible, already hinting at the presence of a columnar phase. On a timescale of months, these colours got quite bright and distinct; see Fig. 2.2. We were not able to detect a change in the colour in time. The reflections allowed us to get an estimate of the hexagonal lattice spacing using Bragg's

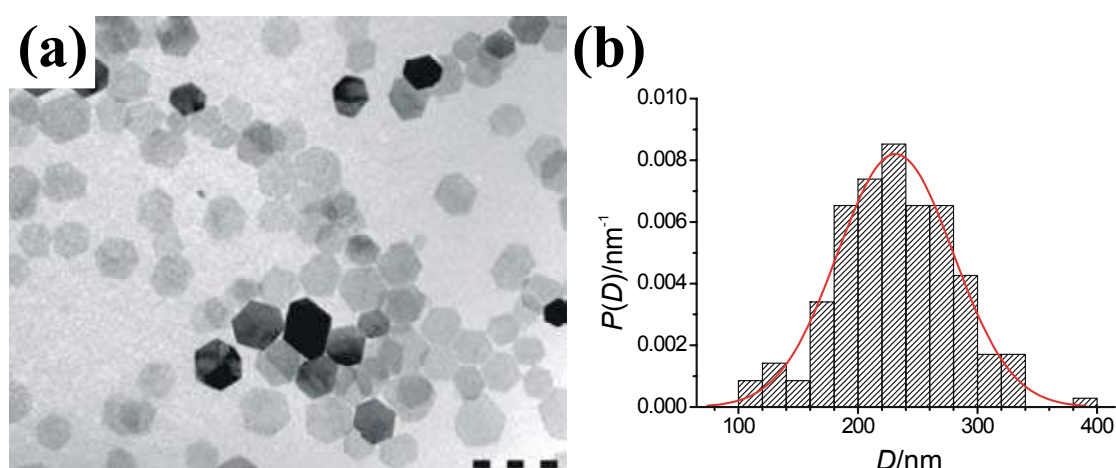


Figure 2.1 – (a) shows a Transmission electron micrograph of the colloidal gibbsite platelets; the scale bar denotes 500 nm. (b) depicts the normalised diameter distribution of the colloidal gibbsite platelets used in this study, together with a Gaussian fit. From the fit, we obtain $\langle D \rangle = 232$ nm and $\sigma = 20\%$, based on 176 platelets measured.

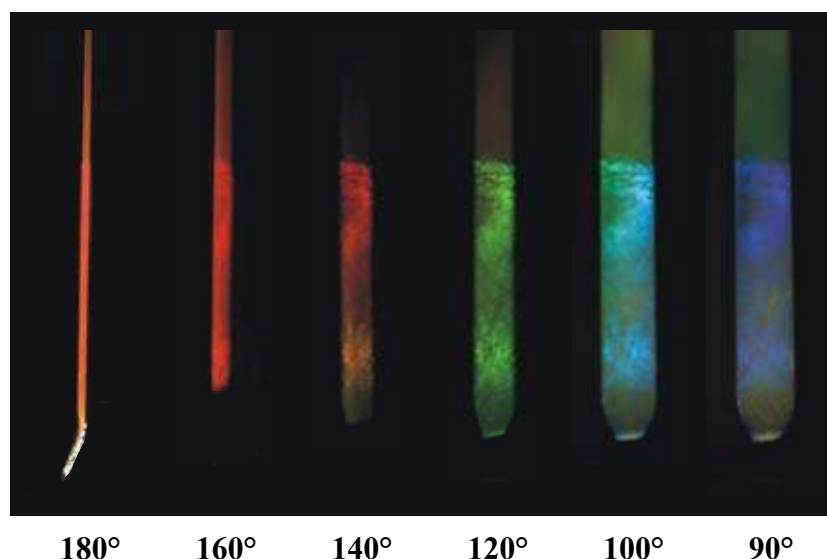


Figure 2.2 – Bragg reflections from the columnar phase of sample C. The upper part of the sample is a nematic phase in equilibrium with the columnar phase. The colour of the reflections (red through blue) varies with the incident Bragg angle 2Θ . The reflections already hint at the presence of a columnar structure and allow making an estimate of the inter-columnar spacing as $\langle d_{(100)} \rangle = 215 \pm 15$ nm, see Table 2.2. Close inspection of the nematic phase reveals a red colour (two most left photographs), indicative of the structure factor peak at about the same position as the $d_{(100)}$ -maximum in the columnar phase. (See colour version at page 131.)

law.

From the set of samples, three representative samples (hereafter called A, B, and C) were selected for analysis with SAXS. The sample details are given in Table 2.1. We used the recently developed [68] high-resolution SAXS setup of the Dutch-Belgian beamline BM-26 DUBBLE at the European Synchrotron Radiation Facility (ESRF, Grenoble, France). One of the challenges in the application of SAXS to our suspensions of colloidal platelets is related to the existence of two distinctly different spatial scales. Due to the small particle thickness, the face-to-face interparticle structure leads to scattering at relatively large angles. On the other hand, due to the relatively large particle diameter, the side-to-side

Table 2.1 – Details of the samples used in this study. Here, age is the time between sample preparation and measurement of the SAXS patterns, ϕ denotes the volume fraction of the platelets and c_{pol} is the polymer concentration.

sample	age/d	ϕ	$c_{pol}/\text{g l}^{-1}$
A	16	0.40	0.0
B	8	0.37	0.0
C	3	0.37	0.8

structure results in scattering at very small angles, requiring a high reciprocal-space resolution. To achieve the latter, the X-ray beam was carefully focused at the position of the X-ray detector consisting of a phosphor screen coupled to a 16-bit CCD camera (Photonic Science) with a pixel size of 22 μm . In order to increase the maximum accessible q -value, a relatively high X-ray energy of 18 keV ($\lambda = 0.69 \text{ \AA}$) and a shorter sample-detector distance (about 5 m) were used. In addition, the detector and beam stop were mounted off-centre to maximise the q -range even further. These settings allowed us to achieve a resolution of 0.003 nm^{-1} (the full-width-at-half-maximum of the instrument function), which is at least 3 times higher than before [45]. The smallest accessible scattering angle corresponded to $q_{\min} = 0.023 \text{ nm}^{-1}$. The maximum q values were about $q_{\max,h} = 0.4 \text{ nm}^{-1}$ in the horizontal plane and $q_{\max,v} = 0.24 \text{ nm}^{-1}$ in the vertical direction.

2.3 Results and discussion

As a first experiment, we measured the hexagonal lattice spacing $d_{(100)}$ using a simple Bragg experiment. Sample C was immersed in a cylindrical glass flask, filled with toluene to reduce optical reflections. We illuminated the sample with white light at Bragg-angles ranging from $2\Theta = 90$ to 180° and recorded images Nikon Coolpix 995 digital camera, as shown in Fig. 2.2. Table 2.2 lists the results and the calculated $d_{(100)}$ lattice spacings. We obtain an average of $\langle d_{(100)} \rangle = 215 \pm 15 \text{ nm}$ and a resulting inter-columnar spacing $a_D = 248 \pm 17 \text{ nm}$, which agrees reasonably with value obtained in the SAXS experiment.

Table 2.2 – The $d_{(100)}$ lattice spacings as obtained from the simple Bragg experiment; see Fig. 2.2. Using Bragg’s law, $2nd \sin \Theta = \lambda$, with a refractive index of $n \approx 1.5$, we find $\langle d_{(100)} \rangle = 215 \pm 15 \text{ nm}$ and a resulting inter-columnar spacing $a_D = 248 \pm 17 \text{ nm}$, which agrees reasonably with the more sophisticated SAXS experiment; see Table 2.3.

$2\Theta/^\circ$	colour	λ/nm	$d_{(100)}/\text{nm}$	a_D/nm
160	red	650	220	254
140	orange	600	212	245
120	green	550	212	245
100	cyan	500	218	252
90	blue	450	212	245

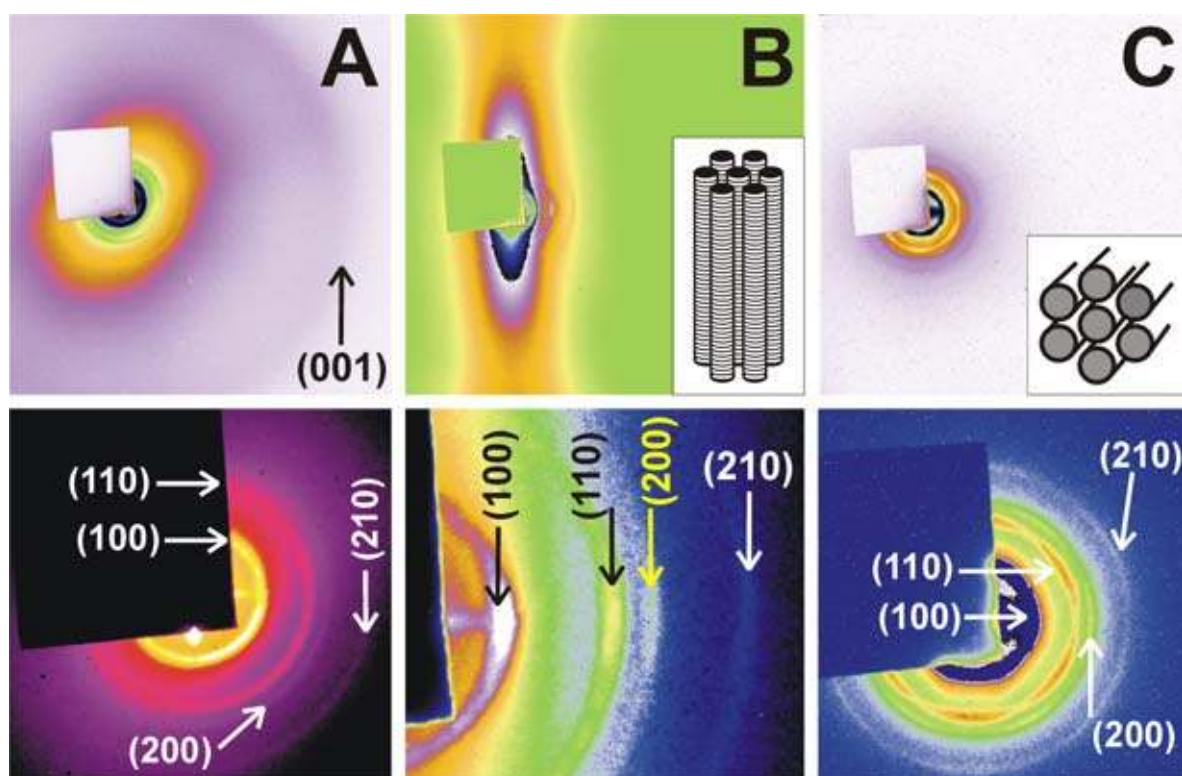


Figure 2.3 – SAXS patterns obtained in the columnar phase of samples A, B and C, along with the assigned Miller indices. The upper panels depict the entire SAXS patterns, while the lower panels present the magnified views of the small scattering angle regions near the beam-stop. Sample A yields ring-like diffraction features typical for diffraction from a powder. In contrast, samples B and C show strong predominant orientation of the columns, either along the vertical direction (in B) or along the X-ray beam (in C), as shown by the inserted sketches. The hexagonal pattern in C points to the presence of the hexagonal columnar phase. (See colour version at page 132.)

In Fig. 2.3, we show the obtained SAXS patterns for samples A to C. In the following we will index the reflections using Miller indices (hkl). For a hexagonal packing we expect reflections perpendicular to the columns with $q_{(hk0)}$ proportional to $\sqrt{h^2 + hk + k^2}$, while we use l to indicate (liquid-like) order within the columns. Sample A shows the characteristics expected for a columnar phase, *i.e.*, four scattering peaks with q -ratios of $1:\sqrt{3}:\sqrt{4}:\sqrt{7}$ at small angles and a much broader, liquid-like peak at large angle. The small-angle inter-columnar peaks have an apparent width of 0.003 nm^{-1} , determined by the instrument's resolution. The large-angle intra-columnar peak has a full width at half maximum of about 0.07 nm^{-1} . The ring-like features are typical for diffraction from a powder, hence, the domains of columnar phase must be much smaller than the irradiated volume ($300 \times 300 \times 300 \mu\text{m}^3$). We attribute the small domains to the relatively high volume fraction that causes fast crystallisation yielding small crystallites [69]. Sample B shows the columnar scattering peaks more clearly than sample A. In this case the scattering is dominated by a larger

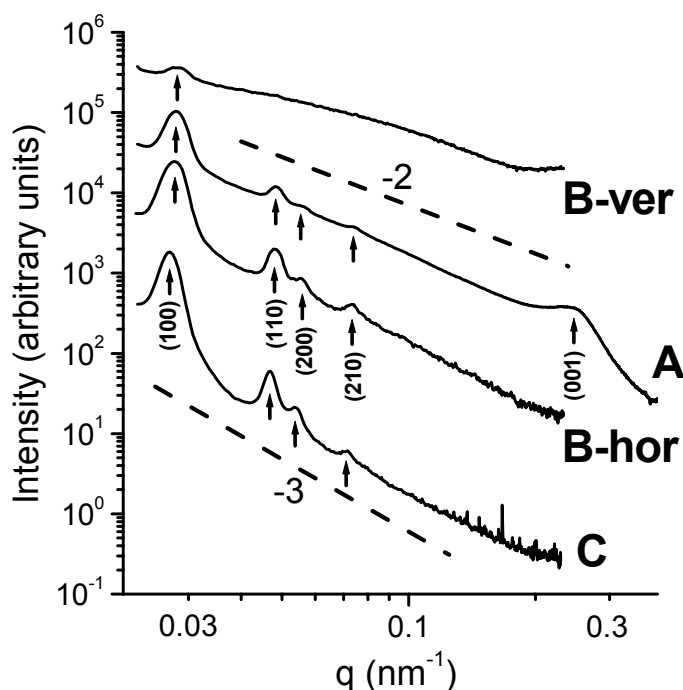


Figure 2.4 – Averaged radial intensity profiles of the SAXS patterns. The profiles of sample B were obtained from small (about 5-pixel wide) horizontal (B-hor) and vertical (B-ver) slices, while A and C are azimuthal averages over the whole available detector area except for the part covered by the beamstop (the same mask is used for both A and C). The curves are shifted vertically for clarity. The dashed lines present the power law decays ($I \propto q^n$) with $n = -2$ and $n = -3$.

single domain, likely due to slower crystallisation and higher mobility at the lower volume fraction involved. The domain has vertically-oriented columns, as illustrated in the inset in panel B. The liquid-like (001) and (00-1) peaks are located outside the detector area, but they were visible in similar samples with skewed orientations. In sample C we find a single domain with columns directed perpendicularly to the wall and we observe a hexagonal scattering pattern due to inter-columnar scattering. Here the presence of non-adsorbing polymer is found to favour the face-to-wall anchoring of the gibbsite platelets, which can be understood by the stronger depletion attraction in this configuration. We also note that in the azimuthal direction the inter-columnar Bragg peaks are broad, of the order of 30° . This suggests a significant spread of the crystal orientations.

From the SAXS patterns, we calculated averaged radial intensity profiles that are depicted in Fig. 2.4. Due to the improved resolution of the SAXS-setup, the inter-columnar (100), (110), (200) and (210) reflections are clearly resolved. Yet, we are not able to resolve the intrinsic width of the Bragg peaks. In addition, in samples B and C we benefit from the predominant orientation of the columnar domains that enhances the visibility of the inter-columnar reflections. This is due to an increase of the intensity of the reflections themselves and to faster decay of the background scattering intensity I_{sc} at q values from

Chapter 2

$q_{(100)}$ to $q_{(001)}$. The behaviour of the background can be understood by taking into account the anisotropy of the scattering of a single particle, *i.e.*, the form factor $F(\vec{q})$. For disk-like particles it can be factorised as $F(\vec{q}) = F_{\parallel}(q_{\parallel}) \times F_{\perp}(\vec{q}_{\perp})$, where q_{\parallel} and \vec{q}_{\perp} are the components of the scattering vector parallel and perpendicular to the platelet normal, respectively. In the q -range of interest ($q_{(100)}$ to $q_{(001)}$) the first factor $F_{\parallel}(q_{\parallel})$ does not decay appreciably, while the second one decays as $F_{\perp}(\vec{q}_{\perp}) \propto |\vec{q}_{\perp}|^{-3}$. (This feature is also used in Chapter 4, where we analyse the scattering of platelets in a magnetic field.) Thus, the strongest scattering is observed for small q_{\perp} , when the scattering vector \vec{q} is nearly perpendicular to the platelets. In sample C this strong contribution is absent since the scattering vector \vec{q} is almost parallel to the platelets, so $q \approx q_{\perp}$. As one can see in Fig. 2.4, the background intensity indeed closely follows power law decay $I_{sc}(q) \propto q^n$ with exponent $n = -3$, arising from the decay of F_{\perp} . In contrast, in sample A, the particles have all possible orientations including those with $q \approx q_{\parallel}$, which give the main contribution to the background. Averaging over all possible orientations leads to a power law decay with a smaller exponent $n = -2$. We have observed similar power-law decay with $n = -2$ in a dilute isotropic suspension (not shown). In sample B, both phenomena are visible – the background scattering intensity along the columns (perpendicular to the platelets, vertical direction) is much stronger and decays slower than parallel to the platelets (horizontal direction).

We further note that, although the diffraction in sample B is dominated by a domain with vertically oriented columns, other orientations are also present, as deduced from the observation that the columnar reflections form rings, albeit with well-pronounced maxima in the horizontal direction. Also, the maxima of the (100), (110), and (210) reflections in the same direction suggest a spread in the orientations of the hexagons formed by neighbouring columns. In contrast, sample C shows long-range bond orientational order leading to a well-pronounced hexagonal pattern. Furthermore, the q^{-3} -decay of the background also indicates the existence of one single domain within the irradiated volume in sample C.

From the averaged radial intensity profiles we find the characteristic spacings as listed in Table 2.3. The intra-columnar spacings are calculated using the relation $a_D = \frac{4}{3} \pi \sqrt{3} \sqrt{h^2 + hk + k^2} / q_{(hk0)}$, while the average intra-columnar distance between the platelets is defined as $a_L = 2\pi / q_{(001)}$. Although samples A and B differ in overall platelet volume fraction, due to the first order character of the nematic-columnar transition, the volume fractions of their columnar phases are the same. This explains their corresponding a_D . Sample C on the other hand contains non-adsorbing polymer, which enhances size

Evidence of the columnar phase of hard colloidal platelets by high resolution SAXS

Table 2.3 – Measured q -values of the scattering in the columnar phase obtained from the radial profiles of the SAXS patterns, as well as the inter- and intra-columnar spacings a_D , respectively, a_L , as calculated from the q -values.

sample	$q_{(100)}/\text{nm}^{-1}$	$q_{(110)}/\text{nm}^{-1}$	$q_{(200)}/\text{nm}^{-1}$	$q_{(210)}/\text{nm}^{-1}$	$q_{(001)}/\text{nm}^{-1}$
A	0.0282	0.0486	0.0561	0.0745	0.25
B	0.0281	0.0482	0.0551	0.0741	-
C	0.0272	0.0470	0.0541	0.0717	-
	a_D/nm				a_L/nm
A	257	259	259	258	25
B	258	261	263	259	-
C	267	267	268	268	-

fractionation between the coexisting phases [67,70], resulting in a higher average particle diameter in the columnar phase and hence a larger columnar spacing.

The formation of columnar crystals in our samples is actually quite surprising, considering the high polydispersity of our platelets. In general, phase separating colloidal systems, of spheres [56,71-73] or platelets [14,67,70,74], deal with this by fractionation of the particles between the phases, leading to sub phases with a smaller polydispersity than the parent suspension. In sample C, where non-adsorbing polymer enhances fractionation even more, this lowering of the polydispersity facilitates the formation of the single columnar crystal. In addition to phase fractionation, there is the possibility of local fractionation, which is likely to take place in sample A due to its being a powder. Local fractionation leads to crystals within the columnar phase having a different average particle diameter (hence slightly different periods) and a slightly lower polydispersity each. However, in sample C, which contains a (large) single domain, such local fractionation is much more difficult as it would require the particles to travel too large distances (at least 1000 times their own diameter).

The $q_{(hko)}$ -values for samples A, B, and C correspond to nearest-neighbour-distances of 257 nm, 260 nm, and 268 nm, respectively. From the histogram (of the parent suspension) it is immediately clear that at least 21% of the particles do not fit into a columnar phase with these spacings. For sample C, where size fractionation is strongest, the average particle diameter is larger than the parent's average, making accommodation of the particles in the columnar phase even more difficult.

Detailed analysis of the scattering peaks in patterns of the aged 1-year-old samples suggests that there might be a different mechanism by which the polydispersity of the particles is incorporated. We find a sharp break in the compressibility of the columnar phase at a certain height, as well as broadening of the scattering peaks in the radial

Chapter 2

direction. On the other hand, the bond-orientational fluctuations are remarkably small, *i.e.*, of the order of 7° rather than 30° as in Fig. 2.3C. These observations point to hexatic-like ordering of the columns and would explain the apparently easy formation of a columnar phase in such highly polydisperse systems [75].

2.4 Conclusion

In this work we present clear evidence of the formation of hexagonal columnar liquid crystals in suspensions of polydisperse hard colloidal platelets. Apart from a powder of small columnar crystals we find macroscopically large single-domain crystals. Our results suggest that addition of non-adsorbing polymer promotes the formation of single-domain crystals (as we have observed before in a suspension of hard colloidal spheres [65]) with unique orientation and no sign of disordered areas. The macroscopically large crystals open up possibilities to fabricate nanostructured materials with a sub-micron periodicity that are of potential interest as, *e.g.*, photonic materials.

3

Gravity-induced liquid crystal phase transitions of hard colloidal platelets

Abstract

The influence of gravity on a suspension of sterically stabilised colloidal gibbsite platelets is studied. An initially isotropic-nematic biphasic sample of such a suspension develops a columnar phase at the bottom on prolonged standing. This phenomenon is described using a simple osmotic compression model. We performed Monte Carlo simulations of cut spheres with aspect ratio $L/D=1/15$ and took data from the literature to supply the equations of state required for the model. We find that the model describes the observed three-phase equilibrium quite well.

3.1 Introduction

The influence of gravitational compression on suspensions of colloidal particles has received attention for a long time. At the beginning of the previous century Jean Perrin [1,2] verified with simple yet brilliant experiments that the concentration of colloidal particles in dilute suspension varied exponentially with height when allowed to reach dynamic equilibrium in the earth's gravitational field. From these measurements he obtained Avogadro's number. The extension of the ideas of Perrin to interacting systems has also appeared to be very fruitful [76-79]. Crandall and Williams [80] measured the effect of the earth's gravitational field on the lattice constant of a colloidal crystal of

Chapter 3

polystyrene spheres. Perhaps even more interesting is the effect of gravity on multiple phases. Takano and Hachisu [81] pioneered the measurement of the coexistence pressure of the disorder-order transition in a sedimented dispersion of monodisperse latex particles. At an electrolyte concentration of 10 mM they found good agreement with results of computer simulations for hard spheres [82]. Hachisu and Takano [83] and later Piazza, Bellini and Degiorgio [84] and Rutgers and co-workers [85] explored the possibility to obtain the equation of state (EOS) both in the fluid as well as the crystal state from the concentration profile as a function of height. In all three cases good agreement with the hard-sphere EOS was obtained at sufficiently high salt concentration. The equivalent of this in computer simulations was done by Biben, Hansen, and Barrat [86].

For anisotropic particles, *i.e.*, rods and plates, experiments are much more limited. Colloidal hard rods and plates show intrinsically richer phase behaviour than hard spheres due to their shape. Apart from the isotropic fluid (I) and crystal phase, the nematic (N), smectic, and columnar (C) phases are encountered, so when the effect of gravity is also taken into account, this allows for the simultaneous coexistence of more than two phases. Only a few observations are available. In the 1950s, Oster [29] reported on an I-N biphasic suspension of tobacco mosaic virus rods that developed a third (Smectic-*A*) phase at the bottom of the sample after some time, an observation that was later confirmed by Kreibig and Wetter [30]. In neither case, a quantitative analysis was performed. Brian, Frisch, and Lerman [87] investigated sedimented suspensions of DNA-fragments at high salt concentration and analysed their results in terms of a scaled particle theory EOS.

Very recently, a model system of hard plates was developed in our laboratory, consisting of sterically stabilised gibbsite platelets dispersed in toluene [22]. This suspension showed the liquid crystal phase transitions predicted for such particles [13,44], *i.e.*, isotropic to nematic [22] and nematic to columnar [45]. On prolonged standing we find that an initially biphasic I-N sample developed a third phase at the bottom that we identify as a columnar phase on the basis of the optical Bragg reflections. This phenomenon can be explained by a simple osmotic compression model [47,88]. Using equations of state obtained from literature and from Monte Carlo (MC) computer simulations that we performed, we find good agreement with the experimentally determined individual phase heights.

3.2 Experiment

We synthesised a colloidal suspension of sterically stabilised gibbsite ($\text{Al}(\text{OH})_3$) platelets according to van der Kooij and Lekkerkerker [22]. Transmission electron microscopy (TEM) and atomic force microscopy were used to determine the average diameter and thickness of the particle core, thus disregarding the steric stabiliser. We found $\langle D \rangle = 230$ nm and $\langle L \rangle = 13$ nm and a polydispersity of about 22% in both dimensions. The thickness of the sterically stabilising polyisobutene brush is estimated at 2 to 3 nm, where we take

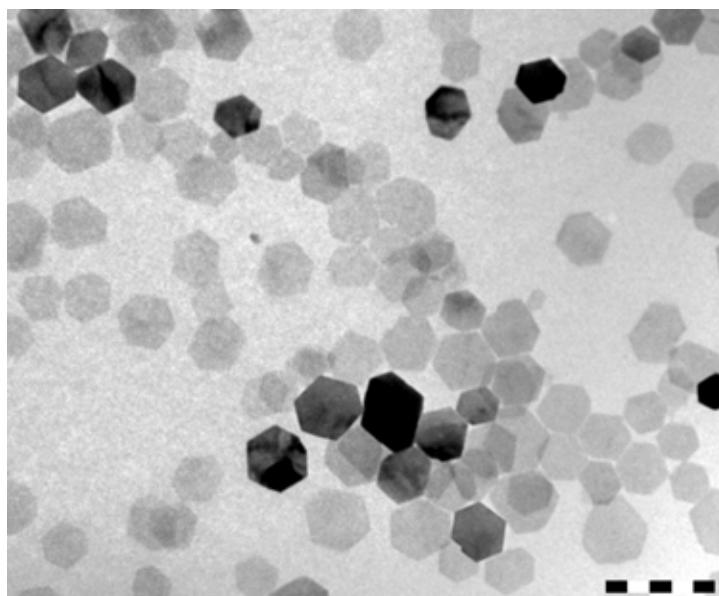


Figure 3.1 – Transmission electron microscope graph showing the gibbsite platelets (the stabilising polyisobutene layer is not visible). The hexagonal shape of the nanocrystals is easily observed. The scale bar denotes 500 nm.

into account a certain maximum stretching length for the polymer at this specific molar weight and an estimate for the extent of the steric repulsion. This gives us effective dimensions of $D_{\text{eff}} = 235$ nm and $L_{\text{eff}} = 18$ nm and hence an aspect ratio of $L/D \approx 1/13$. Fig. 3.1 shows a TEM micrograph of the platelets.

We investigated the phase behaviour in the gravitational field by preparing a sample of this

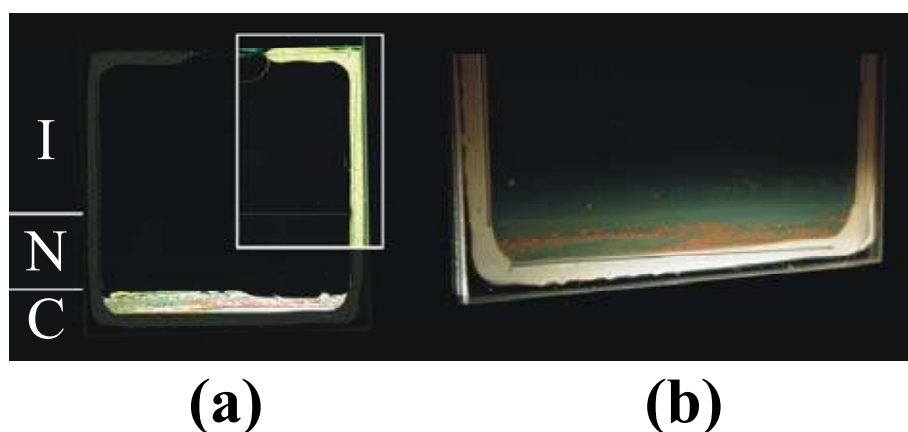


Figure 3.2 – The three-phase sedimentation equilibrium. Photograph (a) depicts the complete sample between crossed polarisers, where the upper right part is digitally enhanced to visualise the I-N interface. The columnar phase contains a dark region at the upper right of the phase, probably due to orientation of the platelets along the sample walls. Although not clearly visible, the N-C interface is horizontal and sharp. (b) shows the columnar phase illuminated with white light to capture the red Bragg reflections. (See colour version at page 132.)

Chapter 3

dispersion at a concentration in the I-N biphasic gap, in a glass cell with a height of about 30 mm. On a timescale of several days, the sample separated into an isotropic upper phase and a birefringent nematic lower phase. The phase-separated sample was investigated on a regular basis for one and a half year. After a few months, a third phase evolved at the bottom of the cell, which appeared to be a columnar phase, see Fig. 3.2. The columnar phase developed bright Bragg reflections (deep red to blue, depending on the angle of the incident light) in time.

After one year, the sample did not show any appreciable change anymore and we found the heights of the phases to be 15.5, 8.5, and 2.5 mm for the isotropic, nematic, and columnar phase, respectively.

3.3 Model

3.3.1 Sedimentation-diffusion equilibrium

Consider a suspension of monodisperse, hard disks with number density $n(z)$ and buoyant mass $m^* = v_p (\rho_p - \rho_0)$, with v_p the single particle volume and ρ_p and ρ_0 the mass densities of the particle and solvent, respectively. When sedimentation-diffusion equilibrium is reached, Eq. (3.1) describes the complete system [47,88]:

$$-\left(\frac{\partial \Pi}{\partial n}\right) \frac{\partial n}{\partial z} = m^* g n. \quad (3.1)$$

To simplify the approach, we define reduced quantities. The pressure will be given by $\tilde{\Pi} = \Pi D^3 / k_B T$, the gravitational length scale $\xi = k_B T / m^* g$, and the reduced concentration $c = n D^3$. Substituting these expressions in Eq. (3.1) yields

$$\frac{1}{c} \left(\frac{\partial \tilde{\Pi}}{\partial c} \right) dc = -\frac{dz}{\xi}. \quad (3.2)$$

For a single phase, the height $H = z_{top} - z_{bottom}$ is found by integrating Eq. (3.2) from c_{top} to c_{bottom}

$$H = \int_{z_{bottom}}^{z_{top}} dz = -\xi \int_{c_{bottom}}^{c_{top}} \frac{1}{c} \frac{\partial \tilde{\Pi}}{\partial c} dc. \quad (3.3)$$

The average concentration \bar{c} of this phase is given by

$$\bar{c} = \frac{\int_{c_{bottom}}^{c_{top}} c(z) dz}{\int_{z_{bottom}}^{z_{top}} dz} = \frac{1}{H} \int_{c_{bottom}}^{c_{top}} c(z) \frac{dz}{dc} dc. \quad (3.4)$$

Using Eq. (3.2) this yields

$$\bar{c} = -\frac{\xi}{H} \int_{c_{bottom}}^{c_{top}} \frac{\partial \tilde{\Pi}}{\partial c} dc = \frac{\xi}{H} [\tilde{\Pi}(c_{bottom}) - \tilde{\Pi}(c_{top})]. \quad (3.5)$$

For multiple phases in sedimentation equilibrium, Eqs. (3.3) and (3.5) apply to each of the phases. The total sample height H^{sample} is obviously the sum of the individual phase heights H^α

$$H^{sample} = \sum_{\alpha} H^\alpha, \quad (3.6)$$

where the summation ranges over all the phases. The average overall sample concentration \bar{c}^{sample} can now be written as

$$\bar{c}^{sample} = \frac{1}{H^{sample}} \sum_{\alpha} H^\alpha \bar{c}^\alpha = \frac{\xi}{H^{sample}} \sum_{\alpha} [\tilde{\Pi}(c_{bottom}^\alpha) - \tilde{\Pi}(c_{top}^\alpha)], \quad (3.7)$$

where the \bar{c}^α are the average phase concentrations. Taking into account that for two coexisting phases α and β (where α on top of β)

$$\tilde{\Pi}(c_{bottom}^\alpha) = \tilde{\Pi}(c_{top}^\beta), \quad (3.8)$$

Eq. (3.7) together with Eq. (3.5) leads to the surprisingly simple result

$$\bar{c}^{sample} = \frac{\xi}{H^{sample}} [\tilde{\Pi}(c_{bottom}^{sample}) - \tilde{\Pi}(c_{top}^{sample})]. \quad (3.9)$$

3.3.2 Equation of state

In order to calculate the individual phase heights for a given overall concentration from Eqs. (3.3) and (3.9) we need to know the EOS for the various coexisting phases. Zhang, Reynolds, and van Duijneveldt [44] performed MC computer simulations on cut spheres (particles obtained by slicing two caps off a sphere of diameter D , at two planes parallel to

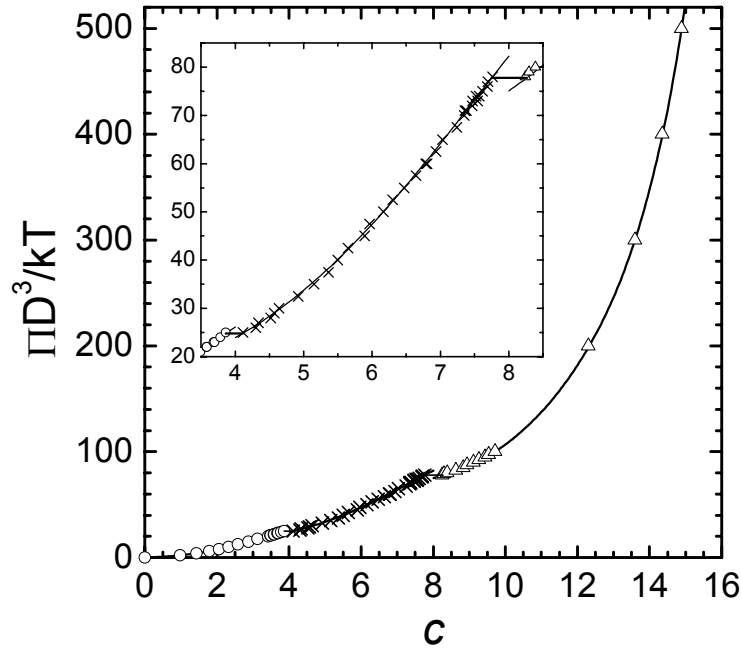


Figure 3.3 – The equation of state from MC simulations for cut spheres with aspect ratio $L/D = 1/15$. Circles are for the isotropic, crosses for the nematic, and triangles for the columnar phase. The phase transitions are indicated with thick lines. The inset shows the region of the phase transitions.

the equatorial plane, each at a distance $L/2$) with aspect ratios of $L/D = 1/10$ and $L/D = 1/20$ and obtained equations of state for both aspect ratios. As our particles have an aspect ratio that is in between these values, we decided to fill the gap ourselves.

We have performed constant- NPT Monte Carlo simulations of a system of 1000 cut spheres with aspect ratio $L/D = 1/15$. The box was rectangular with independently variable side lengths to accommodate the columnar phase. The EOS shown in Fig. 3.3 was obtained by expansion from the columnar phase into the isotropic as well as compression from the isotropic to the columnar. For each pressure we equilibrated for 400000 MC steps.

The EOS shows two density jumps indicating first order phase transitions: the I-N transition and the N-C transition. Close to the transitions the system showed a small hysteresis in both cases. This is due to finite simulation time and finite system size – no fluctuation occurred on the time scale of the simulation that took the system over the nucleation barrier to the next phase. We could nevertheless locate the I-N transition to the accuracy we desired for this work, and found $c_I = 3.68$ and $c_{NI} = 4.11$, with a corresponding pressure of $\tilde{\Pi}_{I-N} = 24.8 \pm 1.0$. The hysteresis around the N-C transition, however, was too strong. From the work of Zhang, Reynolds, and van Duijneveldt [44] it appears that the

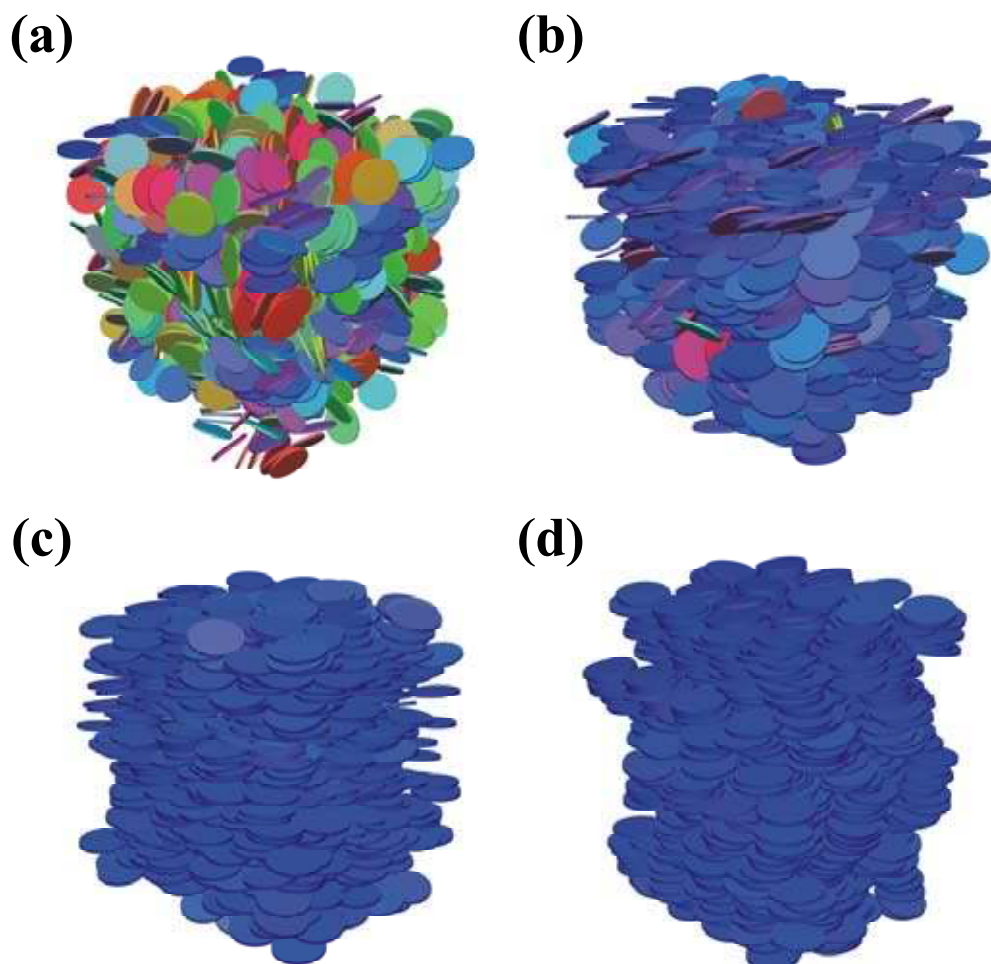


Figure 3.4 – Configuration snapshots from the MC computer simulations, illustrating the positional and orientational order close to the I-N and N-C phase transitions. Shading or colour is used to distinguish between different orientations of the platelets. Snapshots (a) and (b) display the isotropic ($c = 3.39$, $\tilde{\Gamma} = 20$) and nematic phase ($c = 4.62$, $\tilde{\Gamma} = 30$) just below and above the I-N transition, respectively. Clearly, the orientational order has increased, whereas (long range) positional order is still lacking. Snapshots (c) and (d) show the nematic and columnar phase, respectively, near the N-C transition (at state points $c = 7.49$, $\tilde{\Gamma} = 73$ and $c = 8.66$, $\tilde{\Gamma} = 82.5$, respectively). At the N-C transition, there is hardly any gain in orientational order, while the positional order becomes two-dimensional in the columnar phase. (See colour version at page 133.)

Chapter 3

Table 3.1 – The fitting parameters to our simulation data for the equation of state for cut spheres with $L/D=1/15$. The equation of state is given by $\tilde{\Pi} = \sum_{n=1}^6 A_n c^n$, where $\tilde{\Pi} = \Pi D^3/k_B T$ and $c = nD^3$.

phase	c	A_1	A_2	A_3	A_4	A_5	A_6
isotropic	0-3.86	1	0.79432	0.44616	-0.07468	0	0
nematic	4.11-7.75	11.8418	-4.1226	0.83763	-0.04333	0	0
columnar	8.29-15.0	-321.039	170.441	-34.5412	3.43735	-0.16856	0.00329678

N-C phase transition concentrations (expressed as a volume fraction ϕ) are independent of the aspect ratio (either 1/10 or 1/20). Therefore, we interpolate to obtain the N-C transition concentrations in our system and find $c_{NC} = 7.75$ and $c_C = 8.29$ using the relation $\phi = \frac{\pi}{12} \frac{L}{D} \left[3 - \left(\frac{L}{D} \right)^2 \right] c$. The pressure at the transition is found to be $\tilde{\Pi}_{N-C} = 77.8 \pm 1.0$. The resulting EOS is plotted in Fig. 3.3. We show configuration snapshots in Fig. 3.4 to illustrate the positional and orientational order just below and above the phase transitions. In order to use the obtained simulation data in our model, we fitted polynomials to the three branches of the EOS. Thus, three sets parameters were obtained that are given in Table 3.1.

3.4 Results and discussion

We now turn to the analysis of the sedimentation equilibrium that we have observed. The key parameter in our system is the gravitational length scale ξ defined above. Taking into account that for our hexagonal particles $v_p = \frac{3}{8} \sqrt{3} D^2 L = 6.5 \times 10^{-22} \text{ m}^3$ and $\rho_p - \rho_0 = 835 \text{ kg/m}^3$, we find $\xi = 0.77 \text{ mm}$. The measured total sample height is 26.4 mm, which yields a dimensionless height of $H/\xi = 34.3$. By setting the overall concentration to a concentration in the I-N biphasic gap (as imposed by the experiment) we calculate the individual phase heights using the model detailed in Section 3.3.1 and the equations of state of Zhang, Reynolds, and van Duijneveldt [44] and the one we obtained. The results are presented in Table 3.2 and Fig. 3.5 visualises the evolution of the calculated phase heights with aspect ratio. From this figure it is clear that at our experimental aspect ratio of 1/13 the phase heights are not correctly predicted. However, a fairly good description is obtained for $L/D=1/19$. A similar difference is found for a previous study of the same colloidal suspension of sterically stabilised gibbsite platelets. Van der Kooij, Kassapidou, and Lekkerkerker [45] found the experimental aspect ratio to be 1/14 for their platelets. Based on an analysis of the I-N and N-C coexistence concentrations, we observe that the effective aspect ratio in their case appears to be slightly lower as well, *i.e.*, $L/D=1/17$.

Table 3.2 – Heights in millimetres of the individual phases after settling of the sedimentation-diffusion equilibrium, as measured and calculated.

phase	measured height	calculated height with		
		$L/D = 1/10$	$L/D = 1/15$	$L/D = 1/20$
I	15.5	14.1	15.0	15.7
N	8.5	3.0	6.8	8.5
C	2.5	9.3	4.6	2.2

A possible reason for the discrepancy between theory and experiment could lie in the shape characteristics of the particles. The experimental platelets are polydisperse hexagonal particles, while the model is based on monodisperse circular disks. Recently, Bates [89] has reported on the influence of particle shape of infinitely thin platelets on the I-N transition. It is found that the transition densities are lowered just by 10% when going from circular to hexagonal platelets. In a study of the influence of polydispersity on the I-N phase transition for infinitely thin hard platelets, Bates and Frenkel [14] find that the transition densities for 22%-polydisperse disks deviate more substantially from the monodisperse values ($c_I = 3.56$ and $c_N = 4.75$ versus 3.68, respectively, 3.98 for the monodisperse case). This leads us to the conclusion that the calculated individual phase

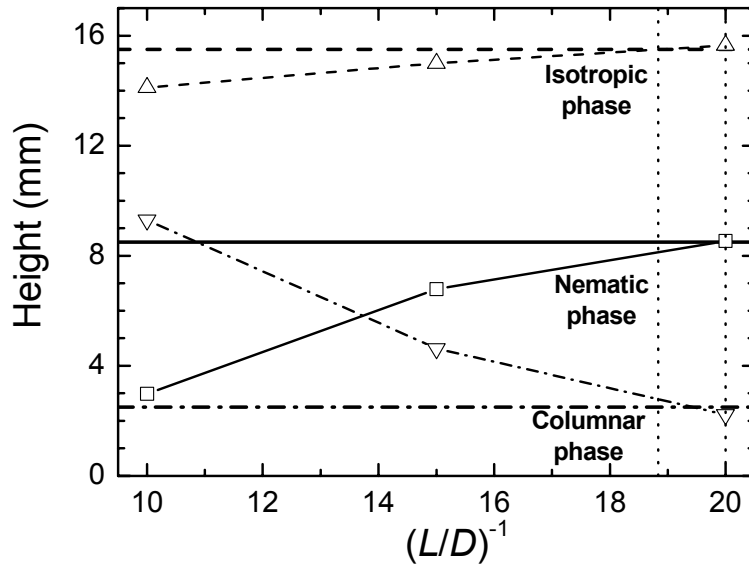


Figure 3.5 – The heights of the individual phases vs. aspect ratio, using the values given in Table 3.2. For each phase, the measured (horizontal lines) and calculated heights (lines with symbols) are given. Dashed lines refer to the isotropic, solid lines refer to the nematic, and dash-dotted lines refer to the columnar phase. The vertical dotted lines indicate the interval (around $L/D = 1/19$) where our experiment is quite well described.

Chapter 3

heights could very well be influenced by particle shape and polydispersity, although it is unclear to what extent. To address this issue would require an EOS and the chemical potentials for a system of polydisperse hexagonal platelets. These have been obtained for polydisperse hard spheres [79], but for hexagonal platelets the problem will perhaps be slightly more complex.

3.5 Conclusion

We have studied the influence of gravity on a suspension of sterically stabilised colloidal gibbsite platelets (hard platelets). An initially I-N biphasic sample developed a columnar phase at the bottom of the sample by sedimentation of the particles. This dynamical sedimentation-diffusion equilibrium was reached on a timescale of a year. In order to describe the phenomenon, we used a simple osmotic compression model, requiring an equation of state for the platelets. These were obtained from literature and from Monte Carlo computer simulations that we performed. We find that the model describes the observed three-phase equilibrium quite well, be it for an aspect ratio that is significantly smaller than the experimental value.

Part II

**Sterically stabilised colloidal gibbsite
platelets in an external magnetic field**

4

Small-angle X-ray scattering study of the magnetic-field-induced orientational order in the isotropic phase of colloidal gibbsite platelets

Abstract

We study the magnetic-field-induced orientational order of an isotropic phase of colloidal gibbsite ($\text{Al}(\text{OH})_3$) platelets by small-angle X-ray scattering (SAXS). At magnetic field strengths of 3 to 7 T these platelets show strong alignment, with an order parameter that attains values up to $S_2 = -0.2$, which is fairly large considering that the maximum value is $S_2 = -\frac{1}{2}$. We provide a model that, despite its simplicity, is able to describe the observed SAXS patterns reasonably well. In addition, the model yields an estimate of the diamagnetic susceptibility anisotropy $\Delta\chi$.

4.1 Introduction

The study of colloidal suspensions submitted to electric and magnetic fields is a very old subject. It dates back to the end of the 19th century, when John Kerr [90] discovered that certain pure liquids showed birefringence when subjected to strong electric fields. This electro-optical effect is now known as the Kerr effect.

Kerr contributed to the field of magnetic birefringence as well and was actually the first to report this phenomenon in a suspension of chemically precipitated magnetite [91]. Majorana [92-98] and Cotton and Mouton [99-103] studied magnetic birefringence in suspensions of so-called “fer Bravais”, a suspension of iron oxides that was commonly

Chapter 4

used in pharmacy at that time. Cotton and Mouton furthermore found that pure liquids also showed magnetic birefringence [104], a phenomenon that is nowadays known by the discoverers' names.

In recent years, Lemaire and co-workers [25,105,106] have studied suspensions of colloidal goethite (α -FeOOH) nanorods that, as a matter of fact, are closely related to the suspensions studied by Majorana and Cotton and Mouton. Suspensions of these rods, somewhat comparable to ferrofluids, are very sensitive to an external magnetic field and align in a field of the order of 0.2 T. In addition, they display a very peculiar phenomenon, *i.e.*, the reorientation of the rods with increasing field strength. Below about 0.35 T, the rods align parallel to the field, while above this value they turn perpendicular to it.

As opposed to inorganic rods, isotropic suspensions of organic particles, such as virus particles, need much higher fields (up to 20 T) to induce magneto-optical effects. Examples include rod-like cellulose microcrystals [107], tobacco mosaic virus (TMV) [108,109], *fd* virus [110-112], and *Pfl* virus [113] particles, as well as plate-like biological membranes [114]. Although the shape of those particles is highly anisotropic, their intrinsic diamagnetic susceptibility anisotropy $\Delta\chi_0$ (*i.e.*, of the bulk material) is much lower, giving rise to a much lower "effective" diamagnetic susceptibility anisotropy per particle $\Delta\chi$ than *e.g.* inorganic goethite rods.

Here, we report a study of an isotropic phase of colloidal gibbsite ($\text{Al}(\text{OH})_3$) platelets in a magnetic field. In view of the abovementioned, we may expect magnetic-field-induced orientational order at much lower field strengths (3 to 5 T) compared to organic moieties, as these inorganic anisometric particles have high diamagnetic susceptibility anisotropies.

We decided to study different field-induced phenomena of our gibbsite platelets. First of all, in this chapter, we will investigate the magnetic-field-induced order with small-angle X-ray scattering (SAXS). We show that the platelets indeed show considerable order at moderate fields. The anisotropic scattering patterns that we obtained can be analysed using a model that allows probing the orientational distribution function directly from the scattering data. Despite its simplicity, it gives us a value for the diamagnetic susceptibility anisotropy $\Delta\chi$.

4.2 Theory

4.2.1 The orientational distribution function

Let us consider a single plate-like particle immersed in a magnetic field with magnitude B directed along the z -axis. The orientation of the platelet is indicated by the platelet normal \hat{e}_\parallel , which makes an angle θ to the magnetic field direction (the z -axis), see Fig. 4.1. For a mineral crystal like gibbsite, the magnetic susceptibility χ will be different along the different axes of the particle. Therefore, the magnetisation along these axes will differ as well. Thus, the induced magnetisation \vec{m} of the particle can be written as

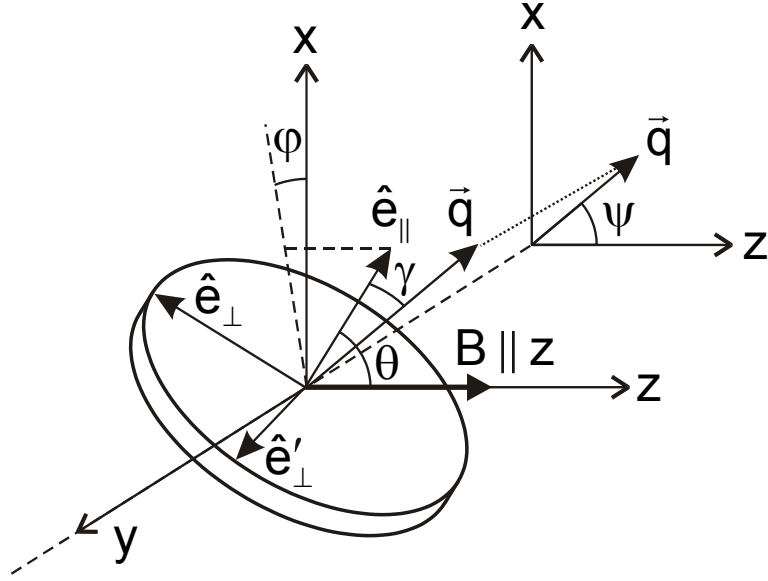


Figure 4.1 – Sketch of the magnetic and scattering coordinate system. Symbols are explained in the text.

$$\vec{m} = \chi_{\parallel} B_{\parallel} \hat{e}_{\parallel} + \chi_{\perp} B_{\perp} \hat{e}_{\perp}. \quad (4.1)$$

The corresponding magnetic energy w_{mag} (per particle) is then given by

$$w_{mag} = -\frac{1}{2} \vec{m} \cdot \vec{B} = -\left(\frac{1}{2} \chi_{\parallel} B_{\parallel}^2 + \frac{1}{2} \chi_{\perp} B_{\perp}^2 \right) = -\frac{1}{2} (\chi_{\parallel} - \chi_{\perp}) B^2 \cos^2 \theta - \frac{1}{2} \chi_{\perp} B^2 \quad (4.2)$$

We define $\Delta\chi$ as

$$\Delta\chi \equiv \chi_{\parallel} - \chi_{\perp}. \quad (4.3)$$

Neglecting the non orientation-dependent term, equation (4.2) can be written as

$$w_{mag}(\theta) = -\frac{1}{2} \Delta\chi B^2 \cos^2 \theta, \quad (4.4)$$

or, equivalently, in terms of the second order Legendre polynomial $P_2(x) = \frac{1}{2}(3x^2 - 1)$ and retaining only the orientation-dependent terms

$$w_{mag}(\theta) = -\frac{1}{3} \Delta\chi B^2 P_2(\cos\theta). \quad (4.5)$$

In our case, as will be shown later on, $\Delta\chi$ is negative, hence in a magnetic field the platelets align with their *normals perpendicular* to the field, as the magnetic energy is lowest in this configuration. An isotropic phase of gibbsite particles that is aligned in a magnetic field will – strictly speaking – not be isotropic anymore and is called paranematic to distinguish it from the nematic phase at zero field. For the particles considered here, a marked difference between these phases in a magnetic field is their symmetry. At zero field, the isotropic phase obviously has no symmetry axis. The nematic phase is aligned in a certain arbitrary direction, called the director, and has uniaxial symmetry. As soon as these phases are only slightly aligned, *e.g.* by a magnetic field, their symmetry changes. Due to the sign of diamagnetic susceptibility, the director of the nematic phase will be orient perpendicular to the magnetic field. Hence, the nematic phase will become biaxial. On the other hand, the alignment in the paranematic phase can be described with one axis and, hence, this phase is uniaxial. The orientational distribution function (ODF) $f(\theta)$ of the paranematic phase therefore only depends on θ , see Fig. 4.1.

At low particle concentrations, where the interparticle interactions are negligible, the ODF of the particles is simply given by the Boltzmann factor of the magnetic energy

$$f(\theta) = \frac{1}{Z} \exp\left[\frac{1}{3} \frac{\Delta\chi B^2 P_2(\cos\theta)}{kT}\right], \quad (4.6)$$

where Z is a normalisation constant. For low magnetic field strengths, this expression can be linearised as

$$f(\theta) = \frac{1}{4\pi} \left[1 + \frac{1}{3} \frac{\Delta\chi B^2 P_2(\cos\theta)}{kT}\right]. \quad (4.7)$$

The order parameter, defined as $S_2 \equiv \langle P_2(\cos\theta) \rangle$, is then given by

$$S_2 = \frac{1}{15} \frac{\Delta\chi B^2}{kT}, \quad (4.8)$$

which immediately shows that for negative $\Delta\chi$ the particles align with their normals perpendicular to the magnetic field ($S_2 < 0$). Note that for an infinitely sharply peaked

distribution function around $\theta_0 = \frac{1}{2}\pi$, with the platelet normals perpendicular to magnetic field, $f(\theta) = \frac{1}{2\pi} \delta(\theta - \frac{1}{2}\pi)$ and hence the lower bound for $S_2 = -\frac{1}{2}$.

In order to calculate the orientational distribution function for higher concentrations, we need to take into account the effect of interparticle interactions. This can be done in an Onsager-like approach, minimising the free energy expression containing the orientational entropy, packing entropy and magnetic energy. At low field strengths, the distribution function is only weakly perturbed and can be written as

$$f(\theta) = \frac{1}{4\pi} (1 + \varepsilon P_2). \quad (4.9)$$

with $|\varepsilon| \ll 1$. Guided by Straley [115], it follows that

$$f(\theta) = \frac{1}{4\pi} \left[1 + \frac{1}{3} \frac{\Delta\chi B^2 P_2(\cos\theta)}{kT} \frac{1}{1 - \phi/\phi^*} \right], \quad (4.10)$$

with ϕ the volume fraction and ϕ^* the so-called spinodal volume fraction, above which the isotropic state becomes locally unstable. This equation closely resembles Eq. (4.7). The corresponding order parameter is given by

$$S_2 = \frac{1}{15} \frac{\Delta\chi B^2}{kT} \frac{1}{1 - \phi/\phi^*}, \quad (4.11)$$

in agreement with earlier results [109,115]. We note that this result is valid for both rod- and plate-like particles. Treating Eq. (4.10) as if it were the result of a Taylor expansion, we obtain

$$f(\theta) = \frac{1}{Z} \exp \left[\frac{1}{3} \frac{\Delta\chi B^2 P_2(\cos\theta)}{kT} \frac{1}{1 - \phi/\phi^*} \right], \quad (4.12)$$

which can be looked upon as a rescaled Boltzmann distribution.

4.2.2 Small-angle X-ray scattering

Here, we will derive a simple model in order to analyse the SAXS data. The model is based on the observation that the Fourier transform, and hence the form factor, of an infinitely thin platelet (with thickness-to-diameter ratio $L/D = 0$) is an infinitely thin rod, directed

Chapter 4

along the platelet normal. Similarly, for finite platelets with low aspect ratio ($L/D \ll 1$), in a certain range of wave vectors, the scattering is strongly directed along their normals. This leads to a very simple relation between the scattered intensity (as recorded in the SAXS patterns) and the orientational distribution function of the platelets.

In a SAXS experiment, the time-averaged intensity of the scattered X-rays is measured. The so-called Rayleigh ratio $R(q) = R_0^2 I(q)/VI_0$ is a measure of the scattered intensity $I(q)$, which is normalised by taking into account the intensity of the incident beam I_0 , the scattering volume V , and the sample-detector distance R_0 . For spherical particles the Rayleigh ratio can be written as [66,116]

$$R(q) = Nr_0^2 Z^2 F(q)S(q), \quad (4.13)$$

the product of the form factor $F(q)$ and the structure factor $S(q)$. Here the prefactor contains the number density of the particles N , the Thompson radius $r_0 \equiv e^2/m_e c^2$, and the excess number of electrons in the colloidal particle relative to an equivalent volume of solvent Z . The scattering wave vector q is defined as

$$q = \frac{4\pi}{\lambda} \sin \Theta, \quad (4.14)$$

where λ the wavelength of the X-rays and 2Θ the scattering angle. Since the form factor and structure factor are coupled in the case of non-spherical particles, they cannot simply be factorised like for spheres. However, for particles at very low concentrations, the structure factor $S(q) \approx 1$. The Rayleigh ratio then becomes

$$R(q) = Nr_0^2 Z^2 \langle F(q, \gamma) \rangle. \quad (4.15)$$

The angular brackets denote ensemble averaging over all particles with different angles γ , the angle between a particle normal \hat{e}_\parallel and the wave vector \vec{q} . Fig. 4.1 illustrates the setup and the used symbols. In addition, we note that γ is related to θ and ϕ (determining the platelet orientation with respect to the x -axis), and ψ (that determines the orientation of the scattering vector in the xz plane) according to

$$\cos \gamma = \cos \theta \cos \psi + \sin \theta \sin \psi \cos \phi. \quad (4.16)$$

The formfactor of a cylinder is classically given by Guinier and Fournet [117] as

$$F(q, \gamma) = \left[\frac{J_1(\frac{1}{2}qD \sin \gamma)}{\frac{1}{2}qD \sin \gamma} \frac{\sin(\frac{1}{2}qL \cos \gamma)}{\frac{1}{2}qL \cos \gamma} \right]^2, \quad (4.17)$$

with J_1 the Bessel function of the first kind. It is convenient to factorise the form factor in its perpendicular components by defining the scattering vector components q_{\parallel} and q_{\perp} parallel and perpendicular to the platelet normal \hat{e}_{\parallel} as

$$\begin{aligned} q_{\parallel} &= q \cos \gamma \\ q_{\perp} &= q \sin \gamma \end{aligned} \quad (4.18)$$

and substitute in Eq. (4.17) to obtain

$$F(q_{\parallel}, q_{\perp}) = F_{\parallel}(q_{\parallel})F_{\perp}(q_{\perp}) = \left[\frac{\sin(\frac{1}{2}q_{\parallel}L)}{\frac{1}{2}q_{\parallel}L} \right]^2 \left[\frac{J_1(\frac{1}{2}q_{\perp}D)}{\frac{1}{2}q_{\perp}D} \right]^2. \quad (4.19)$$

Fig. 4.2 depicts the two components $F_{\parallel}(q)$ and $F_{\perp}(q)$ of the form factor of a cylindrical disk with aspect ratio $L/D = 1/18$. (This specific value is dictated by the experiment, see Section 4.3.1.) As can be observed in Fig. 4.2, there is a q -domain where the components

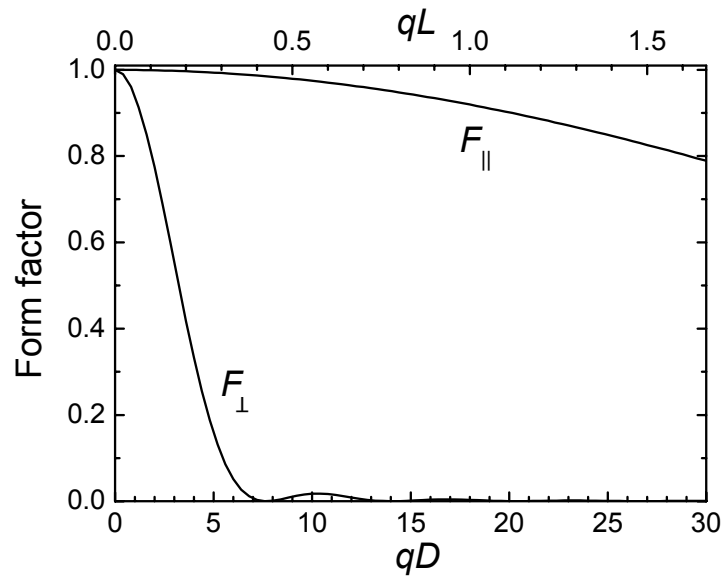


Figure 4.2 – The two components of the form factor of a cylindrical disk with aspect ratio $L/D = 1/18$, as defined in Eq. (4.19). In the intermediate regime, F_{\perp} decays very fast, while F_{\parallel} decreases only slowly with q .

Chapter 4

of the form factor differ substantially in magnitude. In this so-called “intermediate regime” [117], where $\frac{2\pi}{D} \ll q \ll \frac{2\pi}{L}$, $F_{\parallel}(q) \approx 1$ and remains nearly constant, while $F_{\perp}(q)$ decays to values 1 to 3 orders of magnitude lower than $F_{\parallel}(q)$. Thus, for a given value of the scattering vector q , scattering essentially comes only from platelets oriented such that q_{\perp} is small, *i.e.*, for small angles of γ . Hence, we have a very narrow scattering peak. This is explained in detail in the Appendix to this chapter.

In order to calculate the scattered intensity of an ensemble of platelets with a certain orientational distribution function $f(\theta)$, as a function of q and ψ in the detector plane, we have to evaluate the following integral (cf. Eq. (4.15) and using Eqs. (4.16) and (4.18))

$$I(q, \psi) \propto \langle F(q, \gamma) \rangle = \iint f(\theta) F(q_{\parallel}, q_{\perp}) \sin \theta d\theta d\varphi. \quad (4.20)$$

For weakly perturbed orientational distributions, $f(\theta)$ is slowly varying over the very narrow scattering peak. This allows us to take it out of the integral, however, by doing this we make a rather crude approximation. We hence obtain

$$I(q, \psi) \propto f(\theta = \psi) \iint F_{\parallel}(q_{\parallel}) F_{\perp}(q_{\perp}) \sin \theta d\theta d\varphi. \quad (4.21)$$

As $F_{\parallel}(q_{\parallel}) \approx 1$, the integral depends only on $F_{\perp}(q_{\perp})$ and we approximate the latter by

$$F_{\perp}(q_{\perp}) \approx \begin{cases} 1 & q_{\perp} < q_0 \\ 0 & q_{\perp} > q_0 \end{cases}, \quad (4.22)$$

where $q_0 = 3.83/\frac{1}{2}D$ is the first minimum of F_{\perp} . (The last step is equivalent to treating a circle as a square with a length equal to the circle’s diameter.) The condition $\gamma < \Delta\gamma$, or, equivalently, $\gamma \ll 1$, is fulfilled if $\theta \approx \psi$ and $\varphi \approx 0$, following Eq. (4.16). Furthermore, for small angles, $\arctan(q_0/q) \approx q_0/q$ and hence

$$\iint F_{\perp}(q_{\perp}) \sin \theta d\theta d\varphi \propto (\Delta\gamma)^2 \propto \frac{1}{q^2}. \quad (4.23)$$

We now obtain the very simple result

$$I(q, \psi) \propto \frac{f(\psi)}{q^2}. \quad (4.24)$$

This implies that the ODF can be obtained directly from the scattering data at constant q in the intermediate regime, making our data analysis quite straightforward. In our model, the scattered intensity depends on q (it decays monotonously), while the anisotropy of the scattering, as measured from *e.g.* the ellipticity of the iso-intensity lines, is independent of q . It will become clear, however, that in reality this is not the case: the anisotropy decreases with increasing q , slightly obstructing the determination of the ODF.

4.3 Experiment

4.3.1 Preparation and characterisation

We synthesised hexagonal colloidal gibbsite ($\text{Al}(\text{OH})_3$) platelets [50] that were subsequently grafted with end-functionalised polyisobutene and suspended in toluene to obtain a model system of hard platelets [22,45]. This specific batch was the same one as used in the experiments described in Chapters 2 and 3. Transmission electron microscopy and atomic force microscopy were used to determine the average corner-to-corner diameter, D , and thickness, L , of the dry particle core, although the latter might contain a contribution of the collapsed steric stabiliser. We found $\langle D \rangle = 232$ nm and $\langle L \rangle = 13$ nm and a polydispersity of about 20% in both dimensions. In solution, the thickness of the sterically stabilising polyisobutene brush is an estimated 2 to 3 nm. This gives us effective dimensions of $D_{\text{eff}} = 237$ nm and $L_{\text{eff}} = 18$ nm and hence an aspect ratio of $L/D \approx 1/13$. We note that the electron density of the polymer layer is comparable to that of the solvent. Therefore, the X-ray scattering from the polymer layer is negligible, yielding an “effective SAXS aspect ratio” that is equal to that of the gibbsite core, *i.e.*, $L/D = 1/18$. We have therefore used 1/18 rather than 1/13 in Section 4.2.2 on small-angle X-ray scattering.

4.3.2 Samples and methods

A stock dispersion of the sterically stabilised gibbsite platelets was prepared in the isotropic phase. The volume fraction of the stock was calculated from the mass concentration (determined by drying a known amount of dispersion at 85°C to constant weight) and the previously measured particle mass density $\rho_p = 1.7$ g/ml as $\phi_{\text{stock}} = 0.219$. From the stock solution, three dilutions were prepared at volume fractions of $\phi = 0.165$, 0.109, and 0.050. These samples were put in Lindemann cylindrical glass capillaries (internal diameter 0.7 mm) and subsequently flame sealed. The dispersion used in this study shows the I-N phase transition. From the evolution of the phase volumes with volume fraction, we found the isotropic and nematic phase boundaries to be located at $\phi_I = 0.238$ and $\phi_N = 0.255$.

Chapter 4

We used the SAXS setup of the Dutch-Belgian beamline BM-26 DUBBLE at the European Synchrotron Radiation Facility (ESRF, Grenoble, France). The scattered X-rays were detected using a $13 \times 13 \text{ cm}^2$ multiwire Argon-filled detector, with a pixel size of about $250 \text{ }\mu\text{m}$. An X-ray beam of 17 keV (wavelength $\lambda = 0.73 \text{ \AA}$) and a sample-detector distance of about 8 m were used. The accessible q -range was 0.05 to 0.70 nm^{-1} both in the horizontal and vertical direction. The setup was calibrated using the fibre diffraction of wet rat-tail collagen, which has strong characteristic peaks at $q = 2\pi n/67.2 \text{ nm}^{-1}$ ($n = 1, 3, 5$). The beamline was equipped with a helium-cooled superconducting magnet, giving a horizontally directed magnetic field and capable of reaching a maximum magnetic field of $B_{\text{max}} = 7 \text{ T}$ that was homogeneous in a volume of 1 cm^3 . To avoid the influence of gravity, the measurements were performed within 8 days after sample preparation. SAXS patterns were acquired at six different field strengths yielding uniformly spaced values of B^2 between 0 to 49 T^2 . Each pattern was corrected for detector sensitivity and background scattering.

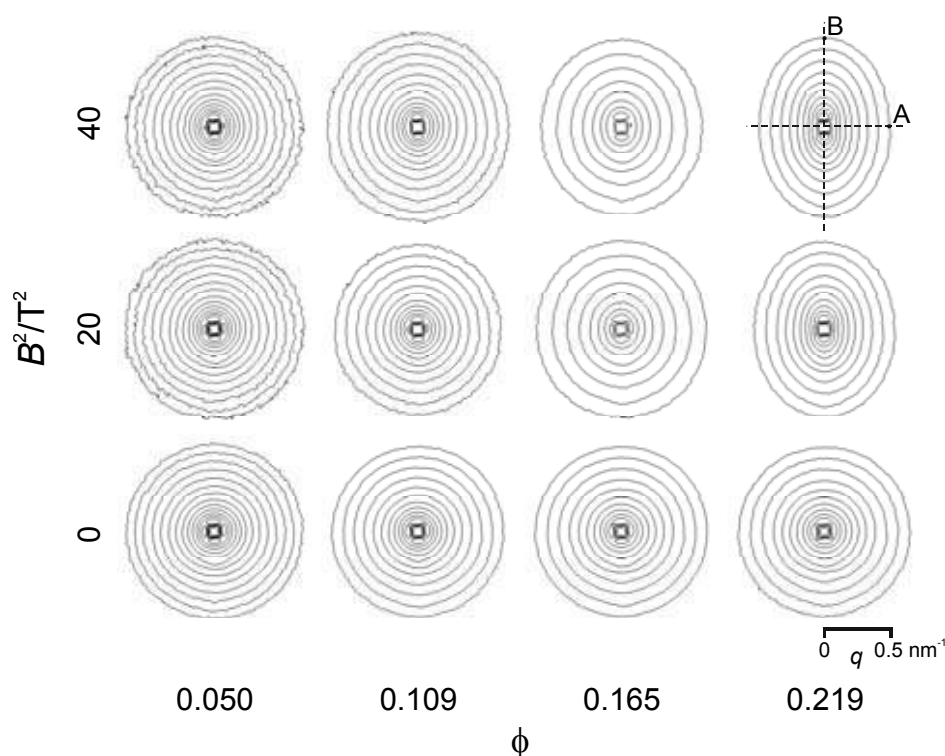


Figure 4.3 – Iso-intensity lines of a few of the small-angle X-ray scattering patterns obtained in this study, as a function of volume fraction ϕ and field strength squared B^2 . The magnetic field is oriented horizontally. Clearly, the ellipticity of the scattering patterns increases with increasing volume fraction and field strength, while it decreases with increasing wave vector q , as more easily observed in Fig. 4.9. In the measurement of the ellipticity of the patterns, we have made use of two points A and B on the iso-intensity line; an example is shown in the upper right pattern.

4.4 Results and discussion

The most striking feature of the (in zero field) isotropic dispersions of gibbsite platelets is the strong anisotropy of the scattering at high magnetic field, which is displayed in Fig. 4.3. Given the fact that the magnetic field is oriented horizontally, this figure shows that the particles align with their normals perpendicular to the field. This means that indeed $\Delta\chi$ has a negative value. We can follow two approaches in order to obtain the values of $\Delta\chi$ and ϕ^* from our scattering data. In the first approach, in Section 4.4.1, we use the simple relation between the scattered intensity and the ODF, as derived in the previous section. In the second approach in Section 4.4.2, we make use of the observation that the iso-intensity lines are ellipse-like.

4.4.1 Measurement of the orientational distribution function

We have derived a simple relation between the scattered intensity and the ODF in Section 4.2.2, Eq. (4.24), and repeat it here:

$$I(q, \psi) \propto \frac{f(\psi)}{q^2}. \quad (4.25)$$

The q^{-2} -dependence of the scattered intensity is demonstrated in Fig. 4.4, where we show scattering profiles of an isotropic phase at zero field and at $B^2 = 40 \text{ T}^2$. In the intermediate regime, which has an approximate range of $0.03 \text{ nm}^{-1} < q < 0.4 \text{ nm}^{-1}$, the intensity is

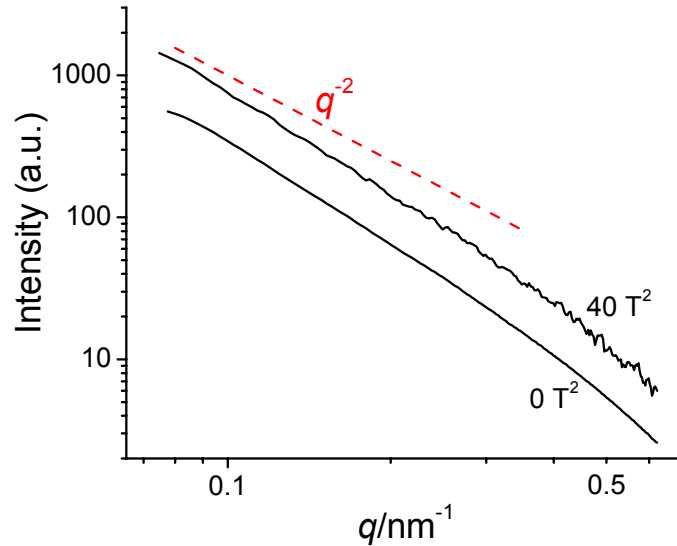


Figure 4.4 – Scattering profiles of the isotropic phase, $\phi = 0.05$, at zero field, obtained by radial averaging, and at $B^2 = 40 \text{ T}^2$, obtained for a thin slice (width < 0.01 radians) with $\psi = 0$. The dashed line indicates that the scattered intensity roughly follows q^{-2} -decay.

reasonably well described by a q^{-2} decay at constant $f(\psi)$. From Eq. (4.25) we obtain

$$f(\psi) \propto I(q_i, \psi), \quad (4.26)$$

when measured at an arbitrary value of q_i in the intermediate regime. The (real) ODF does not depend on q but is solely determined by the characteristics of the dispersion and the applied magnetic field. In our model, the ODF does not depend on q either; it depends only on the anisotropy of the scattered intensity $I(q_i, \psi)$ at constant q_i . However, in our experiment, we observe that the anisotropy of the scattering decreases with increasing q . This means that the ODF will depend on the q_i where we measure it.

We obtain $I(q_i, \psi)$ from the SAXS patterns by taking thin circular slices at three intermediate q -values (0.1, 0.2, and 0.3 nm⁻¹). For each slice, we average a small range of q -values ($q \pm 0.003$ nm⁻¹) to improve statistics. We further average the scattered intensity by making use of the centrosymmetry of the scattering. ($I(q_i, \psi) = \frac{1}{2}I(q_i, \psi = a) + \frac{1}{2}I(q_i, \psi = a + \pi)$ for $0 < \psi < \pi$.) With appropriate normalisation, these data simply represent the ODF, as illustrated in Fig. 4.5. The ODF is given by (Eq. (4.12))

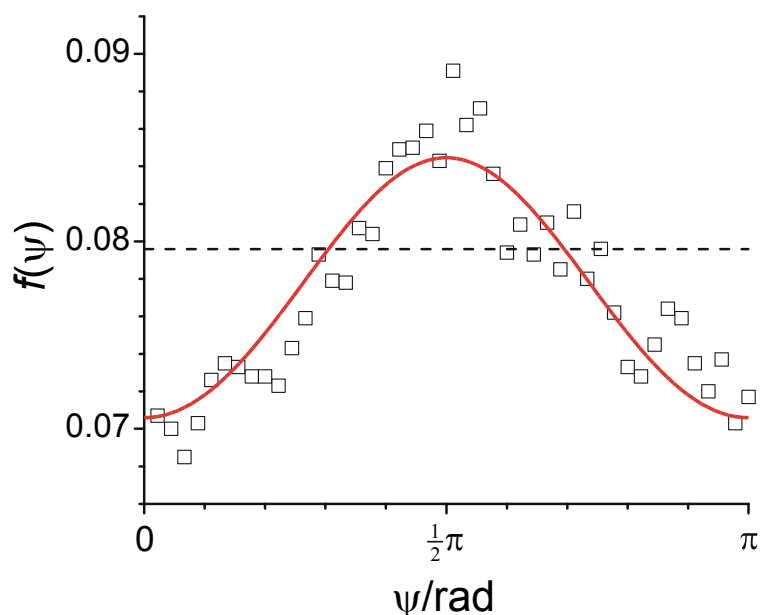


Figure 4.5 – An example of the ODF $f(\psi)$ that was obtained from the SAXS patterns (of the same sample as used in Fig. 4.4, $\phi = 0.05$, $B^2 = 40$ T², and $q = 0.2$ nm⁻¹). The solid line is a fit using Eq. (4.29), yielding $K_2 = -0.18$ and $S_2 = -0.004$. The dashed line indicates the isotropic ODF.

$$f(\theta) = \frac{1}{Z} \exp \left[\frac{1}{3} \frac{\Delta\chi B^2 P_2(\cos\theta)}{kT} \frac{1}{1-\phi/\phi^*} \right]. \quad (4.27)$$

This rescaled Boltzmann distribution is valid only for low volume fractions, $\phi/\phi^* \ll 1$. Therefore, in a first analysis, we only use the SAXS patterns at the lowest concentration ($\phi = 0.05$) to obtain $\Delta\chi$. The ODF (as presented in Fig. 4.5) is fitted using a two-parameter fit

$$f(\psi) = K_1 \exp \left[K_2 \cos^2 \psi \right], \quad (4.28)$$

where K_1 is the normalisation constant, taken such that $\int f(\psi) d\Omega = 1$ and

$$K_2 = \frac{1}{2} \frac{\Delta\chi B^2}{kT} \frac{1}{1-\phi/\phi^*}. \quad (4.29)$$

We have performed this procedure for the scattering patterns of the sample at various magnetic fields, and at three intermediate q values to obtain K_2 for $\phi = 0.05$ as a function of q and B^2 . The resulting data are shown in Fig. 4.6. We have fitted the data for each q -value,

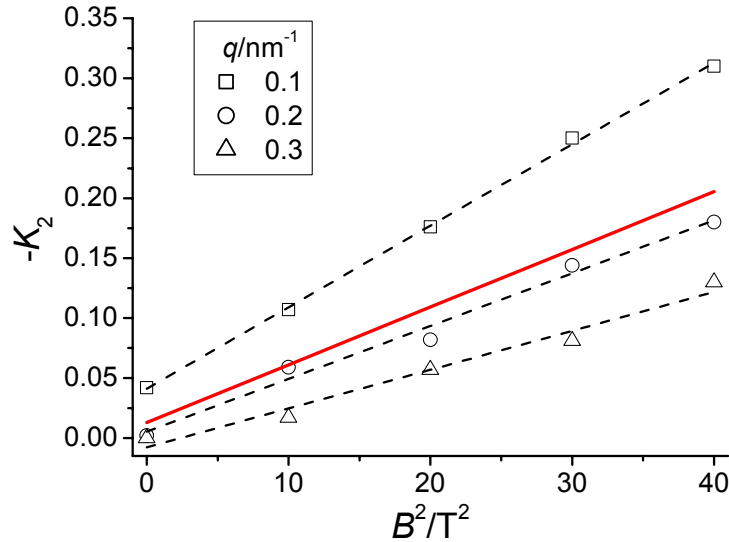


Figure 4.6 – Measurement of the ODF at low volume fraction ($\phi = 0.05$) for three q -values in the intermediate regime. K_2 is related to the ODF through $f(\psi) \propto \exp \left[K_2 \cos^2 \psi \right]$. The dashed lines indicate linear fits through the data at different q -values, while the solid line is a fit through all data points. From the slope of the solid line we obtain $\Delta\chi$.

Chapter 4

as well as the complete data set using two-parameter linear fits, yielding the dashed curves and the solid one, respectively. We attribute the offset of the data to a systematic experimental error. As the effect appears stronger for lower q -values and for low volume fractions, it is probably due to anisotropic parasitic scattering. In view of this offset, we deliberately perform two-parameter fits. As seen in Fig. 4.6, the $q = 0.1 \text{ nm}^{-1}$ -data are better described in this way than with a line through the origin, which supports this approach. From the figure it also appears that the slope of the curves, and hence the value of $\Delta\chi$ to be determined, depends on the q -value where one measures the distribution function. However, as these three q -values cover the intermediate regime, we may assume that the value of $\Delta\chi$ derived in this way is reliable if we take the spread in the slopes (of the individual q -values) as an estimate of the error in $\Delta\chi$.

From Onsager theory for hard platelets it follows that the spinodal concentration has a value in between that of the I-N phase boundaries, and therefore we estimate $\phi^* \cong 0.25 \pm 0.02$. (In the following, it will become evident that this is a reasonable estimate.) Using Eq. (4.29), we hence obtain $\Delta\chi = -3 \pm 1 \times 10^{-23} \text{ J/T}^2$.

We now turn to an analysis of the complete set of data, *i.e.*, we use the scattering patterns for all volume fractions ($0.05 < \phi < 0.219$) and magnetic fields, in order to obtain $\Delta\chi$ and ϕ^* . From Fig. 4.6, it is observed that the slope of the solid fit (for all q -values) is close to that of the fit of $q = 0.2 \text{ nm}^{-1}$. Given the error in the slope, we proceed to perform the current complete analysis only for $q = 0.2 \text{ nm}^{-1}$ and treat the resulting values as

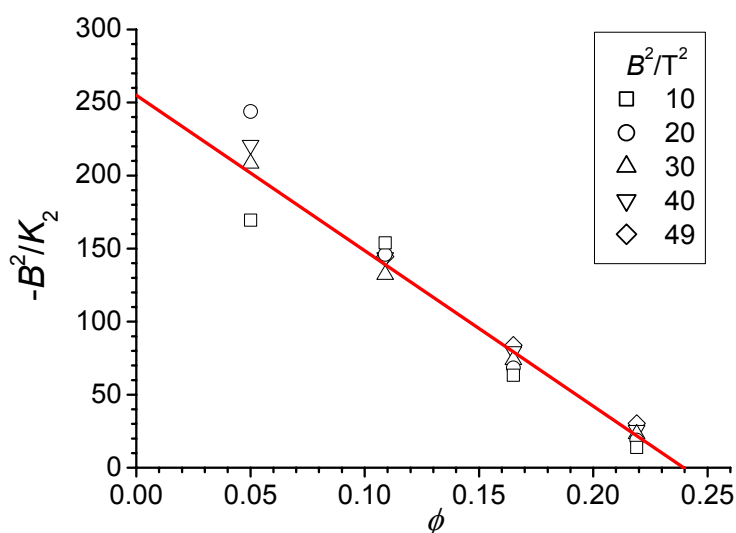


Figure 4.7 – Measurement of the ODF for the complete range of volume fractions and field strengths at $q = 0.2 \text{ nm}^{-1}$. The solid line is a linear fit, yielding $\Delta\chi = -3 \pm 1 \times 10^{-23} \text{ J/T}^2$ and $\phi^* = 0.24 \pm 0.02$. The spread in the data, for different field strengths, is an estimate of the error in this analysis.

representative for the intermediate q -regime. We have checked that this is the case for $\phi = 0.219$ as well.

In the same way as described above, the ODFs are obtained from the SAXS patterns and fitted using Eq. (4.28). Plotting $-B^2/K_2$ vs. ϕ yields Fig. 4.7. We take a linear fit through the data and obtain $\Delta\chi = -3 \pm 1 \times 10^{-23} \text{ J/T}^2$ and $\phi^* = 0.24 \pm 0.02$, where the spread in the data is an estimate of the error in the last two values. Our earlier estimate of the spinodal volume fraction indeed agrees with the experimental value obtained here. In addition, it lies in between ϕ_l and ϕ_N . Table 4.1 lists the results obtained in this section.

To get an impression of the magnitude of the alignment, we calculate the order parameter from the scattering data, for each field strength and volume fraction. As we take discrete data points rather than the analytical expression for the ODF, we use the following expression

$$S_2 = 2\pi \int_0^\pi P_2(\cos\psi) f(\psi) \sin\psi d\psi \cong 2\pi \frac{\pi}{n} \sum_{i=1}^n P_2(\cos\psi_i) f(\psi_i) \sin\psi_i. \quad (4.30)$$

The calculated order parameters are shown in Fig. 4.8. For the most concentrated sample at highest field strength, $S_2 = -0.18$, which is about one third of the maximum value possible ($-\frac{1}{2}$) in this symmetry.

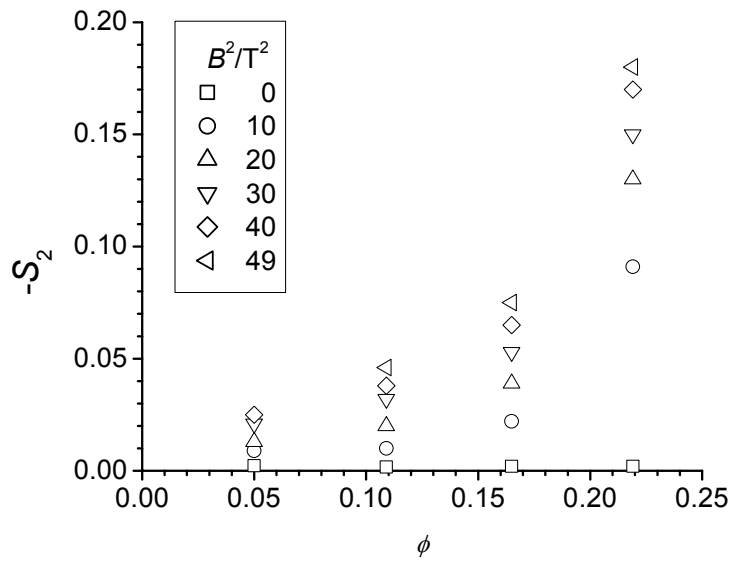


Figure 4.8 – The order parameter S_2 as calculated from the scattering patterns using Eq. (4.30).

4.4.2 Ellipticity analysis

In the previous section, we have obtained the values of $\Delta\chi$ and ϕ^* where we made use of the very direct relation between the ODF and the scattered intensity. Here, we approach the same SAXS patterns in a different way, using the same relation. The iso-intensity lines appear to be well described by ellipses, as has been observed before in the case of aligned Laponite platelets [118].

We first attempt to analyse our data using our simple model. Using home-written image analysis software, we determined the ellipticity, defined as the ratio of the long and short axes b/a , of the iso-intensity lines for each SAXS pattern at q -values from 0.1 to 0.4 nm^{-1} . Fig. 4.9 shows how the ellipticity varies with q_A , defined as the wave vector of the minor (horizontal) ellipse axis (see Fig. 4.3), for a selection of 5 samples. (These are: each volume fraction at the highest field strength, as well as a sample at zero field.)

Let us define two points A and B along a given iso-intensity line such that $\psi_A = 0$ and $\psi_B = \pi/2$. Obviously, $I(A) = I(B)$ and hence it follows from Eq. (4.24) that

$$\frac{b}{a} = \frac{q_B}{q_A} = \sqrt{\frac{q_B^2}{q_A^2}} = \sqrt{\frac{f(\pi/2)}{f(0)}}. \quad (4.31)$$

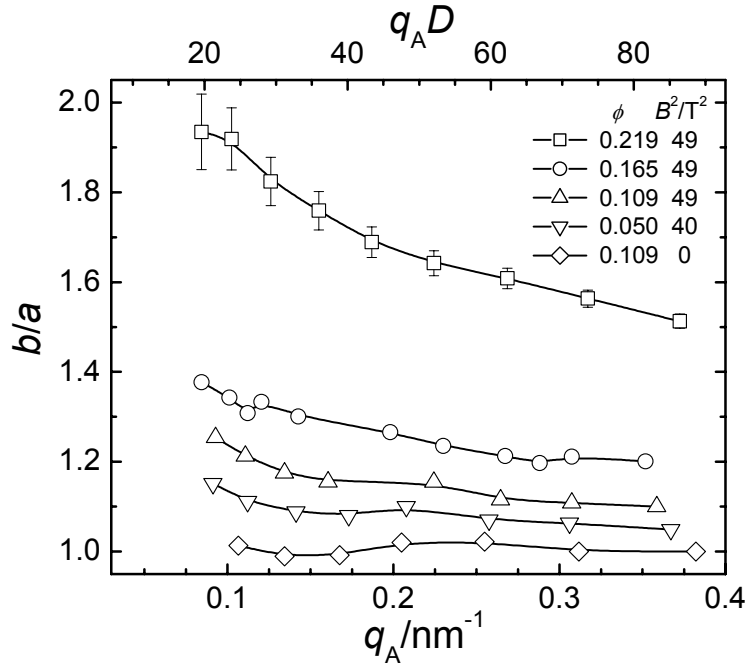


Figure 4.9 – Ellipticity b/a of several SAXS patterns as a function of q_A , defined as the wave vector of the minor axis of the ellipse-like iso-intensity line, see also Fig. 4.3. The q -range in this graph covers the intermediate regime. The error bars on the top curve are representative for the error on all curves.

Note that, although we explicitly use two values of q , our model assumes no q -dependence of the ellipticity b/a . Substituting the ODF (Eq. (4.12)), we obtain

$$\ln\left[\frac{b}{a}\right] = -\frac{1}{4} \frac{\Delta\chi B^2}{kT} \frac{1}{1-\phi/\phi^*}. \quad (4.32)$$

This equation relates the measured ellipticity b/a to $\Delta\chi$ and ϕ^* . Following the same argument as in the previous section, we analyse our data at low volume fraction first ($\phi = 0.05$). We plot $\ln[b/a]$ vs. B^2 for three intermediate values of q in Fig. 4.10, and take linear fits through each of the three data sets, as well as the entire set. The slope of the latter yields $\Delta\chi = -3 \pm 1 \times 10^{-23} \text{ J/T}^2$, where again we took the spread in the slopes of the individual fits (in Fig. 4.10) as an estimate of the error and $\phi^* \cong 0.24$ as obtained in the previous section.

We proceed to perform the complete analysis (for all volume fractions) using only the scattering anisotropy at $q = 0.2 \text{ nm}^{-1}$ as representative for the intermediate regime. A plot of $B^2/\ln[b/a]$ vs. ϕ is shown in Fig. 4.11, and yields a straight line that can be fitted using

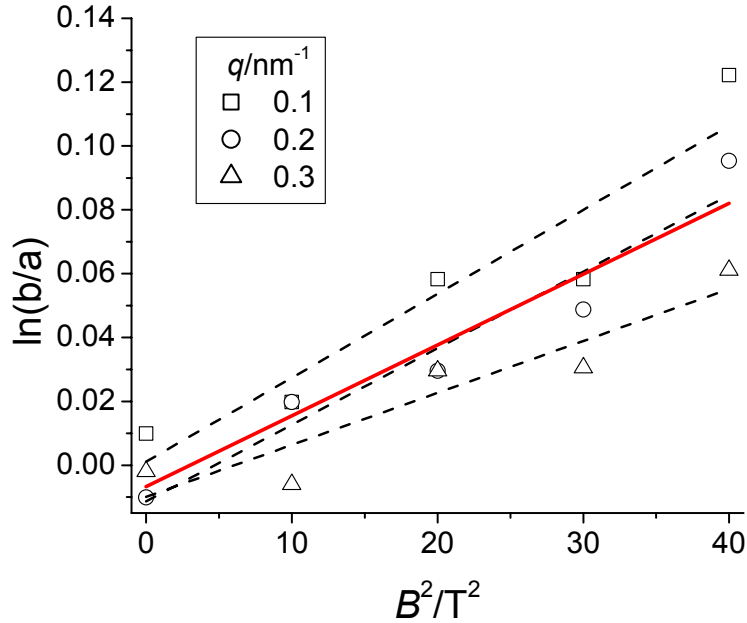


Figure 4.10 – Ellipticity analysis at low volume fraction ($\phi = 0.05$), for three intermediate q -values. The dashed lines indicate linear fits through the data at different q -values, while the solid line is a fit through all data points. From the slope of the solid line we obtain $\Delta\chi$.

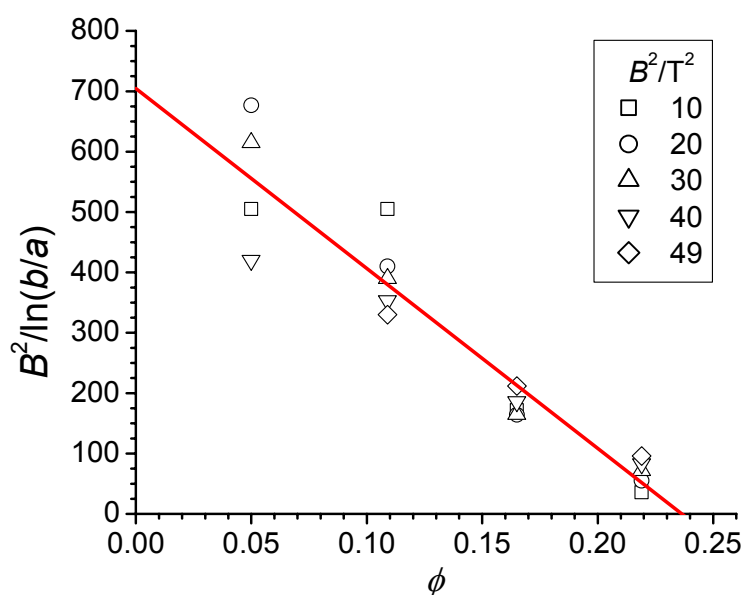


Figure 4.11 – Ellipticity analysis for the complete range of volume fractions and field strengths at $q = 0.2 \text{ nm}^{-1}$. The solid line is a linear fit, yielding $\Delta\chi = -2 \pm 1 \times 10^{-23} \text{ J/T}^2$ and $\phi^* = 0.24 \pm 0.03$. The spread in the data, for different field strengths, is an estimate of the error in this analysis.

$\Delta\chi$ and ϕ^* as parameters. We obtain $\Delta\chi$ and ϕ^* that agree with the values obtained in the previous section; see Table 4.1. However, a serious drawback of our model is that it assumes that the scattering anisotropy is constant in the intermediate regime. As judged from Fig. 4.9, this is clearly not the case. We therefore performed theoretical calculations of the scattering patterns, which show better agreement with our experimental results.

4.4.3 Theoretical calculations of the scattering patterns

We observe that the ellipticity of the iso-intensity lines in the experimental scattering patterns decays with q , while it is assumed constant in our simple model. To investigate this discrepancy, we performed theoretical calculations of the scattering patterns using the Boltzmann ODF for non-interacting platelets (Eq. (4.6)) and the form factor of a cylindrical

Table 4.1 – Values of the diamagnetic susceptibility anisotropy $\Delta\chi$ and spinodal volume fraction ϕ^* , obtained in from the scattering patterns following the ODF and ellipticity analyses.

	ODF analysis		ellipticity analysis	
	$\phi = 0.05$	all ϕ 's	$\phi = 0.05$	all ϕ 's
$\Delta\chi / 10^{-23} \text{ J/T}^2$	-3 ± 1	-3 ± 1	-3 ± 1	-2 ± 1
ϕ^*	–	0.24 ± 0.02	–	0.24 ± 0.03

disk (Eq. (4.17)) with an aspect ratio $L/D=1/18$, following Lemaire and co-workers [118]. Clearly, this approach only holds for low concentrations and we will therefore compare our calculations with the experimental scattering pattern of the sample with $\phi = 0.05$, at $B^2 = 40 \text{ T}^2$. We calculate the scattering patterns of the monodisperse cylindrical disks for two values of the Boltzmann factor, *i.e.*, $\hat{B} = \frac{1}{2}\Delta\chi B^2/kT = -0.2$ and $\hat{B} = -1$, corresponding to $\Delta\chi = -4 \times 10^{-23}$ and $-2 \times 10^{-22} \text{ J/T}^2$, respectively. Their iso-intensity lines are ellipse-like and allow for determination of the ellipticity as a function of $q_A D$ (with D the diameter of the disks), as depicted in Fig. 4.12 together with the experimental result. The oscillations in the calculated ellipticity lines are suppressed in the experimental one, most likely due to polydispersity. The experimental curve is in between the calculated ones, indicating that in the experiment $-0.2 > \hat{B} > -1$ and, hence, that we have obtained an underestimate for $\Delta\chi$ with our simple model.

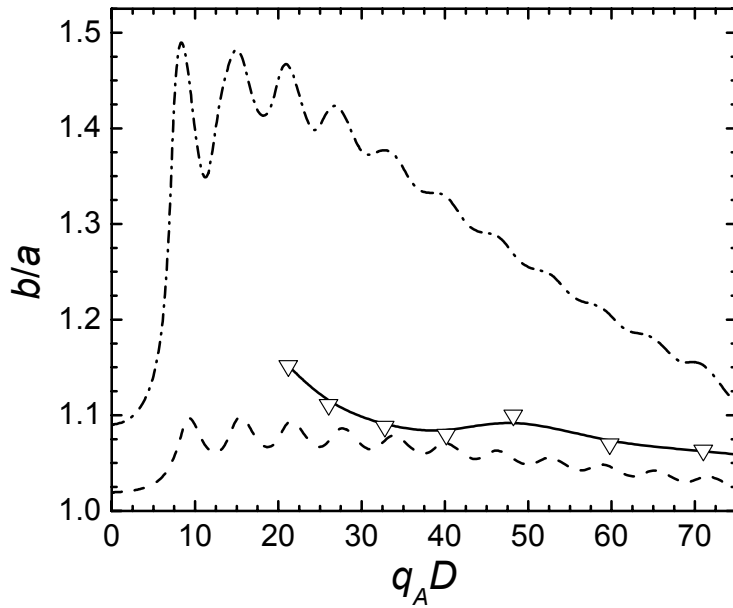


Figure 4.12 – Ellipticity of one experimental and two calculated scattering patterns. The experimental result (of $\phi = 0.05$, $B^2 = 40 \text{ T}^2$, denoted by the open triangles and a solid line to guide the eye) is taken from Fig. 4.9, the calculated patterns were obtained using the form factor of a cylindrical disk with $L/D=1/18$ and the Boltzmann ODF for non-interacting plates with $\hat{B} = \frac{1}{2}\Delta\chi B^2/kT = -0.2$ (dashed line) and $\hat{B} = -1$ (dash-dotted line). The calculated lines show a maximum around $q_A D \approx 10$ that is not observed experimentally due to the limited q -range.

Chapter 4

4.4.4 General discussion

The two procedures that we followed in analysing our data are both based on the same simple relation between the scattered intensity and the ODF, a relation that we have derived in Section 4.2.2. Let us now briefly discuss the model and how it limits our analysis.

First of all, by using the Boltzmann factor for the magnetic energy, we restrict ourselves to near-ideal systems ($\phi \approx 0$). However, by introducing a rescaled version, the model should hold for not too high finite volume fractions ($\phi/\phi^* \ll 1$) as well. Surprisingly enough, from Chapter 5, Fig. 5.3 it appears that – within experimental accuracy – the suspension’s behaviour is well described by this rescaled Boltzmann distribution function, up to $\phi \approx \phi^*$. From both analyses, we find the spinodal volume fraction as $\phi^* = 0.24 \pm 0.03$, which lies in between ϕ_l and ϕ_N . Unfortunately, there is no straightforward method to measure ϕ^* directly.

In the derivation of the ODF we have used Straley’s result for weakly aligned states (expressed mathematically as $\varepsilon \ll 1$ or $S_2 \ll \frac{1}{5}$), allowing only a slight perturbation from the isotropic state. Beforehand, one would expect this condition to be met only at low volume fractions or at low fields. From Fig. 4.8 we find that the most concentrated sample at highest field strength has $S_2 = -0.18$, which is about $\frac{1}{5}$, hence, the sample is certainly not ‘weakly aligned’. However, we find good agreement between the values of $\Delta\chi$ obtained at low and high volume fractions, as well as between the separate analyses, leading to the conclusion that $\Delta\chi = -3 \pm 1 \times 10^{-23} \text{ J/T}^2$. However, in view of the theoretical calculations, we note that the value obtained is a lower bound. The limitations of our simple model become evident in the rather large error in $\Delta\chi$.

4.5 Conclusion

We have shown that colloidal gibbsite platelets form a nice model system in the study of magnetic-field-induced orientational ordering of platelets. The diamagnetic susceptibility anisotropy $\Delta\chi$ is high enough to generate considerable effects at moderate field strengths, yielding a maximal $S_2 = -0.18$. In our analysis, we take a rescaled Boltzmann expression for the orientational distribution function. Given the special properties of the form factor of a plate-like particle in the so-called intermediate regime, we propose a simple model for the scattered intensity in this regime, making it a very transparent and straightforward approach. Although we neglect the q -dependence of the anisotropy of the scattering in our model, we are able to perform an analysis that does our data justice. The obtained value of the diamagnetic susceptibility anisotropy is likely an underestimate. In the next chapter we will study the magnetic-field-induced alignment using an optical technique and indeed

obtain a diamagnetic susceptibility anisotropy that is significantly higher. Although the technique employed there is much more sensitive, it does not provide direct access to the distribution function as in this study.

Appendix

In this appendix we will show that the scattering of plate-like particles is strongly directed along their normals, validating the approach in Section 4.2.2. We focus on the intermediate range, where $\frac{2\pi}{D} \ll q \ll \frac{2\pi}{L}$. In this range, there is a significant difference between the components of the form factor, as was already shown in Fig. 4.2. Fig. 4.13 shows the small ellipse-like region, or central peak, where most of the scattering is found.

Let us define xyz Cartesian coordinates as in Fig. 4.1. The platelet normal \hat{e}_{\parallel} then takes the form $\hat{e}_{\parallel} = (\sin \theta \cos \varphi, \sin \theta \sin \varphi, \cos \theta)$. We need to calculate the scattered intensity of an ensemble of platelets at a given position on the detector, *i.e.*, for a given value of the scattering vector $\vec{q} = (q_x, 0, q_z) = q(\sin \psi_0, 0, \cos \psi_0)$. (We use small-angle approximation here, hence, $q_y \cong 0$.) From Fig. 4.13 it follows that the strongest contribution at this position comes from particles with their normals along the scattering vector, $\hat{e}_{\parallel} \parallel \vec{q}$, *i.e.*, those that have the orientation $\theta = \psi_0$ and $\varphi = 0$. We extend this to the particles that have

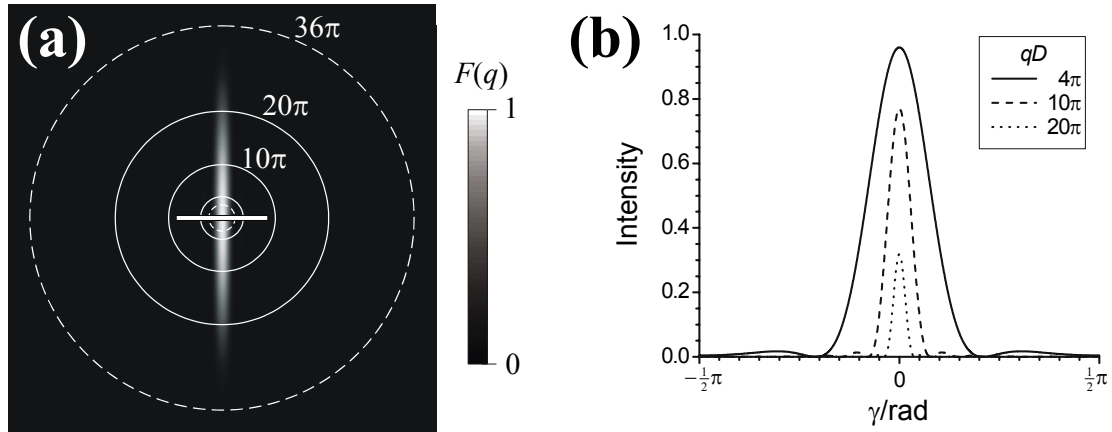


Figure 4.13 – The scattering of a plate-like particle is strongly directed along its normal, as demonstrated by (a) the form factor $F(q)$ of a plate-like particle with $L/D=1/18$. As this is a planar cut through the three-dimensional Fourier space, the central peak is in fact a three-dimensional ellipsoid-like object rather than a two-dimensional ellipse-like object. For clarity, a disk with the same aspect ratio and analogous orientation is projected in the scattering pattern. For three circles, the corresponding qD -value is given. The dashed circles give the extremes of the intermediate regime; the solid circles indicate the azimuthal paths along which we calculate the scattered intensity that is given in (b) for $qD = 4\pi, 10\pi,$ and 20π .

Chapter 4

$\gamma < \Delta\gamma$, where $\Delta\gamma(q) = \arctan(q_0/q)$ and $q_0 = 3.83/\frac{1}{2}D$ is the first minimum of F_{\perp} . As a result we only count 80% of the scattering. The remaining 20% comes from particles with $\gamma > \Delta\gamma$. For the particles under consideration (with $L/D = 1/18$), $\Delta\gamma$ is approximately 8° at $q = \pi/L$, demonstrating that we indeed have a very narrow scattering peak.

5

Magnetic birefringence study of the isotropic phase of colloidal gibbsite platelets

Abstract

We have studied the magnetic birefringence of a system of colloidal gibbsite platelets dispersed in toluene. Due to the relatively large diamagnetic susceptibility anisotropy $\Delta\chi$, isotropic suspensions of these platelets readily align in magnetic fields up to 2 T. We measure the field-induced birefringence of the suspensions as a function of volume fraction and use the model derived in the previous chapter to analyse our data. We obtain a value of $\Delta\chi$ that is slightly higher than that obtained in the previous chapter.

5.1 Introduction

One of the most striking features of liquid crystals (LCs), and perhaps also the most exploited one, as evidenced from *e.g.* the ubiquitous liquid crystal displays (LCDs) that surround us in everyday life, is their birefringence. The orientational order in LCs can be achieved by lowering the temperature (for thermotropic LCs) or increasing the concentration (for lyotropic ones). However, it is perhaps even more easily imposed by an external electric or magnetic field. Moreover, any external field that takes advantage of the anisotropic properties of the (macro) molecules under consideration is suitable [119].

Here, we present a study of the birefringence in an isotropic dispersion of colloidal gibbsite platelets (a so-called mineral liquid crystal or MLC [120,121]), induced by a magnetic

Chapter 5

field. As has been shown in the previous chapter, this specific MLC is quite susceptible to a magnetic field, allowing a small-angle X-ray scattering (SAXS) study of the orientational order and providing direct access to the orientational distribution function (ODF).

Measurement of the birefringence is a well-known technique that allows measurement of the field-induced orientational order and that has been employed before on various kinds of liquid crystals. Examples of these include the classic thermotropic LCs 5CB [122] and MBBA [123]. Among the lyotropic LCs are (bio) polymers like DNA [124], hard rods like tobacco mosaic virus (TMV) [109,125], *fd* [110-112] virus particles, and goethite rods [25,105].

In contrast to the SAXS measurements performed in the previous chapter, the current technique does not provide the ODF, but only its second moment: the order parameter S_2 . We further require knowledge of the specific birefringence Δn_{sat} , *i.e.*, the value of the birefringence of a completely aligned sample of anisotropic particles (with $S_2 = 1$), divided by its volume fraction; see Eq. (5.1). In such an aligned sample, the specific birefringence is determined solely by the optical anisotropy of the single particles. Bragg and Pippard [126] have noted that the optical anisotropy of a macromolecule is “*due partly to the intrinsic birefringence of the molecule itself, and partly to the elongated form of large molecules of high refractive index which are immersed in a liquid of lower refractive index*”. For our gibbsite particles both contributions are expected, as the particles have a slight refractive index-difference along their three perpendicular axes ($n_a = n_b = 1.57$, $n_c = 1.59$ [127]) as well as a substantial difference with the solvent in combination with a quite pronounced shape anisometry. However, we will show that these contributions counteract. In this study, we aim to investigate the magnetic-field-induced order using optical techniques. Using the rescaled Boltzmann distribution function that was introduced in the previous chapter, we analyse our data in order to find the diamagnetic susceptibility anisotropy.

5.2 Field-induced birefringence

A classic way of determining the pretransitional order in liquid crystals is by measuring the field-induced birefringence [105,108,110,119,122-125,128-131]. It has been suggested that the birefringence Δn of a dilute isotropic colloidal suspension is given by [105,132]

$$\Delta n = \Delta n_{\text{sat}} \phi S_2, \quad (5.1)$$

where Δn_{sat} is the specific birefringence, ϕ the volume fraction and S_2 the order parameter. Note that the specific birefringence does not depend on the concentration, nor the amount and direction of alignment of the particles.

Magnetic birefringence study of the isotropic phase of colloidal gibbsite platelets

In this study, the orientation is induced by a magnetic field. In Section 4.2.1, Eq. (4.11), we have shown how, for low volume fractions, the order parameter S_2 depends on $\Delta\chi$ and B and repeat this result here:

$$S_2 = \frac{1}{15} \frac{\Delta\chi B^2}{kT} \frac{1}{1 - \phi/\phi^*}. \quad (5.2)$$

In the derivation of this expression, it is assumed that the particles are only weakly aligned. It will be shown that this requirement is fulfilled. Substitution of Eq. (5.2) into (5.1) gives

$$\Delta n = \frac{1}{15} \frac{\Delta n_{sat} \Delta\chi B^2}{kT} \frac{\phi}{1 - \phi/\phi^*}. \quad (5.3)$$

Rewriting yields

$$\frac{\Delta n}{B^2} = \frac{1}{15} \frac{\Delta n_{sat} \Delta\chi}{kT} \frac{\phi}{1 - \phi/\phi^*}, \quad (5.4)$$

which relates the observed field-induced birefringence $\Delta n/B^2$ to the magnitude of $\Delta n_{sat} \Delta\chi$. Apparently, we may expect linear behaviour of $\Delta n/B^2$ vs. ϕ at low volume fractions ($\phi/\phi^* \ll 1$) when there are only individual interactions of the platelets with the magnetic field, while it should diverge on approaching the spinodal concentration ϕ^* due to the collective effect of the platelets.

5.3 Experiment

5.3.1 Preparation and characterisation

In this study we make use of sterically stabilised colloidal gibbsite platelets in toluene, synthesised according to the procedures in the literature [22,45,50]. We use the same batch that was used in Chapter 4 and refer to it for the experimental details of the preparation and characterisation (see Section 4.3.1). In addition to the described procedure, the stock dispersion used in this study was purified to remove some contamination, visible as a black layer at the I-N interface. We simply extracted the contamination by using a small pipette. Due to this extra step, the stock dispersion has slightly different characteristics, *e.g.*, the isotropic and nematic phase boundaries are shifted to somewhat higher volume fractions.

Chapter 5

5.3.2 Samples and methods

In order to obtain the most concentrated isotropic stock dispersion, we brought the purified stock dispersion in the I-N biphasic gap. After phase separation, which took 1 day, the amounts of isotropic and nematic phase were about 90% and 10%, respectively. Both phases were extracted. The nematic fraction was used to study the effect of a magnetic field on a wall-aligned nematic phase (the Frederiks transition), as described in Chapter 7 of this thesis.

The volume fraction of the isotropic phase was determined to be $\phi = 0.229$, following the method described in Section 4.3.2. It was used to prepare 11 samples in spectrophotometric cells with volume fractions ranging from $\phi = 0.02$ to $\phi = 0.246$. In spite of carefully sealing the cells with Teflon tape, evaporation of the solvent could not be prevented, causing a shift of the samples' volume fraction to slightly higher values with time. We kept track of the actual volume fraction by weighing each sample before performing the birefringence measurements. The path length of the cells d was chosen such that it increased from 1.00 mm to 10.00 mm with decreasing volume fraction to counterbalance the lower birefringence at lower concentration.

The birefringence was measured using a technique based on the modulation of the state of polarisation of the light [133]. This setup is suited to measure the linear birefringence Δn very sensitively, as demonstrated by our measurement of the field-induced birefringence of toluene (the solvent).

The setup, similar to that described in Ref. [105], used a green He-Ne laser ($\lambda = 543.5$ nm), a vertical polariser, a photoelastic birefringent modulator with its main optical axis at 45° from the vertical direction and oscillating at a frequency $\nu = 50$ kHz to avoid the influence of mechanical vibrations, the sample immersed in a horizontal magnetic field perpendicular to the light beam, an analyser at 45° from the vertical direction and a photomultiplier as a detector. A lock-in amplifier measures the component of the photomultiplier signal I_ν at the modulation frequency ν , which is related to the birefringence Δn by

$$I_\nu = I_0 \sin \frac{2\pi\Delta n d}{\lambda}, \quad (5.5)$$

where I_0 is kept constant and determined by calibration. The alternating magnetic field was generated by an electromagnet, sweeping with a triangular type of modulation from -0.8 T to 0.8 T and a period of 49 s, which was much larger than the typical response time of an isotropic solution (measured to be in the range 10-100 ms, depending on volume fraction) to ensure orientational equilibrium of the particles.

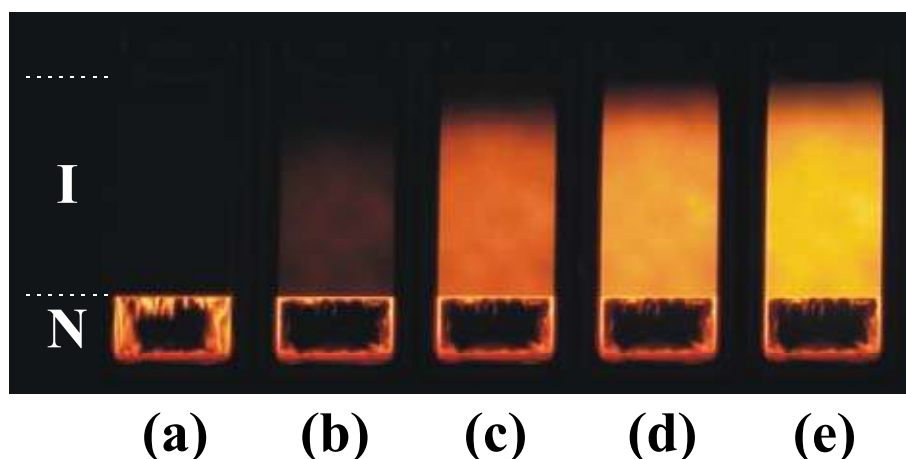


Figure 5.1 – Illustration of the magnetic-field-induced birefringence in the isotropic phase of the suspensions of sterically stabilised colloidal gibbsite platelets. An isotropic-nematic sample with path length $d = 2.00$ mm is placed between crossed polarisers in a horizontal magnetic field (a) 0, (b) 0.5, (c) 1, (d) 1.5, and (e) 2.0 T, generated using a Bruker BE25v Electromagnet. The sample is observed between crossed polarisers, making angles of -45° and 45° with the vertical direction. As can be seen quite clearly, the birefringence in the isotropic phase increases with increasing magnetic field. The black patch in the nematic phase, which increases in size with the field strength, is caused by so-called homeotropic anchoring of the platelets on the front and back walls of the cell. This phenomenon is studied in Chapter 7. The birefringence gradient observed at the top of the sample is due to sedimentation of the particles. (See colour version at page 134.)

5.4 Results and discussion

To illustrate the magnetic birefringence of the suspension of colloidal gibbsite platelets, we show the field-induced birefringence as recorded with a digital camera. This simple qualitative experiment was performed using a different biphasic (isotropic and nematic) sample in a spectrophotometric cell (path length $d = 2.00$ mm), immersed in a horizontal magnetic field and put between crossed polarisers (both making an angle of 45° with the vertical). Fig. 5.1 depicts this sample and the increase of the birefringence of the isotropic phase with magnetic field. Using a rough estimate $d\Delta n \approx \lambda_{opt}/10$ [118] ($\lambda_{opt} \approx 0.6 \mu\text{m}$ the wavelength of the orange transmitted light) of the birefringence that can be detected with the naked eye, we evaluate the field-induced birefringence $\Delta n/B^2$ in the coexisting isotropic phase. From Fig. 5.1, we observe that the birefringence becomes visible around $B \approx 0.5$ T, yielding $|\Delta n|/B^2 \approx 10^{-4} \text{ T}^{-2}$. Later on we will show that this is indeed about the right order of magnitude.

Measurement of the field-induced birefringence yields Δn vs. B -curves, of which a typical one is shown in Fig. 5.2. The birefringence is proportional to B^2 . At the highest volume fractions, the curves showed some hysteresis, likely due to the fact that the samples had entered the biphasic gap. Still, the hysteresis was small enough to accurately determine

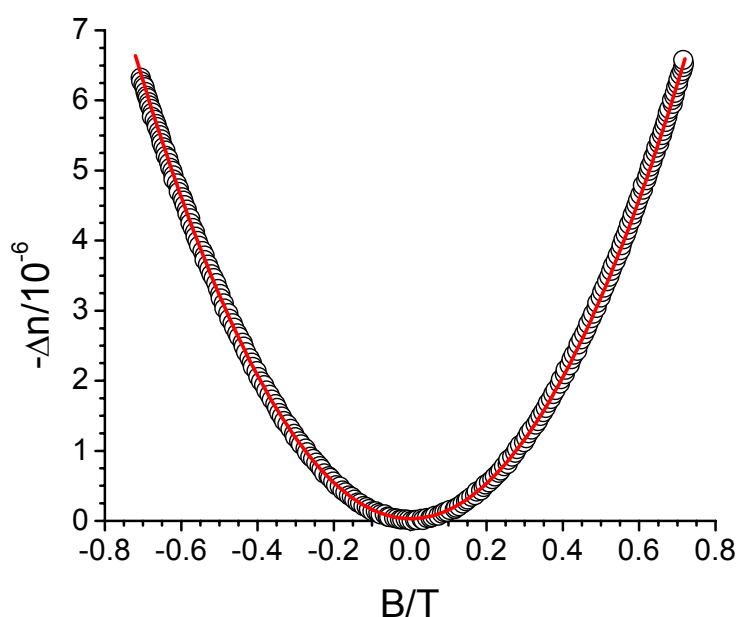


Figure 5.2 – Typical curve obtained from the measurement of the field-induced birefringence, in this case for a sample with $\phi = 0.219$ and $d = 1.00$ mm. The open dots indicate measured data; the solid curve is a parabolic fit through the data, demonstrating that $-\Delta n \propto B^2$.

$\Delta n/B^2$ by linearly fitting the Δn vs. B^2 curves. The volume fraction-dependent field-induced birefringence is depicted in Fig. 5.3. As a demonstration of the setup sensitivity and as a background check, we have measured the field-induced birefringence of the solvent (toluene) as well, and found a value of $\Delta n/B^2 = 2.5 \times 10^{-9} \text{ T}^{-2}$. The so-called Cotton-Mouton constant K_{CM} is obtained as $K_{CM} = \Delta n/\lambda B^2$, where λ is the wavelength at which it was determined. From the literature values [134] of the Cotton-Mouton constants of benzene ($7.84 \times 10^{-3} \text{ T}^{-2}\text{m}^{-1}$) and p-xylene ($8.17 \times 10^{-3} \text{ T}^{-2}\text{m}^{-1}$), measured at $\lambda = 488$ nm, we estimated that of toluene at $7 \times 10^{-3} \text{ T}^{-2}\text{m}^{-1}$ at our experimental wavelength. Our measured $K_{CM} = 5 \times 10^{-3} \text{ T}^{-2}\text{m}^{-1}$, which is slightly lower than the (estimated) literature value.

For the coexisting isotropic phase, at $\phi = 0.24$, the field-induced birefringence is about $2 \times 10^{-5} \text{ T}^{-2}$. This is indeed of the same order of magnitude as the value we (very crudely) estimated above. We are able to make an estimate of the order parameter in this sample. Using Eq. (5.2), $\phi = 0.24$, $\phi^* = 0.26$, $B = 0.8$ T, and $\Delta\chi = -2 \times 10^{-22} \text{ J/T}^2$ as obtained later on, we find that $S_2 = -0.03$, indicating that the condition for weakly aligned states is satisfied. The value of $\Delta n/B^2$ of our isotropic suspension of colloidal gibbsite ($\text{Al}(\text{OH})_3$) platelets falls in between those of metal oxide and organic colloidal rods, see Table 5.1. This is understood on the basis of the electronic structure of the constituent atoms (*d*-block

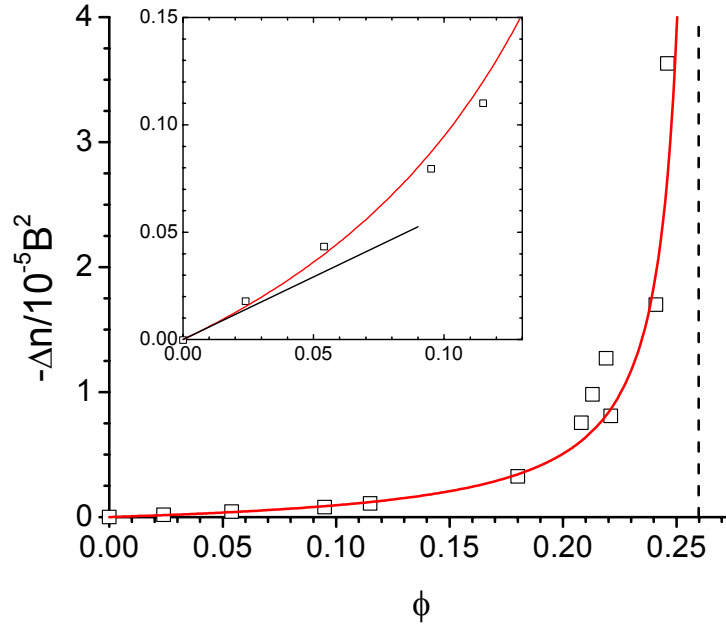


Figure 5.3 – Field-corrected birefringence $-\Delta n/B^2$ vs. volume fraction. This graph shows that the field-induced birefringence diverges near the spinodal volume fraction ϕ^* , obtained from the fit in Fig. 5.4 and indicated by the dashed line. The inset shows the low volume fraction region, with the solid black line as the tangent to the fit at $\phi = 0$, indicating ideal behaviour as described by the Boltzmann ODF. The rescaled Boltzmann ODF is able to describe the collective behaviour, almost up to ϕ^* , very well.

Table 5.1 – Magneto-optical properties of several anisotropic colloidal particles, including plate-like gibbsite particles studied in this thesis. To give an impression of the different shapes of the particles, we present the particles' length (L), diameter (D), width (W), and thickness (T). We furthermore make a comparison of the magnetic-field-induced birefringence $\Delta n/B^2$ in the isotropic suspensions at I-N coexistence. In order to make a fair comparison, we correct it for the volume fraction and have therefore calculated $\Delta n/\phi_i B^2$. The right-most column gives the diamagnetic susceptibility anisotropy per particle.

particle	dimensions	ϕ_i	$ \Delta n /\phi_i B^2 / \text{T}^{-2}$	$\Delta\chi / 10^{-23} \text{ J/T}^2$
goethite lathe	$L = 150 \text{ nm}, W = 25 \text{ nm}, T = 10 \text{ nm}$ [105]	0.06 [105]	0.5 [105]	-2200 [105]
V ₂ O ₅ ribbon	$L \approx 200 \text{ nm}, W = 10 \text{ nm}, T = 1 \text{ nm}$ [137]	0.01 [137]	0.7 [105]	–
TMV rod	$L = 300 \text{ nm}, D = 18 \text{ nm}$ [138]	0.3 [109]	5×10^{-7} [109]	0.2 [108,109,125]
<i>fd</i> virus rod	$L = 900 \text{ nm}, D = 6.5 \text{ nm}$ [139]	0.02 [111]	5×10^{-6} [21]	0.5 [113,140]
<i>Pf1</i> virus rod	$L = 2000 \text{ nm}, D = 6 \text{ nm}$ [113]	–	–	1.2 [113]
gibbsite plate	$D = 237 \text{ nm}, T = 18 \text{ nm}$	0.24	8×10^{-5}	-10 ± 5

Chapter 5

atoms like Fe and V in contrast to *p*-block elements like Al, C and N) as well as the particle volume (which is higher for platelets than for rods with the same dimensions).

The volume-fraction-dependent field-induced birefringence follows the behaviour that was sketched at the end of section 5.2: at low volume fraction ($\phi < 10\%$), the curve shows almost linear behaviour, as shown in the inset in Fig. 5.3, while it diverges near ϕ^* . Although the rescaled Boltzmann ODF was derived for not too high volume fractions ($\phi/\phi^* \ll 1$), it is able to describe the data surprisingly well, almost up to ϕ^* .

The value of ϕ^* as well as $\Delta n_{sat}\Delta\chi$ can be obtained from our measurements following Lemaire and co-workers [105]. Rewriting Eq. (5.4) we find

$$\frac{\phi B^2}{\Delta n} = \frac{15kT}{\Delta n_{sat}\Delta\chi} \left(1 - \frac{\phi}{\phi^*}\right). \quad (5.6)$$

Plotting $\phi B^2/\Delta n$ vs. ϕ then should yield a straight line with a vertical intercept of $15kT/\Delta n_{sat}\Delta\chi$ and a horizontal intercept at ϕ^* . This indeed appears the case from Fig. 5.4. $\Delta n_{sat}\Delta\chi$ and ϕ^* can be used as linear fit parameters, yielding $-3.6 \pm 0.1 \times 10^{-25} \text{ J/T}^2$ and 0.26 ± 0.03 , respectively. The value for ϕ^* closely agrees with the value obtained in Chapter 4. Now we know the value of $\Delta n_{sat}\Delta\chi$, we will determine the specific

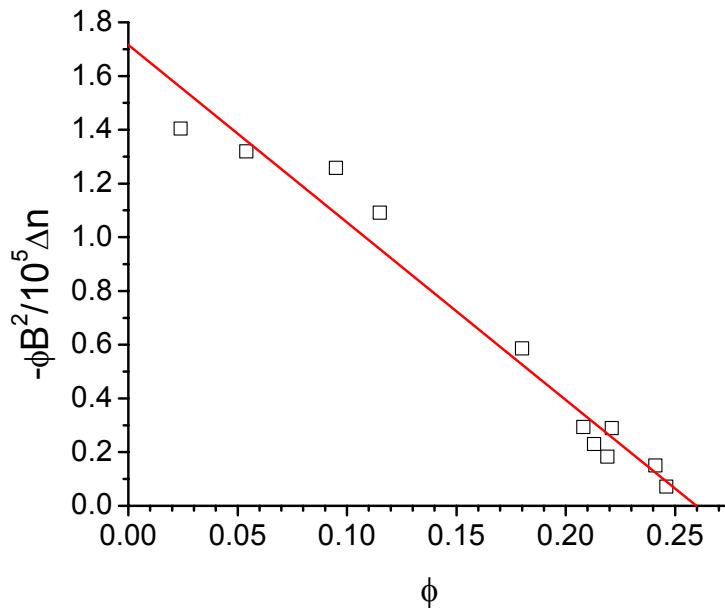


Figure 5.4 – The same information as Fig. 5.3, now in a representation with $\phi B^2/\Delta n$ vs. ϕ . Using Eq. (5.6), we obtain $\Delta n_{sat}\Delta\chi = -3.6 \pm 0.1 \times 10^{-25} \text{ J/T}^2$ and $\phi^* = 0.26 \pm 0.03$ from this graph.

birefringence Δn_{sat} in order to obtain $\Delta\chi$.

According to Eq. (5.1), $\Delta n_{sat} = \Delta n / \phi S_2$ and therefore, we have to determine Δn_{sat} by measuring the birefringence of a completely aligned sample (with $S_2 = 1$) with known volume fraction. In order to prepare completely aligned sample, we improved the orientational order of a nematic phase by rotating it in a magnetic field around an axis perpendicular to the field. Apart from improved alignment, we expect reorientation of the nematic director parallel to the rotation axis. (This is due to $\Delta\chi < 0$, which also results in the positive order parameter that we use below. This is explained in more detail in the next chapter, Section 6.3) We have performed the procedure above to two different samples, whose birefringence was measured in two different ways. First we prepared a nematic phase ($\phi = 0.27$) in a flat optical capillary with thickness $d = 200 \mu\text{m}$. It was rotated in a magnetic field ($B = 1.0 \text{ T}$) for 10 minutes and we used a polarisation microscope to check the alignment before and after measurement of the birefringence, see Fig. 5.5. We observed that the orientational order had relaxed to a certain extent, and therefore estimate the order parameter at $S_2 \approx 0.8$ rather than 1. The birefringence of the sample was measured using an optical birefringent compensator to obtain the specific birefringence as $\Delta n_{sat} = 2.1 \pm 0.5 \times 10^{-3}$. A second nematic phase, in coexistence with an isotropic phase, with $\phi = 0.255$, was prepared in a thicker cell ($d = 2.00 \text{ mm}$) and put in a horizontal magnetic field at $B = 1.4 \text{ T}$. The cell was rotated and Fig. 5.6 shows the evolution of the birefringence in time. The nematic phase, which initially consisted of multiple domains, coalesces completely to form a monodomain nematic phase with its director vertical. Using an interference colour

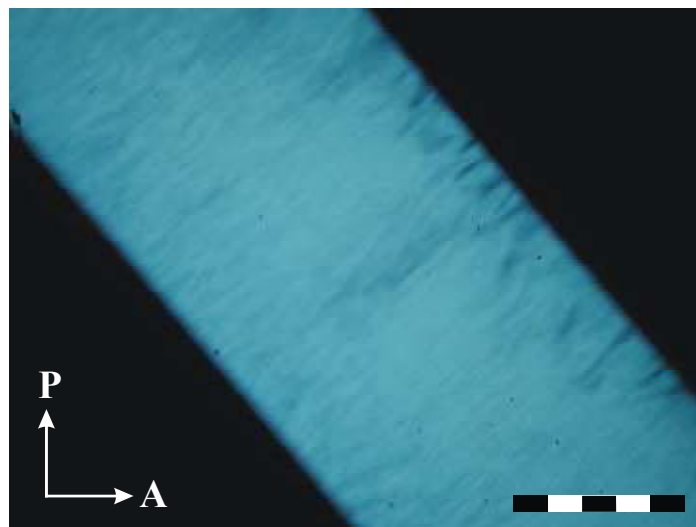


Figure 5.5 – Aligned nematic sample used in the determination of Δn_{sat} . At an angle of 0° with the polariser the sample appeared completely black. The scale bar denotes 1 mm. (See colour version at page 134.)

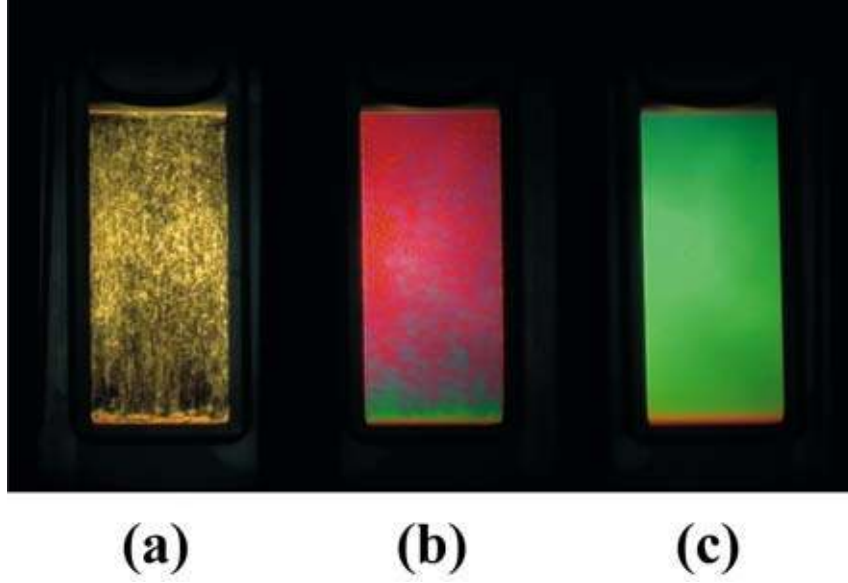


Figure 5.6 – Isotropic-nematic sample in a magnetic field, rotated around its vertical axis at an average rate of 6 revolutions per minute (a) just before starting rotation and after rotating for (b) 1 and (c) 2 minutes. The magnetic field was directed horizontally, $B = 1.4$ T, the polarisers made an angle of -45° and 45° with the vertical direction. Due to this specific geometry, a (uniaxial) nematic phase is prepared with its director along the vertical rotation axis. Using an interference colour chart [135], we find that the green interference colour finally emerging is a “second-order” green, with a retardation $\Delta = 800 \pm 40$ nm. In this specific sample, due to the magnetic field, the amount of nematic phase had increased from 80% to 97%. This phenomenon is described in more detail in Chapter 6. Furthermore, we note that we have in fact induced the Frederiks transition in the sample, *i.e.*, a reorientation of the nematic director field due to a magnetic field. This phenomenon is discussed in Chapter 7. (See colour version at page 135.)

chart [135], we find that the bright green interference colour finally visible is a “second-order” green, with a retardation $\Delta = 800 \pm 40$ nm. We estimate $S_2 \approx 0.8$ and using the relation $\Delta n = \Delta/d$, we find $\Delta n_{sat} = 2.0 \pm 0.5 \times 10^{-3}$ agreeing very well with the first measurement.

We are now able to calculate $\Delta\chi = -2.0 \pm 0.7 \times 10^{-22}$ J/T² and note that this is one order of magnitude higher than the value obtained in Chapter 4.

In order to cross-check the value of the specific birefringence, we calculate it following Lemaire and co-workers using the expression [105,126]

$$\Delta n_{sat} = \frac{n_0}{2} \left[\frac{n_c^2 - n_0^2}{n_0^2 + N_c (n_c^2 - n_0^2)} - \frac{1}{2} \left(\frac{n_a^2 - n_0^2}{n_0^2 + N_a (n_a^2 - n_0^2)} + \frac{n_b^2 - n_0^2}{n_0^2 + N_b (n_b^2 - n_0^2)} \right) \right], \quad (5.7)$$

Magnetic birefringence study of the isotropic phase of colloidal gibbsite platelets

where n_a , n_b , and n_c the refractive indices of the gibbsite platelet along the three crystallographic axes, and N_a , N_b , and N_c the depolarising factors along the same axes. The depolarising factors can be calculated by treating the particles as ellipsoids [136] with the same aspect ratio as the gibbsite core ($L/D = 1/18$), yielding $N_a = 0.04$, $N_b = 0.04$, and $N_c = 0.92$. This in turn yields the specific birefringence as $\Delta n_{sat} = 1.2 \times 10^{-2}$. This value is one order of magnitude larger than measured experimentally. However, we note that the calculation only takes into account the form birefringence. As explained in the introduction, the effective or measured birefringence has two contributions: the intrinsic (material) birefringence and the form birefringence. As these contributions counteract in the case of our gibbsite particles, the discrepancy can be explained. Therefore, in the calculation of $\Delta\chi$ from the value of $\Delta n_{sat} \Delta\chi$, we should use Δn_{sat} as measured in our experiment and, hence, we obtain $\Delta\chi = -2.0 \pm 0.7 \times 10^{-22} \text{ J/T}^2$.

In the previous chapter, we have obtained a value of the diamagnetic susceptibility anisotropy that is considerably lower, $\Delta\chi = -3 \pm 1 \times 10^{-23} \text{ J/T}^2$. However, given the shortcomings of the model employed in Chapter 4, this has to be taken as a lower bound. We hence conclude that the diamagnetic susceptibility anisotropy of our gibbsite platelets can be given as $\Delta\chi = -1 \pm 0.5 \times 10^{-22} \text{ J/T}^2$. In Table 5.1 we present a comparison of the values of $\Delta\chi$ for different anisotropic colloidal particles. It appears that the value of our gibbsite platelets is higher than that of organic rods, and lower than that of the inorganic rod goethite.

5.5 Conclusion

We have studied the magnetic birefringence of an isotropic suspension of sterically stabilised colloidal gibbsite platelets dispersed in toluene. We have measured the birefringence as a function of volume fraction and analysed our data using a rescaled Boltzmann orientational distribution function. In contrast to the study in Chapter 4, we here fulfil the requirement of weakly aligned states. From this and the previous chapter, we obtain the diamagnetic susceptibility anisotropy of our platelets as $\Delta\chi = -1 \pm 0.5 \times 10^{-22} \text{ J/T}^2$. In the next chapters, we will study the effect of the magnetic field on the phase transition densities, as well as the Frederiks transition, both requiring this value of $\Delta\chi$.

Chapter 5

6

Magnetic-field-induced shift of the isotropic-nematic phase transition of colloidal gibbsite platelets

Abstract

We present exploratory experiments of the isotropic-nematic phase behaviour of a suspension of sterically stabilised colloidal gibbsite platelets in a magnetic field. We observe a shift of the phase transition to lower volume fractions with increasing field, in agreement with theoretical calculations. We derive a Clausius-Clapeyron type relation to analyse our experimental results.

6.1 Introduction

In the previous two chapters, we have discussed the influence of the magnetic field on the isotropic phase of our colloidal dispersion of gibbsite platelets. Here, we will focus on the isotropic (I) to nematic (N) phase transition in a magnetic field.

The isotropic to nematic phase transition can be understood on the basis of the so-called Onsager theory. In the 1940s, Onsager has shown why suspensions of anisometric particles – rods or plates – show the I-N phase transition [10,11]. It was demonstrated that the balance between orientational entropy (which favours the isotropic state) and packing entropy (favouring the nematic or aligned state) determines the phase behaviour. At low concentrations, orientational entropy dominates, yielding an isotropic state. As the packing entropy becomes more important at higher concentrations, a first-order phase transition

Chapter 6

from an isotropic to a nematic phase may occur if the concentration of plates or rods is sufficiently high.

On the basis of these considerations, one may already intuitively expect that external (aligning) fields may have an influence on the I-N transition. In 1982, Khokhlov and Semenov [142] put down a theoretical basis for this, by adding an extra term to the Onsager free energy that incorporates the field-induced alignment. Recently, Varga and co-workers [143,144] have used the Parsons-Lee [145-147] rescaling method to describe the phase behaviour of hard rods in an external field. For platelets however, this method is only qualitatively correct [144,148].

As was shown by Khokhlov and Semenov, one can distinguish two scenarios for the alignment of rods or plates in an external quadrupolar field. A particle aligns with its normal \hat{e}_{\parallel} either parallel or perpendicular to the field, depending on the sign of the diamagnetic susceptibility anisotropy $\Delta\chi$. The magnetic energy per particle w_{mag} is given by

$$w_{mag} = -\Phi P_2(\cos\theta), \quad (6.1)$$

where $\Phi = \frac{1}{3}\Delta\chi B^2$; see also Section 4.2.1. It follows that $\hat{e}_{\parallel} \parallel \vec{B}$ for $\Phi > 0$ and $\hat{e}_{\parallel} \perp \vec{B}$ for $\Phi < 0$. We have sketched phase diagrams for both scenarios in Fig. 6.1. As observed in Chapter 4, our particles align with their normals perpendicular to the field and, hence, we deal with the second scenario, shown in Fig. 6.1b.

Evidence for a shift of the I-N transition due to a magnetic field is still limited. A decade ago, Tang and Fraden [111] provided evidence for a magnetic-field-induced I-N phase transition in suspensions of rod-like *fd* virus particles on the basis of the time dependence

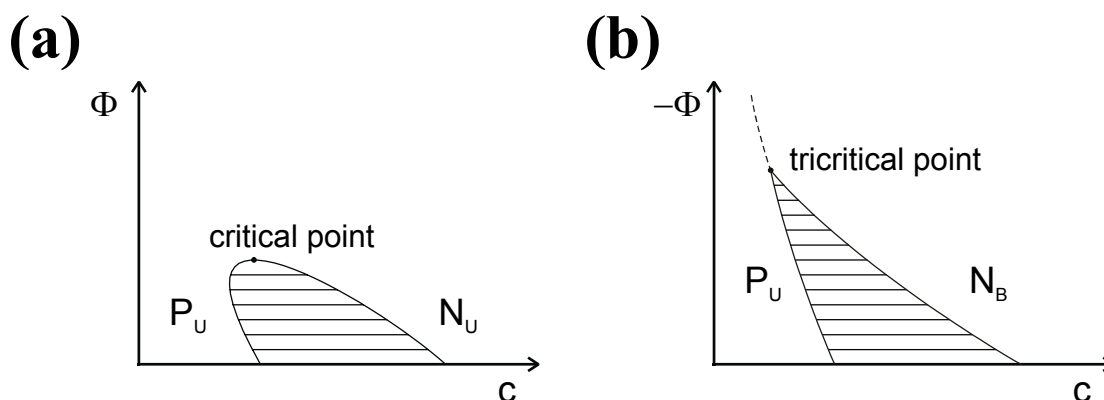


Figure 6.1 – Sketches of the phase diagram of rods or plates in an external field, (a) for positive and (b) for negative values of the field parameter Φ . The solid horizontal lines denote tie lines, c denotes concentration. P and N refer to the paranematic and nematic phases, respectively; U denotes uniaxial and B biaxial symmetry.

of the field-induced birefringence. Recently, Lemaire and co-workers [149] observed that when a magnetic field is applied to a biphasic goethite suspension, “*the isotropic phase acquires a birefringence comparable to that of the nematic phase. At strong enough fields, the meniscus between the two phases fades and finally vanishes on the timescale of a week*”. This strongly suggests the disappearance of the coexistence region typical of the first order character of the I-N transition beyond some value of the magnetic field.

Here, we present visual observations of the shift of the I-N phase transition densities in a colloidal suspension of gibbsite platelets. We show that the densities are lowered due to the field. We follow a simple Clausius-Clapeyron type approach to analyse our data and find qualitative agreement.

6.2 Experiment

In this study we make use of the same dispersion of sterically stabilised colloidal gibbsite platelets [22,45,50] as in Chapter 4. We therefore refer to Section 4.3.1 for the experimental details of the preparation and characterisation.

The suspension’s I-N phase boundaries (at zero field) are $\phi_I = 0.238 \pm 0.002$ and $\phi_N = 0.255 \pm 0.002$. We prepared one sample within the I-N biphasic regime, at $\phi = 0.246$. (Volume fractions were calculated from the mass concentration, determined by drying a known amount of dispersion at 85°C to constant weight, and the previously measured

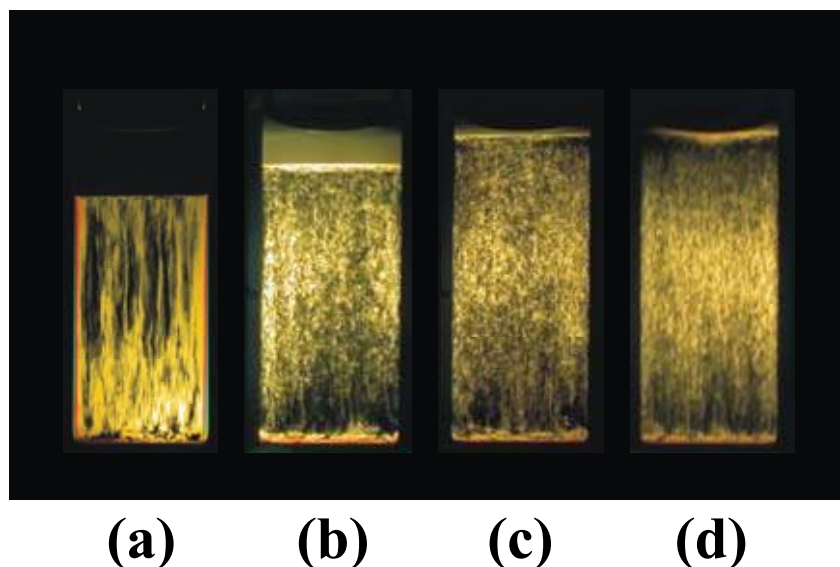


Figure 6.2 – A biphasic sample of a different batch of sterically stabilised colloidal gibbsite platelets photographed between crossed polarisers at increasing magnetic field strength. The amount of nematic phase increases with the field, at the cost of the isotropic (or paranematic) phase. The sample is shown at $B^2 =$ (a) 0, (b) 1, (c) 2, and (d) 3 T², respectively. (See colour version at page 135.)

Chapter 6

particle mass density $\rho_p = 1.7$ g/ml.) The sample was put in a spectrophotometric cell with a thickness of 2 mm.

We studied the phase behaviour of the suspension in a magnetic field using a Bruker BE25v Electromagnet. This magnet, in combination with the specific magnet poles, produces a very homogeneous magnetic field in our sample, up to field strengths of 2.3 T. The field strength was monitored using a LakeShore 421 Gaussmeter.

Before each measurement, we thoroughly homogenised the sample and suspended it between the poles of the electromagnet. Then, immediately, the magnet was brought at the intended field strength. The sample was left to phase separate in the field, which usually took 1 or 2 days. Using crossed polarisers and a cathetometer, we determined the relative amounts of isotropic and nematic phase. This procedure was executed for three field strengths and two sample volume fractions, where we kept track of the actual volume fraction by weighing the sample after dilution.

6.3 Results and discussion

We have determined the relative amounts of isotropic and nematic phase at eight state

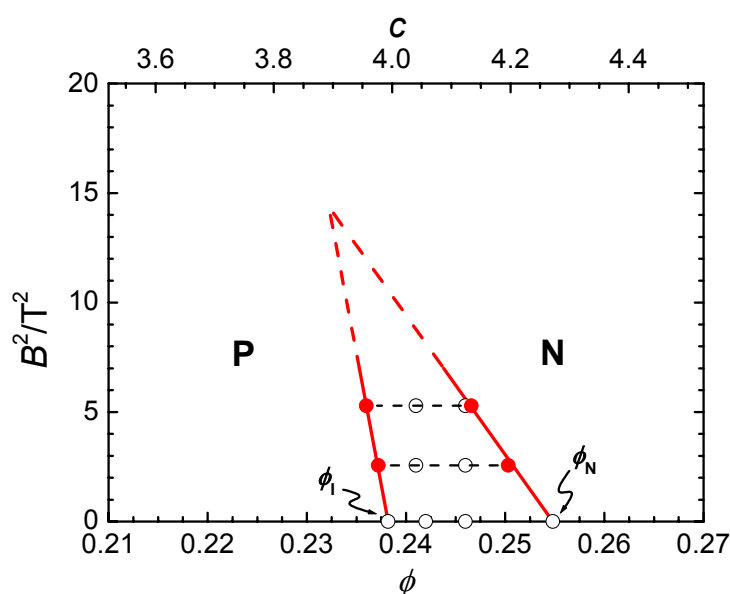


Figure 6.3 – Phase diagram of the gibbsite platelets in a magnetic field. The volume fraction is denoted by ϕ ; $c = \rho D^3$ is calculated from ϕ using $c = \phi \frac{4}{\pi} \frac{D}{L}$. The open dots indicate the state points at which we have measured the amount of isotropic and nematic phase. The solid dots indicate the limits of the biphasic gap (binodal points) that were extrapolated from the open dots using the lever rule. The solid lines indicate linear fits through the binodal points. Clearly, the isotropic-nematic phase transition shifts to lower volume fractions with increasing field strength. P denotes the paranematic and N the nematic phase.

Table 6.1 – Measured slopes of the paranematic and nematic binodal lines. The negative slope indicates that the phase transition densities shift to lower values with increasing field strength.

binodal	$dB^2/dc/T^2$
paranematic	-160
nematic	-38

points in the I-N biphasic regime, by variation of volume fraction and magnetic field. We observe an increase of the relative amount of nematic phase with increasing magnetic field, as illustrated in Fig. 6.2. To our knowledge, this is the first observation of this kind ever.

Two pairs of state points (at a certain field strength) were used to obtain the edges of the biphasic region, the so-called limits of stability or “binodal” volume fractions, by extrapolation using the lever rule. Doing this, we implicitly neglect fractionation effects. It has been observed, however, that fractionation in this kind of dispersions is not very strong [22,67]. The procedure yields a phase diagram as depicted in Fig. 6.3. We connect the binodal points of each branch – in a first approximation – by straight lines. Clearly, the phase transition densities shift to lower values with increasing field. The slopes of the binodal lines are given in Table 6.1. They suggest the existence of a tricritical point around $B^2 \approx 15 T^2$, in accordance with Fig. 6.1b.

We now analyse our observations with a Clausius-Clapeyron type approach. Suppose an isotropic phase is in equilibrium with a nematic phase at zero field. Such a system is described by the equilibrium condition

$$\mu_I(\Pi_0) = \mu_N(\Pi_0), \quad (6.2)$$

where Π_0 is the osmotic pressure of the system in zero field. On applying a magnetic field, the chemical potential will shift to a different value, at a different pressure, $\Pi_0 + \Delta\Pi$,

$$\mu_I(\Pi_0 + \Delta\Pi, B) = \mu_N(\Pi_0 + \Delta\Pi, B). \quad (6.3)$$

Taylor expansion around $\Pi = \Pi_0$ and $B = 0$ yields

$$\mu_I(\Pi_0) + \left(\frac{\partial \mu_I}{\partial \Pi} \right)_{T,B=0} \Delta\Pi + \Delta\mu_I(\Pi_0, B) = \mu_N(\Pi_0) + \left(\frac{\partial \mu_N}{\partial \Pi} \right)_{T,B=0} \Delta\Pi + \Delta\mu_N(\Pi_0, B), \quad (6.4)$$

which, using Eq. (6.2), leads to

Chapter 6

$$\Delta\Pi = \frac{\Delta\mu_N(\Pi_0, B) - \Delta\mu_I(\Pi_0, B)}{\left(\frac{\partial\mu_I}{\partial\Pi}\right)_{T, B=0} - \left(\frac{\partial\mu_N}{\partial\Pi}\right)_{T, B=0}}. \quad (6.5)$$

This has the typical Clausius-Clapeyron form: a change in the equilibrium pressure depends on the change in chemical potential. From thermodynamics, it follows that

$$\left(\frac{\partial\mu_I}{\partial\Pi}\right)_{T, B=0} = \frac{1}{\rho_I} \quad \text{and} \quad \left(\frac{\partial\mu_N}{\partial\Pi}\right)_{T, B=0} = \frac{1}{\rho_N}, \quad (6.6)$$

where ρ denotes the number density at zero field. In addition,

$$\begin{aligned} \Delta\mu_I(\Pi_0, B) &= \langle w_{mag}(\theta) \rangle_I = 0 \\ \Delta\mu_N(\Pi_0, B) &= \langle w_{mag}(\theta) \rangle_N = -\frac{1}{3}\Delta\chi B^2 S_2^B \end{aligned} \quad (6.7)$$

Here, S_2^B is the order parameter along the z -axis (and the magnetic field) that is related to S_2 , the order parameter measured along the director of the nematic phase, by

$$S_2^B = -\frac{1}{2}S_2. \quad (6.8)$$

(This is the equivalent of a frame-of-reference change sometimes used in the field of NMR and quantum mechanics.) Substitution of Eqs. (6.6) - (6.8) in Eq. (6.5) yields

$$\Delta\Pi = \frac{\frac{1}{6}\Delta\chi B^2 S_2}{\frac{1}{\rho_I} - \frac{1}{\rho_N}}. \quad (6.9)$$

We now wish to relate this exact result to the change in the coexistence densities of the phases by

$$\Delta\rho_\alpha = \frac{1}{\left(\frac{\partial\Pi}{\partial\rho}\right)_\alpha} \frac{\frac{1}{6}\Delta\chi B^2 S_2}{\frac{1}{\rho_I} - \frac{1}{\rho_N}}, \quad (6.10)$$

where α denotes either of the phases. Rewriting yields

$$\frac{\Delta c_\alpha}{B^2} = \frac{1}{\left(\frac{\partial \tilde{\Pi}}{\partial c}\right)_\alpha} \frac{\frac{1}{6} \frac{\Delta \chi}{kT} S_2}{\left(\frac{1}{c_I} - \frac{1}{c_N}\right)} \quad (6.11)$$

where we have introduced dimensionless quantities $\tilde{\Pi} = \Pi D^3 / kT$ and $c = \rho D^3 = \phi \frac{4}{\pi} \frac{D}{L}$ with D and L the average platelet diameter and thickness, respectively. In the value of $\Delta c_\alpha / B^2$ we recognise the inverse slope of the binodal lines in a phase diagram where B^2 is plotted against c . $\left(\frac{\partial \tilde{\Pi}}{\partial c}\right)_\alpha$ is recognised as the compressibility of phase α , and, apparently, the slopes of the paranematic and nematic binodal differ due to a different compressibility of the phases at coexistence.

Let us now turn to an analysis of our experimental results. In order to compare the slopes of the binodals found in our experiment with the theoretical predictions of Eq. (6.11), we need to know the compressibilities of both phases at equilibrium. The compressibility of the paranematic phase (in a magnetic field) is – to fourth order in B – equal to that of the isotropic phase, and, hence, can be obtained from computer simulations of hard disks. However, for the compressibility of the nematic phase one has to take the compressibility *along* the binodal, which is not available.

In addition to the compressibilities, the diamagnetic susceptibility anisotropy $\Delta \chi$ and nematic order parameter S_2 are needed. As discussed in the previous chapter (Section 5.4) we take $\Delta \chi = -1 \times 10^{-22} \text{ J/T}^2$.

In Table 6.2 we present calculated slopes for three values of S_2 and three values for the compressibility of the isotropic phase, obtained from computer simulations of cut spheres [44,150] (see also Chapter 3) with aspect ratios close to our experimental one, $(L/D)_{exp} \approx 1/13$. Clearly, the experimental slope is only well described when a relatively

Table 6.2 – Slopes dB^2/dc of the paranematic binodal, calculated with our Clausius-Clapeyron equation (Eq. (6.11)) for a range of aspect ratios L/D and order parameters S_2 in the nematic phase. As discussed in the previous chapter, we take $\Delta \chi = -1 \times 10^{-22} \text{ J/T}^2$.

L/D	$\left(\frac{\partial \tilde{\Pi}}{\partial c}\right)_I$	$dB^2/dc / \text{T}^2$		
		$S_2 = 0.4$	$S_2 = 0.6$	$S_2 = 0.8$
1/20	6.4 [44]	-67	-44	-33
1/15	9.9 [150]	-103	-69	-52
1/10	15.0 [44]	-156	-104	-78

Chapter 6

low order parameter is used. Discrepancies might be due to the fact that the computer simulations employ monodisperse particles, while we deal here with a rather polydisperse experimental system. Furthermore, our experimental data are rather limited and more measurements, especially near the critical point, are required to draw quantitative conclusions. Nevertheless, we show that a relatively simple Clausius-Clapeyron type approach is able to give a reasonable estimate of the slope of the isotropic branch of the binodal.

6.4 Conclusion

We have studied the influence of a magnetic field on the isotropic-nematic phase behaviour of a suspension of sterically stabilised colloidal gibbsite platelets. We have found that the phase transition densities are driven to lower values in a magnetic field. Our observations suggest that the isotropic and nematic binodal lines meet in a critical point, in accordance with theoretical predictions that have been done before. We analyse our data with a simple Clausius-Clapeyron type approach. Despite its simplicity, it allows one to estimate the slope of the isotropic branch of the binodal. We furthermore note that future measurements are required to draw more quantitative conclusions from our experiment.

The Frederiks transition in a nematic phase of colloidal gibbsite platelets

Abstract

In this chapter, the effect of a magnetic field on the nematic phase of sterically stabilised gibbsite platelets is studied. It is found that a thin layer of this nematic phase shows a strong tendency to homeotropic anchoring on a wall. This condition enables us to induce the Frederiks transition reproducibly. The uniform Frederiks transition allowed for determination of the bend elastic constant $K_3 = 2 \pm 1 \times 10^{-13}$ N, which appears to be close to that of rod-like colloidal *fd* virus particles. To our knowledge, this is the first reported measurement of an elastic constant of a nematic phase of hard disks. We furthermore present exploratory measurements of a “non-uniform” bend-splay Frederiks transition, showing typical transient periodic patterns. We measure the periodicity of the patterns as a function of sample thickness and magnetic field strength and find qualitative agreement with theoretical predictions.

7.1 Introduction

In the current chapter, which concludes Part II, we will study the nematic phase in a magnetic field, specifically the field-induced distortion of a thin nematic layer contained between two walls, known as the Frederiks transition [119].

Chapter 7

The origin of the Frederiks transition is the competition between the wall-imposed director orientation of the nematic phase, and a magnetic field opposing this orientation. Usually, a magnetic field is applied to a uniformly aligned nematic phase in such a way that the director tends to realign perpendicular to its initial direction. The final director field is that for which the magnetic field torque is balanced by the elastic restoring torque transmitted through the layer from the anchored boundaries and this depends on the values of the so-called Franck elastic constants K_i of the nematic phase. The three elastic constants K_1 , K_2 , and K_3 pertain to the three basic types of deformation in a nematic phase, *i.e.*, the splay, twist, and bend deformation, respectively. Earlier experiments employing colloidal suspensions showing the Frederiks transition include rod-like tobacco mosaic virus [151], *fd* virus [140,152,153], and goethite [106] particles.

It can be shown that the free energy density F_d of a deformed nematic phase is given by [119]

$$F_d = \frac{1}{2} K_1 (\vec{\nabla} \cdot \vec{n})^2 + \frac{1}{2} K_2 (\vec{n} \cdot (\vec{\nabla} \times \vec{n}))^2 + \frac{1}{2} K_3 (\vec{n} \times (\vec{\nabla} \times \vec{n}))^2, \quad (7.1)$$

where \vec{n} , actually $\vec{n}(\vec{r})$, is a unit vector indicating the director field. From Eq. (4.4) it follows that the magnetic energy density F_m is given by

$$F_m = -\frac{1}{2} \rho \Delta \chi (\vec{n} \cdot \vec{B})^2, \quad (7.2)$$

where $\Delta \chi$ denotes the diamagnetic susceptibility per particle and ρ the number density of the particles in the nematic phase. Minimising the total free energy $F = F_d + F_m$ will yield the equilibrium director field. At very low field strengths, the magnetic energy will simply be too low to overcome the elastic forces in the nematic phase. At a certain threshold-value of the field B_c , the director field will start to deviate from the initial state. It can be shown that B_c is given by

$$B_c = \frac{\pi}{d} \sqrt{\frac{K_i}{\rho |\Delta \chi|}} \quad (i=1,2,3), \quad (7.3)$$

where d denotes the thickness of the nematic layer and K_i the elastic constant of the deformation being applied. Eq. (7.3) is valid for a strongly anchored nematic phase, *i.e.*, in which the director right at the wall is not disturbed by the magnetic field. In our experiments, this appears to be the case.

If the distorting field is chosen only slightly larger than B_c , the Frederiks transition induced will be uniform or homogeneous, *i.e.*, the director field will only smoothly vary in space

and time. At still higher fields, a non-uniform transition may be induced, involving a spatially periodic, transient instability in which adjacent domains of the sample rotate in opposite directions. Although such periodic structures do not have the lowest free energy, they are preferred from a dynamical point of view because they show a reduced effective viscosity due to backflow coupling. (This case has to be distinguished from the non-uniform equilibrium periodic structure in the splay Frederiks transition that has been observed for $K_1/K_2 > 3.3$ and which follows from free energy calculations [154].) Thus, the non-uniform response to the external magnetic field is faster than the uniform Frederiks transition. As soon as a field of high enough strength is switched on, the sample is in unstable equilibrium, and small fluctuations of the director field grow exponentially in the presence of the destabilising field. Because of non-linearities, the mode with the fastest growth rate suppresses all slower modes and is finally observed macroscopically. The theoretical description of this mode selection mechanism was provided by Guyon and co-workers [155]. The relation between the magnetic field strength, sample thickness and wavelength of the fastest growing mode λ follows from their theory and is given by [156,157]

$$\left(\frac{B}{B_c}\right)^2 = P\left(\frac{2d}{\lambda}\right)^4 + Q\left(\frac{2d}{\lambda}\right)^2 + R, \quad (7.4)$$

where the coefficients P , Q and R are functions of the viscosities and elastic constants. Apparently, for larger fields the wavelength decreases, which makes sense, because, as the magnetic field strength increases it supplies more energy to allow for larger gradients. From Eq. (7.4) it follows that for fields exceeding a second threshold field

$$B_s = B_c \sqrt{R} \quad (7.5)$$

the non-uniform Frederiks transition will occur whose wavelength decreases with increasing magnetic field strength.

Summarising, no Frederiks transition will occur for $B < B_c$. For a magnetic field strength $B_c < B < B_s$ the uniform transition will occur, and for $B > B_s$ the non-uniform Frederiks transition. One should take note of the fact that the periodic structures, created in the non-uniform Frederiks transition, are transient phenomena. When subjected to the reorienting field for long enough time, the stripes will disappear and the nematic phase will reach a new equilibrium.

In this study, we aim to determine the threshold value of the uniform Frederiks transition, which allows us to obtain the bend elastic constant K_3 . A prerequisite for an accurate determination of B_c is a well-defined initial configuration of the director field, *e.g.*, homeotropic alignment [119]. This is a configuration of the nematic phase with the director

Chapter 7

field perpendicular to the sample wall. It will be shown that our samples acquire such orientation relatively easily, facilitating our experiments.

We will furthermore study the non-uniform bend-splay Frederiks transition in samples of the same nematic phase and determine the wavelength of the transient striped patterns as a function of field strength and sample thickness. A similar study was performed by Kuzma [158], who studied samples of disk-like micelles with negative diamagnetic susceptibility anisotropy in a rotating magnetic field, also probing the bend elastic constant. In a subsequent comment [159], Fraden and Meyer observed an analogy between rod- and plate-like particles by noting that “*the splay geometry for the rod system is both formally and physically equivalent to the bend geometry for the disk system, and the appearance of stripes for disks in the bend geometry is expected*”. Although our preliminary results do not allow for a quantitative analysis, they can be fitted with the theoretical expression (Eq. (7.4)) reasonably well.

7.2 Experiment

7.2.1 Preparation and characterisation

In this study we make use of sterically stabilised colloidal gibbsite platelets in toluene, synthesised according to the procedures in the literature [22,45,50]. We use the batch that has been used in Chapter 4 and purified as explained in Chapter 5; see Sections 4.3.1 and 5.3.1 for details.

7.2.2 Samples

In order to obtain a nematic phase of the platelet dispersion, we brought a sample of the stock dispersion in the I-N biphasic gap. After 1 day, the sample had phase separated, yielding about 90% isotropic phase and 10% nematic phase. Both phases were extracted. The isotropic fraction was used to study the magnetic-field-induced birefringence, as described in Chapter 5 of this thesis. The nematic phase was used to study the Frederiks transition. The volume fraction of the nematic phase was determined to be $\phi_N = 0.27$, which corresponds to a number density of $\rho = 4.1 \times 10^{20} \text{ m}^{-3}$.

As stated in the introduction, we need samples with a well-defined initial alignment to conduct our experiments. Therefore, we filled flat optical capillaries with the nematic phase. These capillaries (obtained from VitroCom, USA) have a thickness d ranging from 20 to 300 μm , a width $10d$ and a length of about 70 mm. Each sample was prepared by sucking the nematic phase into the capillary using a vacuum pump. The capillaries were subsequently flame-sealed to avoid evaporation of the solvent. Due to the filling, the samples showed streaming birefringence and defects like the ones shown in Fig. 7.1. These disappeared over several days after which the samples became completely homeotropic, indicative of strong anchoring. Exceptions are the $d = 200$ and 300 μm -samples that did not

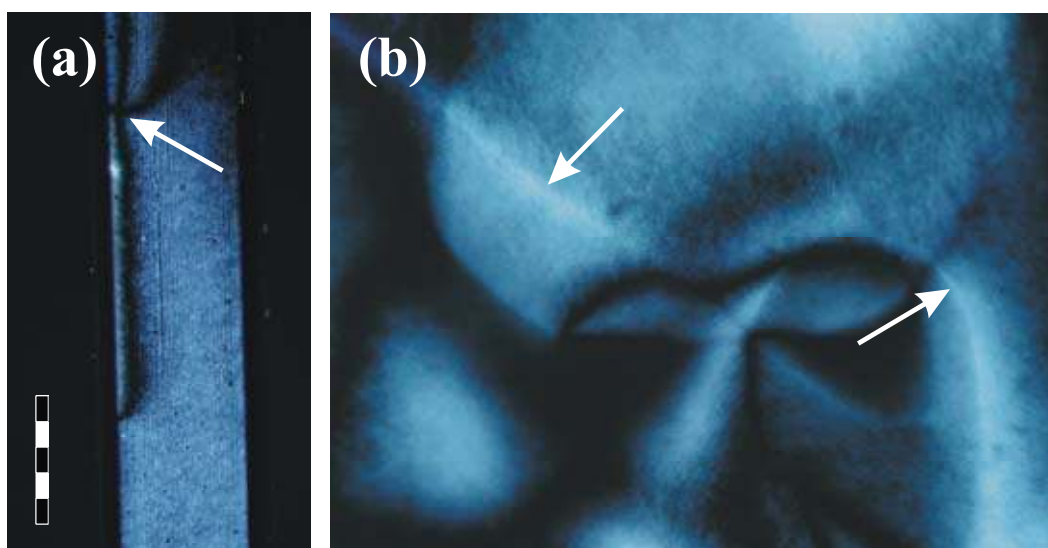


Figure 7.1 – The nematic phase of sterically stabilised colloidal gibbsite platelets shows defects typical for a nematic phase, like the (a) four-brush defect and (b) disclination lines indicated by the white arrows. The scale bar denotes 500 μm and pertains to both micrographs. (See colour version at page 136.)

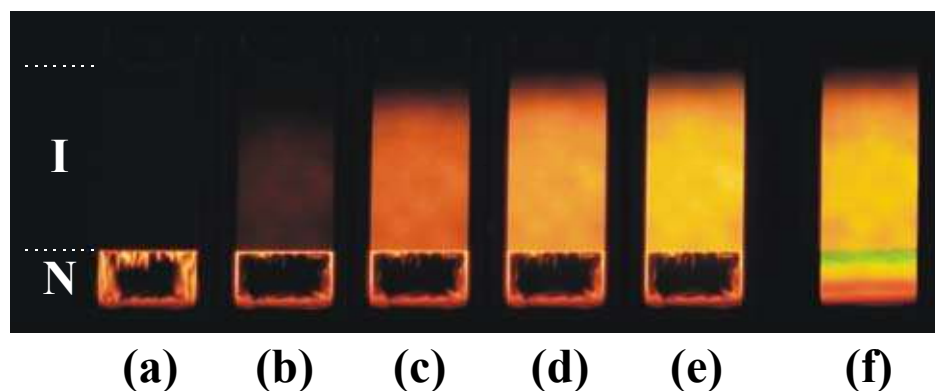


Figure 7.2 – An isotropic-nematic sample of the sterically stabilised colloidal platelets at coexistence between crossed polarisers (that make angles of -45° and 45° with the vertical direction). This demonstrates the wall-imposed director field in the nematic phase and the Frederiks transition. (a) - (e) have been shown earlier in Fig. 5.1 and depict the sample at increasing field strength of 0 to 2.0 T. (f) depicts the sample after rotating it in the horizontal magnetic field of 2.0 T, inducing a reorientation of the nematic director field, *i.e.*, the Frederiks transition. In (a) - (e), the nematic phase contains a black region, seemingly indicating lack of orientational order. However, due to the imposed director orientation by the walls, the sample has become homeotropic in the centre. Clearly, the director field is dominated by the wall that is closest, as indicated by the birefringence at the sides of the phase. At increasing magnetic field, the black patch extends as the horizontal magnetic field stabilises homeotropic alignment. (See colour version at page 136.)

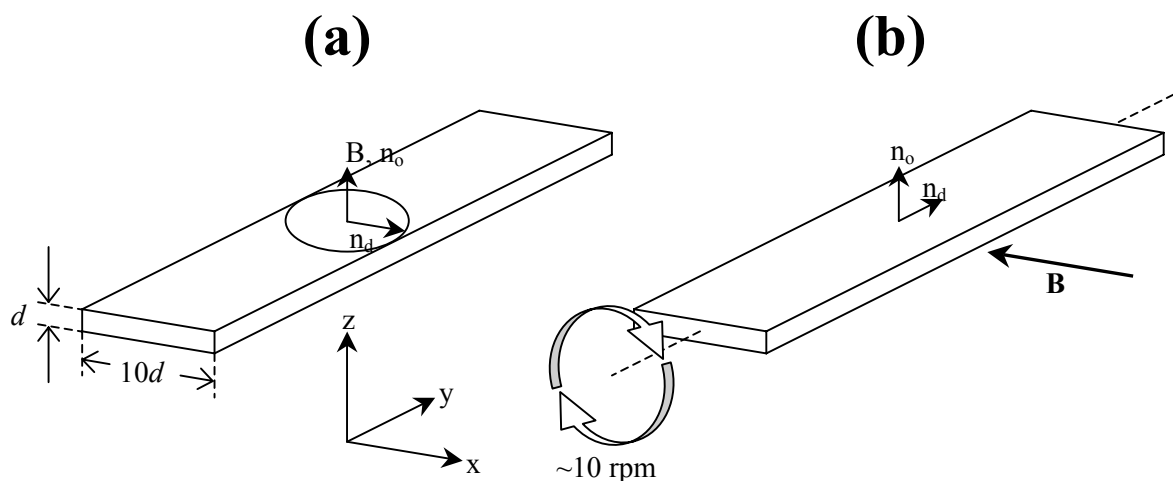


Figure 7.3 – Sketch of the geometry of the two types of experiments performed in this study. In experiment A, the magnetic field is applied perpendicular to the sample wall, inducing a uniform Frederiks transition, while in experiment B, a non-uniform transition is induced by rotating the sample around its long axis. From the geometry of the setup, it is found that we probe the bend elastic constant K_3 in both experiments [119].

become homeotropic. In addition, it was not possible to avoid flow in these relatively thick samples. Hence, they were not used in this study.

The preferential orientation of the platelets with their planes along the wall is understood as due to the anisotropic shape of the particles. This notion has been discussed in Chapter 2, where we enhanced the depletion attraction between platelets and the wall using non-adsorbing polymer. As an example, we show Fig. 7.2 (repeating Fig. 5.1) here, because it demonstrates the influence of a wall on the nematic phase (apart from the magnetic-field-induced alignment of the platelets in the isotropic phase, as discussed in Chapter 5).

7.2.3 Methods

In this study, two types of experiments have been performed, both probing the bend elastic constant K_3 of the nematic phase, as inferred from the geometry of the experiment [119]. In the first type, henceforth referred to as A, we applied a magnetic field perpendicular to the sample wall as sketched in Fig. 7.3, driving a uniform Frederiks transition. We have measured the critical field strength B_c for the onset of the uniform Frederiks transition. Before each measurement, we checked that the sample was completely homeotropic. A magnetic field was applied for a maximum of 1 h, after which the sample was inspected using a polarisation microscope to detect birefringence anywhere in the sample as an indication of the onset of the Frederiks transition. The field strength was increased and the sequence was repeated until the sample had become completely birefringent. We repeated this procedure for the range of sample thicknesses, at fields from 5 mT up to 0.5 T.

The second type of experiments, B, involved rotating the sample in the magnetic field, thereby driving a non-uniform transition that yields a very typical, transient periodic stripe pattern; see Fig. 7.3. Beforehand, we checked the samples to be completely homeotropic. Each measurement was conducted by rotating a sample around the capillary's long axis in a magnetic field at an angular speed of about 10 revolutions per minute ($\cong 0.17$ Hz) for about 10 to 20 minutes. We inspected the sample at regular intervals during the rotation. This experiment was performed at magnetic field strengths from 0.2 to 0.8 T.

7.3 Results and discussion

7.3.1 The uniform Frederiks transition

The uniform Frederiks transition threshold B_c was determined in experiment A. Fig. 7.4 shows the onset of the transition in a sample with a thickness of $50 \mu\text{m}$. Typically, the first signs of birefringence were found at the edges of the capillary. Table 7.1 lists the

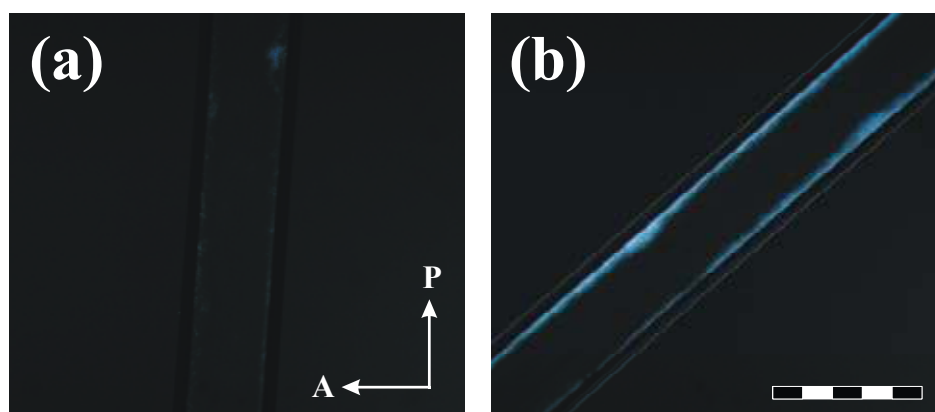


Figure 7.4 – The onset of the uniform Frederiks transition, in a sample with $d = 50 \mu\text{m}$ at $B = 91$ mT. The sample is shown at (a) 0° and (b) 45° with respect to the polariser-orientation, as is indicated by the arrows; the scale bar denotes 1 mm. The first signs of birefringence are visible at the edges of the capillary, where they aid the reorientation. (See colour version at page 137.)

Table 7.1 – Uniform Frederiks transition threshold-value B_c as a function of sample thickness. The values are plotted in Fig. 7.5.

$d/\mu\text{m}$	B_c/T	$B_c \cdot d / 10^{-6} \text{ Tm}$
20	0.40 ± 0.05	8 ± 1
40	0.19 ± 0.02	7.6 ± 0.8
50	0.08 ± 0.02	4 ± 1
100	0.03 ± 0.03	3 ± 3

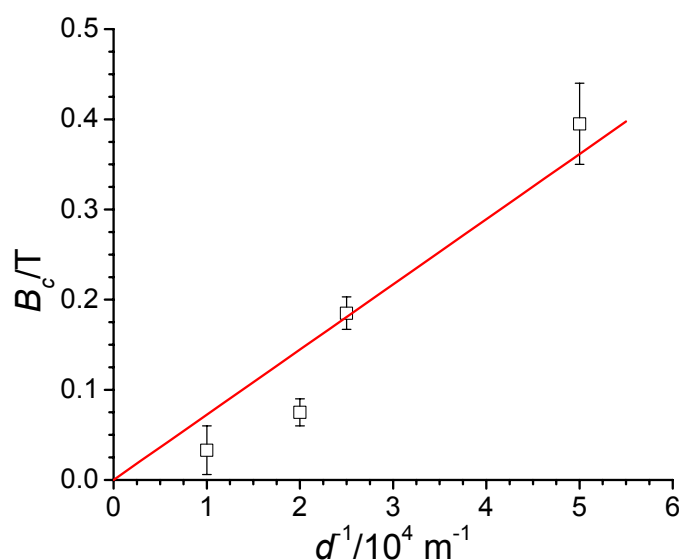


Figure 7.5 – The threshold field of the uniform Frederiks transition as a function of reciprocal sample thickness. The linear fit through the origin yields $B_c \cdot d = 7 \pm 2 \mu\text{Tm}$.

determined critical field at all thicknesses. It appeared difficult to precisely determine the critical field B_c for the 50 and 100 μm samples, which explains the rather large error bars on those values. The table also lists the values of $B_c \cdot d$, which, in the case of strong anchoring, see Eq. (7.3), should yield a constant value. In Fig. 7.5 we plot B_c vs. $1/d$; the slope of the linear fit yields $B_c \cdot d = 7 \pm 2 \mu\text{Tm}$. This value allows for a calculation of the bend elastic constant K_3 . For the diamagnetic susceptibility anisotropy $\Delta\chi$, we take $\Delta\chi \cong 1 \times 10^{-22} \text{ J/T}^2$ as obtained in Chapter 5. Using Eq. (7.3), we obtain $K_3 = 2 \pm 1 \times 10^{-13} \text{ N}$. To our knowledge, this is the first measurement of one of the elastic constants of a nematic phase of hard disks. Unfortunately, there is no model available that predicts the elastic constants of hard disks. A comparison with the elastic constants of colloidal rods, however, is possible. The cholesteric phase of rod-like *fd* virus particles (at coexistence) has a twist elastic constant of $K_2 \cong 4 \times 10^{-13} \text{ N}$ [140,152,153], which is of the same order of magnitude as our platelet suspension. For rods, there are models that predict the elastic constants [160-162] and, from these, it follows that $K \approx 10kT/D$ as a crude estimate, with D the diameter of the rod. If we suppose this relation holds for plate-like particles as well, we obtain $K \approx 2 \times 10^{-13} \text{ N}$, in good agreement with our experiment.

7.3.2 The non-uniform Frederiks transition

In experiment B, a non-uniform Frederiks transition was induced, involving typical transient periodic structures [154,163]; see Fig. 7.6. At high magnetic field, the pattern appeared as early as after one revolution of the sample in the field. The wavelength of the

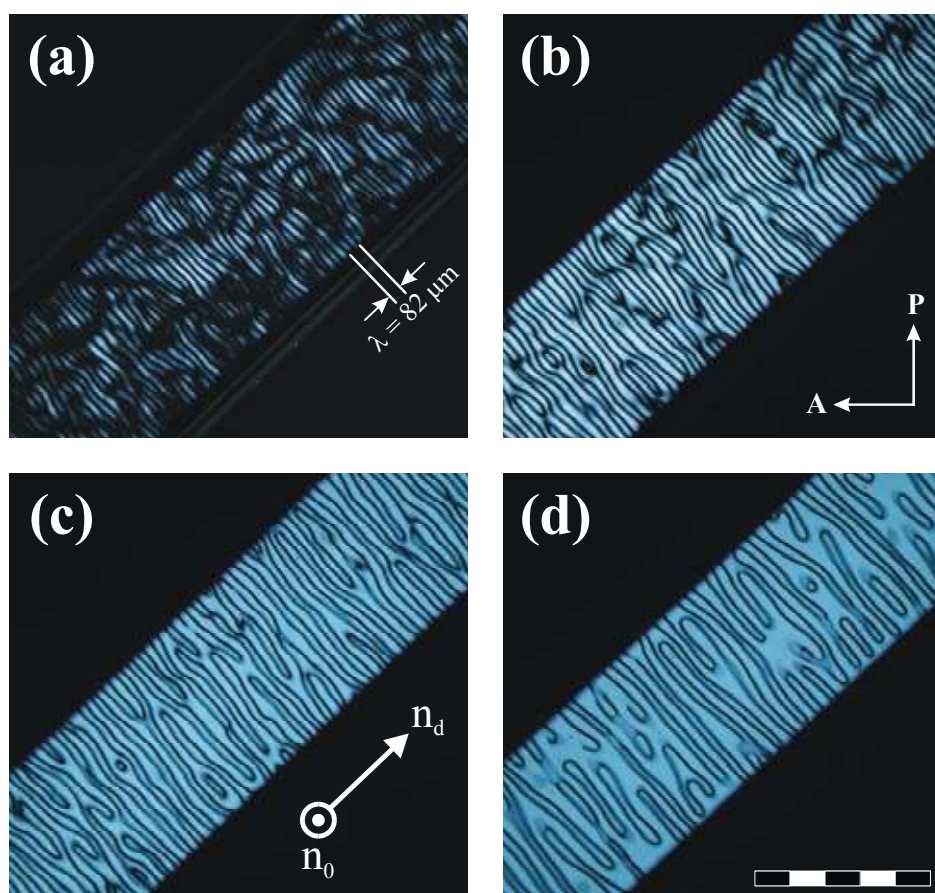


Figure 7.6 – Evolution of the non-uniform Frederiks transition in a sample with thickness $d = 100 \mu\text{m}$ at $B = 0.56 \text{ T}$, rotated around the capillary's long axis at 0.17 Hz , observed at (a) $t = 5 \text{ s}$, (b) 86 s , (c) 200 s , and (d) 554 s . The sample makes an angle of 45° with the polarisers; the scale bar denotes 1 mm . The wavelength of the periodic pattern increases from $82 \mu\text{m}$ at the start to a saturation value of $104 \mu\text{m}$. The evolution of the wavelength in time is depicted in Fig. 7.7. (See colour version at page 137.)

Table 7.2 – The wavelength λ of the transient periodic pattern as a function of field strength B and sample thickness d .

$d/\mu\text{m}$	B/T			
	0.22	0.39	0.56	0.79
20	–	–	–	160
30	–	–	120	68
40	–	–	200	180
100	280	250	82	70

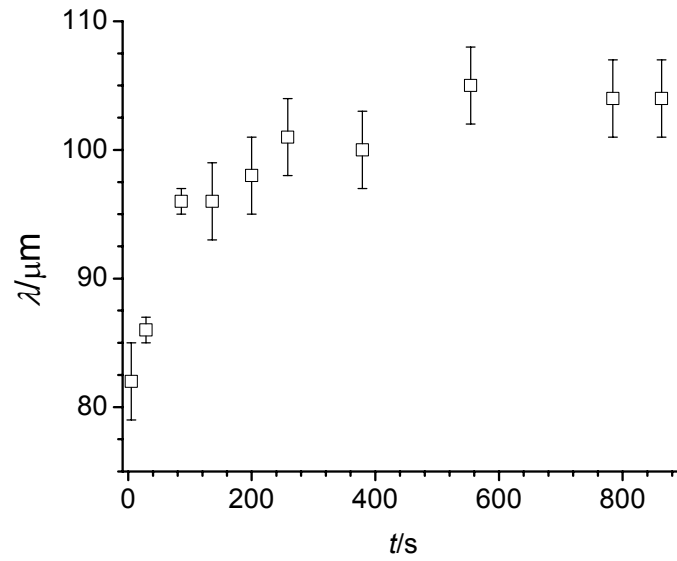


Figure 7.7 – Evolution of the wavelength λ of the periodic pattern of the non-uniform Frederiks transition. These data relate to the same sample as shown in Fig. 7.6, we refer to the caption of that figure for sample details.

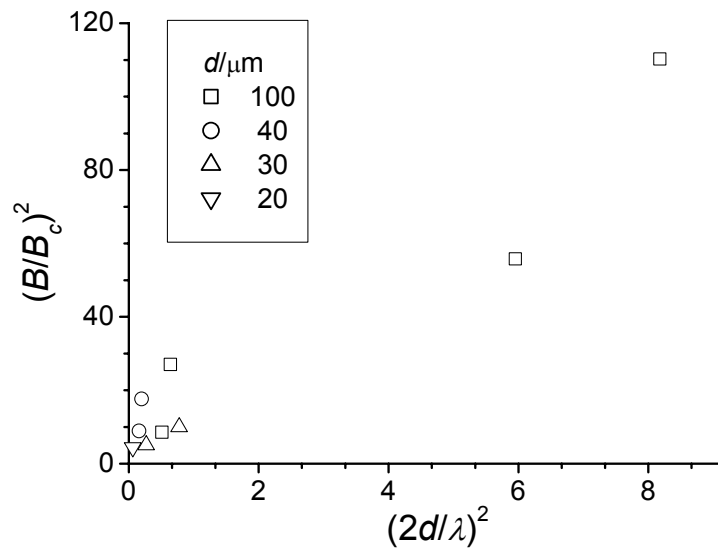


Figure 7.8 – Scaled magnetic field strength vs. scaled stripe pattern wavelength. Our results follow the predicted behaviour qualitatively, see Eq. (7.4).



Figure 7.9 – Early stage of the rotation of a nematic phase in a horizontal magnetic field, used in Chapter 5 to determine Δn_{sat} . Sample thickness $d = 2.00$ mm, $B = 1.4$ T, the scale bar denotes 1 cm. The temporal periodicity observed in this sample hints at the same type of transient pattern as observed in the much thinner samples in this study. However, the initial alignment of this sample was not homeotropic, hence, we do not draw quantitative conclusions from this observation. (See colour version at page 138.)

pattern increased in time, in agreement with theory [164], and appeared to reach a saturation value. This is plotted for one sample in Fig. 7.7. For the complete range of samples, we have measured the initial wavelengths, *i.e.*, right after the pattern became visible, and list them in Table 7.2. Inspired by the relation given in Eq. (7.4), we plot these data as $(B/B_c)^2$ vs. $(d/\lambda)^2$ in Fig. 7.8. In view of the relatively large scatter of the data points, we are reluctant to perform a quadratic fit (as suggested by the theory) and suffice to note that our results follow the predicted behaviour qualitatively. A more accurate description calls for more measurements, as well as detailed information on the viscoelastic parameters of the studied nematic phase; information that is not yet available.

The Frederiks transition has in fact been used earlier in this thesis. In Chapter 5, we used the technique of rotating a nematic phase in a magnetic field to produce a well-aligned uniaxial nematic phase in order to determine the saturation value of the birefringence, Δn_{sat} . Then, a sample with thickness $d = 2.00$ mm was rotated in a magnetic field of 1.4 T for several minutes, see Fig. 5.6. In Fig. 7.9 we depict the sample at an early stage in the procedure. There seems to be a spatial periodicity in this sample, suggesting a non-uniform Frederiks transition. However, this could equally well be due to the inhomogeneous initial state of the nematic phase.

7.4 Conclusion

We have studied the nematic phase of sterically stabilised colloidal gibbsite platelets. The strong homeotropic anchoring on the wall facilitates a study of the Frederiks transition in this nematic phase. It allows for the first experimental determination of the bend elastic constant in a nematic phase of hard disks. In previous studies, it was found that the elastic constants of hard rods scale as $K \approx 10kT/D$, with D the diameter of the rod. Assuming that this relation holds for platelets as well, we find excellent agreement with our experimental value. The non-uniform Frederiks transition that was induced in our nematic

Chapter 7

phases of colloidal platelets yields very typical transient stripe patterns that have been observed before in other nematogens. The predicted behaviour of the periodicity with field strength and sample thickness was confirmed by our measurements, although a quantitative analysis was not possible. In conclusion, our experimental results call for a thorough theoretical approach to the Frederiks transition in nematic phase of hard disks.

Part III

**Liquid crystal phases in a suspension of
charged colloidal gibbsite platelets
and the influence of
a gravitational and centrifugal field**

8

Liquid crystal phases in a suspension of charged colloidal platelets

Abstract

We study aqueous dispersions of charged colloidal gibbsite ($\text{Al}(\text{OH})_3$) platelets that show the isotropic (I) to nematic (N) phase transition. This is the first case where the I-N transition in a dispersion of charged colloidal platelets is not impeded by gelation since Langmuir's classic work on dispersions of clay particles more than sixty years ago (I. Langmuir, J. Chem. Phys. **6**, 873 (1938)).

By variation of the ionic strength, we are able to tune the effective thickness-to-diameter ratio of the platelets in suspension, allowing us to observe the isotropic to columnar (C) phase transition in the same suspension as well. This scenario, *i.e.*, both the I-N and the I-C transition in one suspension, has been predicted by computer simulations of hard platelets a decade ago (J. A. C. Veerman and D. Frenkel, Phys. Rev. A **45**, 5632 (1992)) and is hereby confirmed experimentally.

In addition to the shape-dependent thermodynamic driving force, the effect of gravity is important. For example, a biphasic (I-N) suspension becomes triphasic (I-N-C) on prolonged standing, which is described by a simple osmotic compression model.

8.1 Introduction

In the preceding chapters, we have studied various phenomena in a system of sterically stabilised gibbsite platelets dispersed in the organic solvent toluene. In this and the following chapter we will study the phase behaviour of suspensions of charge stabilised gibbsite platelets in water. Contrary to the relatively short-ranged steep steric repulsion between the gibbsite platelets in an organic solvent, we are now dealing with soft double-layer repulsions, the range of which can be tuned by the salt concentration. The isotropic-nematic phase transition in a system of charged colloidal platelets was reported by Irving Langmuir as early as 1938 [7]. In a remarkable paper he reported on sols of California bentonite clay particles that, after standing for several 100 hours, separated into two distinct phases. This separation was found to occur for sols containing between 2.0 and 2.2 wt% clay particles. The phase-separated system can be identified as an isotropic phase (I) in equilibrium with a nematic (N) liquid crystal phase. This observation – among others [8,9] – inspired Lars Onsager to the theoretical explanation of the I-N phase transition [10,11].

Langmuir refers to his clay as “California bentonite”. The name bentonite is nowadays generally used to indicate montmorillonite, a dioctahedral smectite clay [165]. However, Langmuir did not have a montmorillonite in hand. From the adjective he uses we know that he was using a clay from California. From the elemental analysis, provided by Langmuir, it is clear that he worked with the trioctahedral smectite clay named hectorite in 1941 after its finding place Hector (California).

Quite surprisingly, although Wyoming bentonite [166,167], Laponite [166,168,169] (a synthetic hectorite produced by Laporte Industries Ltd.), and synthetic Na-fluorhectorite [170,171] have been used quite extensively in experimental attempts to observe the I-N phase transition in clays, never again has a *natural* hectorite been used in such studies. This may be the reason that the I-N phase transition, as reported by Langmuir, has not been observed again in clay systems and that gelation is found instead.

Here, we report a study of an aqueous dispersion of charge-stabilised gibbsite platelets. We find that this suspension does show the I-N phase transition. In addition, it shows the columnar (C) liquid crystal phase. The columnar phase has been predicted by computer simulations of hard platelets [13] before. Specifically, these simulations show that hard platelets undergo either the I-N and subsequently the N-C transition or directly the I-C phase transition, depending on the diameter-to-thickness ratio. Quite recently, these two scenarios have been observed experimentally. The I-N phase transition was reported to occur in suspensions of sterically stabilised gibbsite platelets [22] and mixed-metal hydroxides ($\text{Mg}_{2-x}\text{Al}_x(\text{OH})_2^{x+}$) [27], and the N-C transition only in the former [45]. In Part 1 and 2 of this thesis, we have studied the sterically stabilised gibbsite platelets and the influence of external fields in detail. The second scenario (direct I-C phase transition) was observed in a suspension of charged nickel hydroxide ($\text{Ni}(\text{OH})_2$) platelets [46,172]. However, the scenarios have never been observed in one colloidal system.

In this chapter, we show that this can be achieved in our suspension of charge-stabilised colloidal gibbsite platelets by variation of the ionic strength. In addition, we find that gravity plays a major role in the phase behaviour of our platelet suspensions, like in the case of colloidal spheres [80,83-85,173] and rods [29,30,87,174]. Our results are described by a simple osmotic compression model that we developed.

8.2 Experiment

8.2.1 Preparation and characterization

The suspension of gibbsite platelets was synthesised following a modified version of a procedure that was developed earlier at our laboratory [22,50]. To a solution of HCl (2 litres, 0.09 M) aluminium *sec*-butoxide (0.08 M, Fluka Chemika, pract. >95%) and aluminium iso-propoxide (0.08 M, Acros Organics, 98+%) were added. It was stirred for 17 days and subsequently heated for 65 hours at 85°C in a polypropylene vessel by means of a waterbath. The resulting turbid suspension was dialysed for 12 days against demineralised water in order to get rid of excess reactants and by-products. Gibbsite content was determined to be 6.5 g/l.

It has been observed that the presence of Al_{13} -ions ($\text{Al}_{13}\text{O}_4(\text{OH})_{24}(\text{H}_2\text{O})_{12}^{7+}$) has a stabilising effect on suspensions of colloidal boehmite particles [18,23,175-177]. Furthermore, Hernandez [178] presented a systematic study of the adsorption of aluminium polycations, in particular Al_{13} , on colloidal iron and aluminium oxyhydroxides and hydroxides (*i.e.*, gibbsite particles). He used ^{27}Al NMR to study the reaction of the Al_{13}

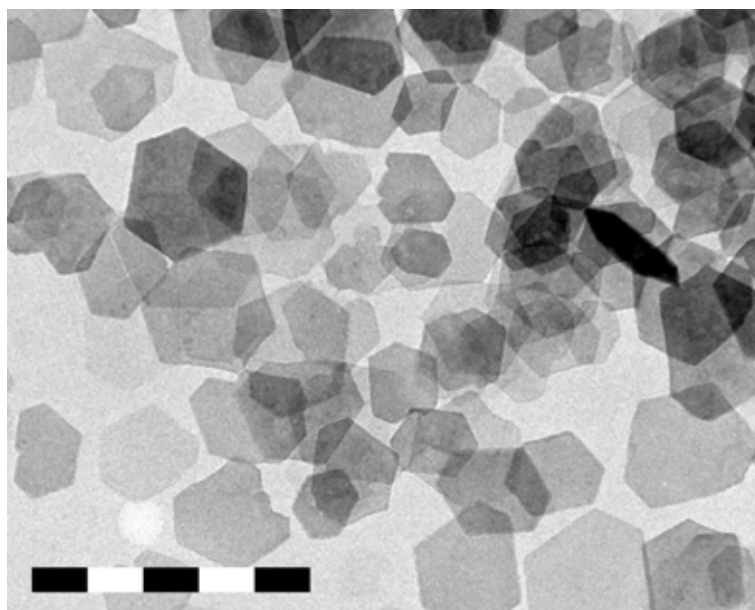


Figure 8.1 – Transmission electron micrograph of the hexagonal gibbsite platelets used in this study. The scale bar denotes 500 nm.

Chapter 8

Table 8.1 – Characteristics of the colloidal platelets used in this study, as obtained by TEM (for the diameter $\langle D \rangle$) and AFM (for the thickness $\langle L \rangle$). The given dimensions refer to the particle core; σ_D and σ_L express polydispersities.

$\langle D \rangle$	σ_D	$\langle L \rangle$	σ_L	$\langle D \rangle / \langle L \rangle$
202 nm	38 nm (19%)	13.2 nm	3.6 nm (27 %)	15.3

species with the surface of these particles. He concluded that the adsorption leads to an increased surface charge, which in turn appears to enhance the stability of the particles. In view of this, we used Al_{13} ions (as produced by hydrolysis of aluminium chlorohydrate [23], $\text{Al}_2(\text{OH})_5\text{Cl} \cdot 2-3 \text{H}_2\text{O}$) to stabilise our gibbsite platelets. To 200 ml of gibbsite dispersion (as obtained from the synthesis), 1.0 g of aluminium chlorohydrate was added. This mixture was shaken vigorously for 1.5 minute after which it was put away at room temperature for 3 days. Through a sequence of sedimentation (20 h, 1400 G) and redispersion, excess Al_{13} was removed and sodium chloride added to bring the suspensions to the intended ionic strength, either 0.1, 1, or 10 mM. Measurements showed that the conductivity was close to that of the stock NaCl solutions.

From the gibbsite dispersion, a sample was taken for investigation with transmission electron microscopy (TEM) by dipping a coated copper grid in very dilute suspension. The electron microscope was equipped with a CCD camera that was used to take micrographs. From such micrographs, as depicted in Fig. 8.1, the average particle diameter (defined as the average of the average corner-to-corner distances) was obtained using image analysis software. The anisotropic particle shape allowed us to determine the thickness of the platelets to within 0.1 nm using atomic force microscopy (AFM). Obviously, the *effective* particle dimensions in suspension depend strongly on the ionic strength; this issue will be addressed further on. The particle characteristics are listed in Table 8.1.

8.2.2 Samples and methods

To study the phase behaviour of our dispersions, weighed amounts of stock dispersion were put in spectrophotometric cells (path length 2.00 mm). The stock-particle concentration was determined by drying a known amount of dispersion at 75°C to constant weight. Variation of particle concentration in the cells was achieved by diluting with sodium chloride solution or by centrifugation, removal of supernatant and redispersion. After thorough homogenisation, the samples were stored at room temperature to reach phase equilibrium. Once phase-separated, the samples were checked for liquid crystallinity using crossed polarisers.

8.3 Results and discussion

8.3.1 Phase behaviour as determined by salt concentration

At an ionic strength of 10 mM NaCl, the suspensions are isotropic at gibbsite concentrations up to about 260 g/l. Between crossed polarisers only flow birefringence is observed. However, on increasing the particle concentration to above the mentioned value the suspensions become permanently birefringent. On a time scale of 24 h, they separate into two distinct layers divided by a sharp interface. The birefringent bottom layer appears to be a nematic phase in equilibrium with the isotropic upper phase. This isotropic phase shows very strong flow birefringence with a decay time of about 0.3 s. The nematic phase shows a threaded texture that is very typical of a nematic phase [119]. The relative amount of nematic phase increases with increasing particle concentration; see Fig. 8.2. In contrast to earlier observations [26], the samples now become fully nematic, around 410 g/l. On increasing the concentration even further, gelation is observed instead of the expected N-C phase transition. Apparently, gelation still cannot be avoided when concentrating in the usual way. However, by letting gravity work on our suspension, we have been able to induce a high particle concentration in a very gentle way. This is described in more detail in Section 8.3.2.

At somewhat lower ionic strength (1.9 and 1.4 mM), the suspensions also show the I-N phase transition. However, when going to even lower ionic strength (1 mM and below), the

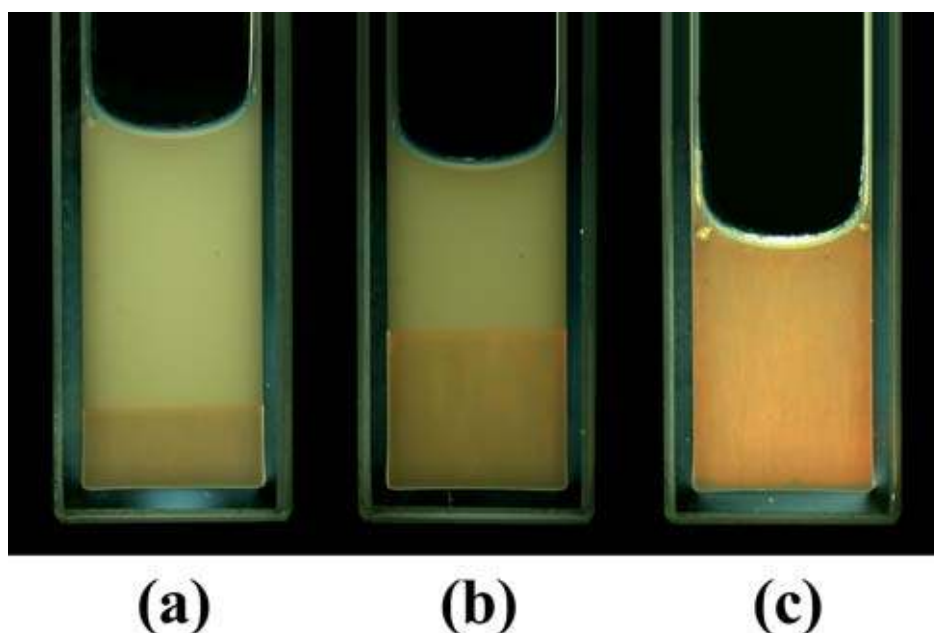


Figure 8.2 – The I-N phase transition observed between crossed polarisers. The ionic strength in these samples is 10 mM and the gibbsite concentration (a) 328 g/l, (b) 356 g/l, and (c) 464 g/l. Sample (c) is well into the nematic phase, in contrast with our earlier study [26] where gelation impeded the formation of a completely nematic phase. (See colour version at page 138.)

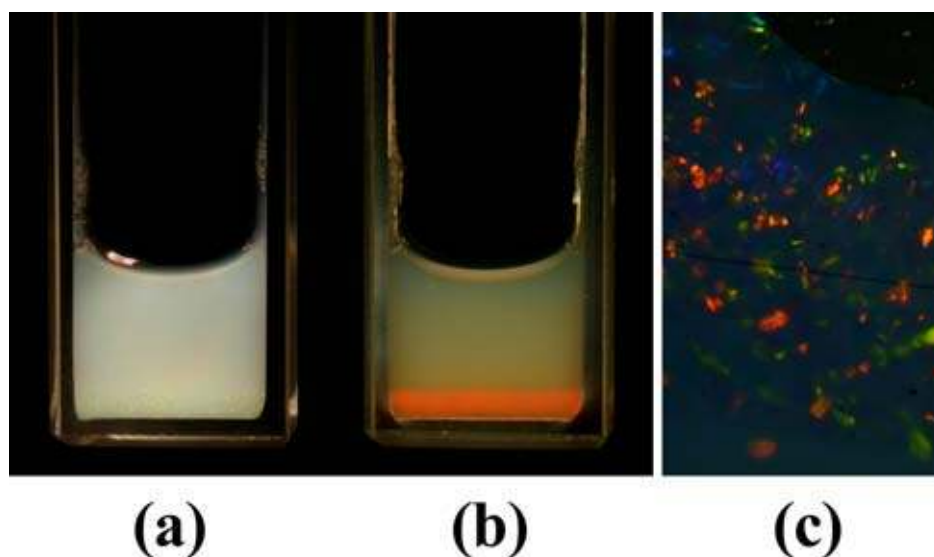


Figure 8.3 – Phase separated sample in I-C equilibrium, (a) illuminated by white light and (b) between crossed polarisers. (c) depicts a close-up of Bragg reflections in another columnar sample. The Bragg reflections stem from the two-dimensional hexagonal lattice of columns of platelets, with a lattice spacing of about 200 nm. (See colour version at page 139.)

nematic phase is not observed anymore. Suspensions at 1 and 0.1 mM NaCl show an isotropic phase at low gibbsite concentration (< 170 g/l) and I-C phase separation on increasing particle concentration. The columnar phase is easily identified by the presence of Bragg reflections; see Fig. 8.3. The relative amount of columnar phase increases with increasing particle concentration, up to the point where the samples become fully columnar (1 mM) or gel (0.1 mM). All observations are depicted in a phase diagram, Fig. 8.4. Note that the slope of the sol-gel line is opposite to that of clay suspensions studied earlier [166,168,169]. Apparently, as opposed to these clays, in our suspensions repulsion dominates the interparticle interactions. One exception has to be noted, however. Levitz and co-workers [179] find repulsive behaviour in Laponite suspensions at very low ionic strength as well.

In order to compare our results with other ones, it is necessary to express our mass concentrations in dimensionless number densities (ND^3/V). It can easily be shown that the volume fraction ϕ of monodisperse hexagonal platelets in solution equals

$$\phi = \rho \frac{3}{8} \sqrt{3} D^2 L, \quad (8.1)$$

with D and L being the diameter and thickness of the particle, respectively, and $\rho = N/V$ being the number density. For polydisperse particles, Eq. (8.1) becomes

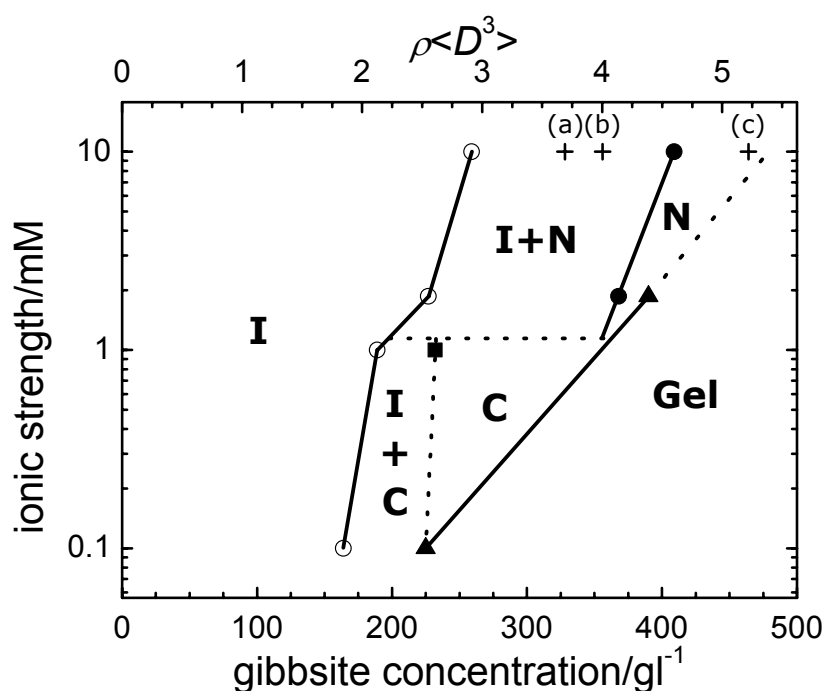


Figure 8.4 – Experimental phase diagram of the gibbsite suspension. Boundaries between the phase regions are indicated with solid lines. Dashed lines indicate tentative phase boundaries. The plus signs and accompanying characters refer to the samples in Fig. 8.2.

Table 8.2 – Comparison of the I-N phase transition densities of our suspension with those of other studies.

ref.	method	$\rho_{iso}\langle D^3 \rangle$	$\rho_{nem}\langle D^3 \rangle$
[14,89]	MC with hard platelets, 19% polydisperse ^a	3.2	4.0
[22]	experiment with hard platelets	2.5	2.7
[181]	theory on charged Laponite clay platelets	3.2	
this study	experiment with charged platelets at 10 mM	2.9	4.6

^a From MC computer simulations, phase transition densities were found for monodisperse hexagonal disks [89] and polydisperse circular disks [14]. Following Bates [89], we find $\rho_{iso}D^3 = 3.2$ and $\rho_{nem}D^3 = 4.0$ as an estimate for 19% polydisperse hexagonal disks.

$$\phi_{pol} = \rho \frac{3}{8} \sqrt{3} \langle D^2 L \rangle = \rho \frac{3}{8} \sqrt{3} \frac{\langle D^2 L \rangle}{\langle D^3 \rangle} \langle D^3 \rangle. \quad (8.2)$$

Following Van der Kooij and co-workers [180], we assume that D and L are uncorrelated and that the particle diameter distribution is symmetric, so $\langle D^3 \rangle / \langle D \rangle^3 = 1 + 3\sigma_D^2$ and $\langle D^2 \rangle / \langle D \rangle^2 = 1 + \sigma_D^2$ with σ being the diameter polydispersity. This yields

$$\phi_{pol} = \frac{3}{8} \sqrt{3} \frac{\langle L \rangle}{\langle D \rangle} \frac{(1 + \sigma_D^2)}{(1 + 3\sigma_D^2)} \rho \langle D^3 \rangle, \quad (8.3)$$

which in turn can be rewritten as

$$\rho \langle D^3 \rangle = \frac{8}{9} \sqrt{3} \frac{\langle D \rangle}{\langle L \rangle} (1 + 2\sigma_D^2) \phi_{pol}. \quad (8.4)$$

The core volume fraction is related to the mass concentration through the mass density of gibbsite (2420 kg/m³). In our suspensions, the I-N phase transition, at 10 mM ionic strength, occurs between 260 g/l and 410 g/l, yielding dimensionless densities of $\rho_{iso} D^3 = 2.9$ and $\rho_{nem} D^3 = 4.6$. Table 8.2 shows our results in comparison with that of other experimental [22] and theoretical [181] work and computer simulations [14,89]. Because the I-N phase transition is driven by the excluded volume, electrostatic effects are of crucial importance. We take this into account by using effective particle dimensions, as explained below. As stated earlier, the main issue of this paper is the observation of two different regimes in one suspension. At relatively high ionic strength, the I-N phase transition is observed, while at low ionic strength, the I-C transition occurs. This can be understood on the basis of the phase diagram of Veerman and Frenkel, obtained by Monte Carlo (MC) computer simulations [13]. They studied cut spheres as a model system for hard platelets and found the I-N transition occurring for aspect ratios smaller than $L/D = 1/7$, while the I-C transition occurred for ratios larger than $L/D = 1/7$. Our charged particles are not hard platelets; still we can map them on a hard platelet system by introducing an *effective* diameter and *effective* thickness, a notion that goes back to Onsager himself [10,11]. In such a description, the effective diameter of a platelet can be regarded as the core dimension plus some constant times the Debye length. Let us assume that this holds for the thickness as well and that the constant is the same for the diameter and thickness. In that case

$$\begin{aligned} L^{eff} &= L^{core} + a\kappa^{-1} \\ D^{eff} &= D^{core} + a\kappa^{-1} \end{aligned} \quad (8.5)$$

where a is the constant to be determined and κ^{-1} is the Debye length. From Fig. 8.4, our experimental phase diagram, it appears that the ionic strength at the changeover is 1.2 ± 0.2 mM, which corresponds to a Debye length of 9.1 nm. The effective aspect ratio L^{eff}/D^{eff} at the changeover must be 1/7. Together with the core dimensions from Table 8.1 and Eq. (8.5) this yields $a = 2.0$. In other words, the interparticle distance at which two platelets presumably have a repulsion of about kT is 2.0 times the Debye length, which agrees with the value that Stroobants and co-workers found for charged rods [182], *i.e.*, $a = 2.9$.

However, this hard platelet picture fails. The core volume fractions at which the I-C phase transition occurs (at 1.2 mM) are $\phi_I^{core} = 0.08$ and $\phi_C^{core} = 0.10$. It can easily be shown that the *effective* volume fraction is related to the *core* volume fraction as follows:

$$\phi^{eff} = \left(\frac{L^{eff}}{L^{core}} \right) \left(\frac{D^{eff}}{D^{core}} \right)^2 \phi^{core}, \quad (8.6)$$

where we now explicitly use superscripts. (Note that in Eqs. (8.1) - (8.4), the core volume fraction is used although this is not explicitly mentioned.) The effective volume fractions

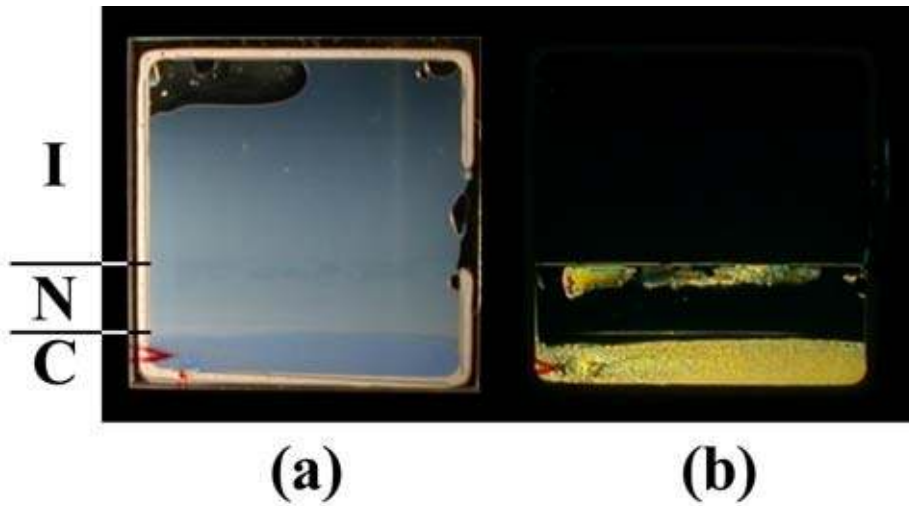


Figure 8.5 – An initially biphasic (I-N) sample that developed a third phase (C) over a timescale of six months. (a) depicts the sample in reflection with white light, and (b) in transmission between crossed polarisers. Again, Bragg reflections can be observed in the columnar phase; see (a). In (b), the major part of the nematic phase appears dark, this is because of the alignment of the platelets along the wall (homeotropic alignment). (See colour version at page 139.)

Chapter 8

Table 8.3 – Relative heights of the phases in the sample in sedimentation equilibrium, as measured in our experiment and calculated with the osmotic compression model.

	experiment	model
I	0.61	0.54
N	0.21	0.13
C	0.18	0.33

consequently are $\phi_I^{\text{eff}} = 0.22$ and $\phi_C^{\text{eff}} = 0.26$. These values should be compared with $\phi_I \cong 0.45$ and $\phi_C \cong 0.50$ that follow from the simulations of Veerman and Frenkel [13]. Clearly, the soft repulsive tail of the electric double layer between the platelets lowers the effective volume fractions at which the I-C transition occurs.

8.3.2 Phase behaviour as explored by gravity.

As mentioned before, the suspensions at 10 mM become fully nematic, but the columnar phase does not show up at this ionic strength because of gelation. However, by letting gravity act on our suspensions, we have been able to induce a high particle concentration in a very gentle way, avoiding the formation of a gel. A sample containing isotropic and nematic phase in coexistence (in a 60:40% ratio) was left at room temperature to observe the effect of gravity. After 6 months, we found that the sample contained three phases instead of the initial two, the upper two phases being isotropic and nematic, respectively, whereas the lower phase appeared to be columnar; see Fig. 8.5. This columnar phase shows a grainy texture and bright Bragg reflections due to the two-dimensional positional order. The measured relative heights of the phases are listed in Table 8.3. Close inspection of the sample reveals a particle concentration gradient as a function of height, indicating a balance between gravity and osmotic pressure. Using a simple model, which has been presented in Chapter 3 of this thesis, this balance and the resulting three-phase equilibrium can be described qualitatively. We have shown that each phase α has a height

$$H^\alpha = -\xi \int_{c_{\text{bottom}}^\alpha}^{c_{\text{top}}^\alpha} \frac{1}{c} \frac{\partial \tilde{\Pi}_\alpha}{\partial c} dc, \quad (8.7)$$

where we have introduced the gravitational length scale $\xi = k_B T / m^* g$, with buoyant mass m^* , and the reduced quantities $\tilde{\Pi} = \Pi D^3 / k_B T$ and $c = \rho D^3$, with number density ρ . Furthermore, it is found that the average concentration \bar{c}_α of each phase is given by

$$\bar{c}^\alpha = -\frac{\xi}{H^\alpha} \int_{c_{bottom}^\alpha}^{c_{top}^\alpha} \frac{\partial \tilde{\Pi}_\alpha}{\partial c} dc = \frac{\xi}{H^\alpha} \left[\tilde{\Pi}_\alpha(c_{bottom}^\alpha) - \tilde{\Pi}_\alpha(c_{top}^\alpha) \right]. \quad (8.8)$$

This result simply expresses hydrostatic equilibrium in which the difference in osmotic pressure above and below a layer is balanced by the weight of the layer. Interestingly, noting that

$$H^{sample} = \sum_a H^\alpha, \quad (8.9)$$

we find that Eq. (8.8) holds for the complete sample as well:

$$\bar{c}^{sample} = \frac{\xi}{H^{sample}} \left[\tilde{\Pi}(c_{bottom}^{sample}) - \tilde{\Pi}(c_{top}^{sample}) \right], \quad (8.10)$$

just like the case of one phase. This equation, together with Eqs. (8.7) and (8.9), allows for explicit calculation of c_{top} and c_{bottom} and, hence, the sedimentation profile once the equation of state (EOS) is known. For charged platelets, no EOS is known. However, a hard-platelet EOS was given by Zhang and co-workers [44] for platelets with an aspect ratio of 1/10. We take this EOS for a qualitative approach to the problem, resulting in a calculated sedimentation profile that is shown in Fig. 8.6 and the corresponding phase-

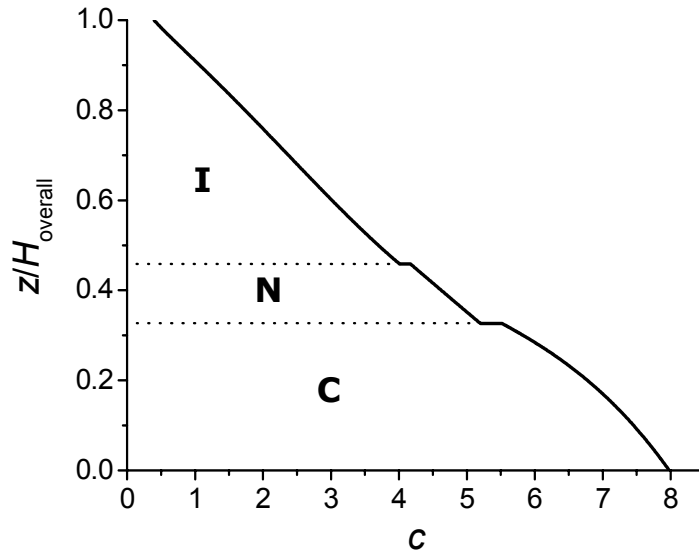


Figure 8.6 – The sedimentation profile (relative height vs. concentration) that was calculated using the osmotic compression model. The overall concentration was set to $c = 4.1$ (in the I-N biphasic gap) as dictated by the experiment.

heights in Table 8.3. Apparently, this approach describes the sample reasonably well.

8.4 Conclusion

Our work demonstrates that it is possible to synthesise charged colloidal platelets that systematically display the I-N phase transition, dispelling the mystery of the I-N transition in such systems. Modification of the particle surface with cationic aluminium tridecamers appears to play an essential role in facilitating liquid crystal formation. In addition, through variation of the ionic strength, we have been able to tune the effective aspect ratio of the platelets. This enabled us to observe both the I-N and I-C phase transition in one suspension, a scenario predicted by MC computer simulations a decade ago.

The effect of gravity is quite important. A biphasic (I-N) sample became triphasic (I-N-C) after standing for several months, which is described by a simple osmotic compression model that we developed. In the next chapter, we will study the same kind of aqueous gibbsite dispersion in a centrifugal field at 900 G.

9

Formation of a columnar phase of charged colloidal platelets in a centrifugal field

Abstract

Sediments of aqueous dispersions of gibbsite platelets were obtained by centrifuging at 900 G. The observed Bragg reflections in the sediments suggest the formation of a columnar phase. The order of the colours of the reflections suggests size fractionation of the platelets, with the largest ones accumulating at the bottom of the sample. Small-angle X-ray scattering measurements and real space transmission electron microscopy images of different fractions of the sediment confirm the existence of a columnar phase and significant size fractionation.

9.1 Introduction

Sedimentation in the earth's gravitational field is a convenient means to concentrate colloidal suspensions that takes advantage of the difference between the mass density of the particles and solvent. It can be used to prepare iridescent phases of colloidal spheres [183,184], rods [29,30,33] and platelets (see Chapter 8). Although this process is very slow – it may take months to years – the inherent slowness of the sedimentation assists the phase separation process. The sedimentation process can be accelerated using a centrifuge.

Centrifugation is a well-known technique in the study of mesoscopic systems and it has been applied extensively in the field of colloid and biochemistry [185]. It can be used both

Chapter 9

as a preparative technique, *e.g.*, in the separation of cell constituents in biology, and as an analytical tool, like in the characterisation of colloidal particles on the basis of their sedimentation velocity. Although it may seem to be a very simple technique, it has led to several very important discoveries. In the study of colloidal gibbsite platelets, centrifugation is the most convenient way to concentrate samples, *e.g.*, for phase behaviour studies as presented in Chapters 2 and 8.

An important parameter in sedimentation studies is the gravitational length scale ξ , which we have used before in Chapters 3 and 8. It gives the height that an object must be lifted – in a gravitational field – to increase its potential energy by $1 kT$. It can be shown that, in the case of centrifugation, it is given by [79,185]

$$\xi = \frac{kT}{m^* \omega^2 r}, \quad (9.1)$$

where $m^* = v_p (\rho_p - \rho_0)$ denotes the buoyant mass of the particles, with v_p the particle volume and ρ_p and ρ_0 the particle and solvent mass density, respectively, ω the rotation speed, and \bar{r} the average distance to the rotation axis. For our colloidal gibbsite platelets, the gravitational height is about 1 mm in the earth's gravitational field, which is about 5000 particle diameters. However, in the centrifugation experiments that we perform, it reduces to about 1 μm and becomes only 5 particle diameters. In that respect, it is remarkable that, as often as we centrifuge an aqueous dispersion of gibbsite platelets, we obtain an iridescent sediment with colours that vary over the visible spectrum when illuminated with white light; an example is shown in Fig. 9.1. The distinct Bragg reflections are an indication of positional – likely columnar – order in the sediment. In contrast, suspensions of colloidal spheres centrifuged at 1000 G typically yield amorphous sediments that do not show Bragg reflections at all. (We note that micrometre-sized spheres, sedimenting in the earth's gravitational field and having a gravitational length that is smaller than their diameter, still form crystalline sediments on a flat wall [186,187].)

One exception has to be mentioned, however. In the 1950s, tipula iridescent virus (TIV) particles, with the shape of a regular icosahedron and a diameter of about 130 nm, were found to exhibit iridescent layers when centrifuged [188,189]. In fact, this is the first observation of a synthetic colloidal crystal. The TIV sediment showed Bragg reflections with “*a smooth gradation in colour ranging from violet at the bottom through green to red at the top*” [188]. This gradation can be understood on the basis of osmotic compression. Surprisingly, we find exactly the opposite: in our sediment, the Bragg reflections with longest wavelengths (green) are found at the bottom, while the shortest wavelengths (violet) are found at the top; see Fig. 9.1. Hence, our observations cannot be explained on the basis of osmotic compression effects. We suggest that the “reversed” colour gradient is due to significant size fractionation, with the largest particles accumulating at the bottom.

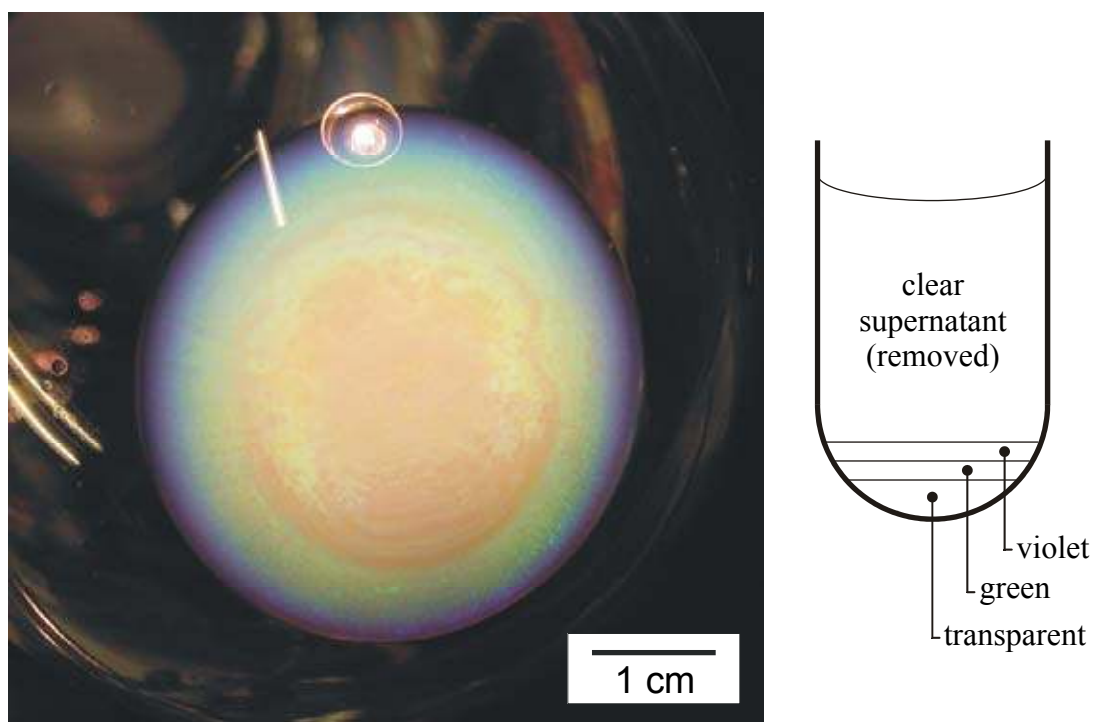


Figure 9.1 – The preparation of charge-stabilised gibbsite platelets involves a sequence of sedimentation and redispersion to remove excess Al_{13} ions. After the first sedimentation step the sediment, as depicted from below on the photograph, shows bright green and violet Bragg reflections, indicative of the columnar phase. The bottom part is a transparent glass-like layer. (See colour version at page 140.)

Triggered by these considerations, we decided to study the sediment in detail. From small-angle X-ray scattering (SAXS) measurements, we obtain the lattice spacing and its evolution with the height in the sediment, demonstrating the presence of a columnar phase. Following Maeda and Maeda [190], we used real space imaging on a rapidly frozen sample to investigate the composition of the sediment at different heights, confirming that size fractionation takes place.

9.2 Experiment

We performed this study with the same dispersion as was used in the previous chapter and refer to Section 8.2 for the details on synthesis and characterisation. A transmission electron micrograph of this dispersion is shown in Fig. 9.2. The preparation of our charge-stabilised gibbsite platelets involves treatment of the particles with Al_{13} ions to increase their surface charge. After this treatment, excess Al_{13} ions are removed by a sequence of sedimentation and redispersion (27 h at 900 G). After the first sedimentation step, the sediment shows bright green and violet Bragg reflections, indicative of the columnar phase, see Fig. 9.1. The lower part of the sediment consists of a rather transparent layer. On top of

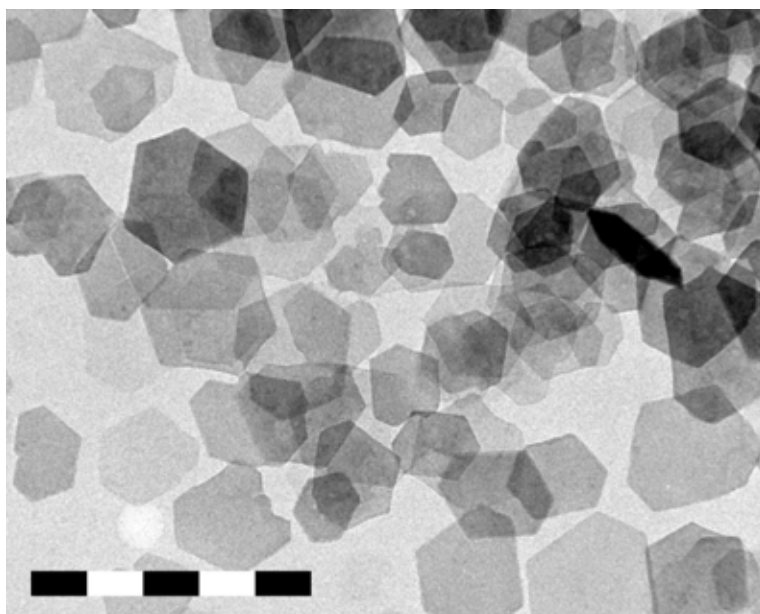


Figure 9.2 – TEM micrograph of the parent suspension. The scale bar denotes 500 nm. Fig. 9.6 shows the particle diameter distribution.

that is a more turbid layer, displaying green Bragg reflections in the lower part, and violet reflections in the upper part. After the second and third sedimentation step, replacing the supernatant by NaCl-solution, the Bragg reflections are less intense. Clearly, the Al_{13} tridecamers removed in the sequence play an important role, perhaps as a depleting agent. In Chapter 2 we have found that the presence of a depleting agent enhances the formation of columnar crystals in suspensions of sterically stabilised gibbsite platelets and such a scenario may occur here as well.

We prepared a sample to study the sediment with small-angle X-ray scattering (SAXS). From the dispersion described above, we took a sample just before the first sedimentation step. After concentrating the sample ten times (in order to obtain enough material to create a high enough sediment), we put it in a flat capillary with internal dimensions $0.3 \times 3 \text{ mm}^2$. Gibbsite content in this sample was about 70 g/l and the aluminium chlorohydrate concentration 5 g/l. The sample was centrifuged for 26 h at 900 G. Subsequently, the supernatant was removed and the capillary was flame sealed to conserve the sediment. The sediment showed the bright green and violet Bragg reflections that are also visible in Fig. 9.1. Moreover, almost two years after preparation, these Bragg reflections are still present and have hardly diminished, proving that the columnar phase is well conserved.

We have measured SAXS patterns at increasing heights from the bottom to the top of the sediment. We used the SAXS setup of the Dutch-Belgian beamline BM-26 DUBBLE at the European Synchrotron Radiation Facility (ESRF, Grenoble, France).

The scattered X-rays were detected by a phosphor screen coupled to a 16-bit CCD camera (Photonic Science) with a pixel size of 22 μm . An X-ray beam of 18 keV (wavelength $\lambda =$

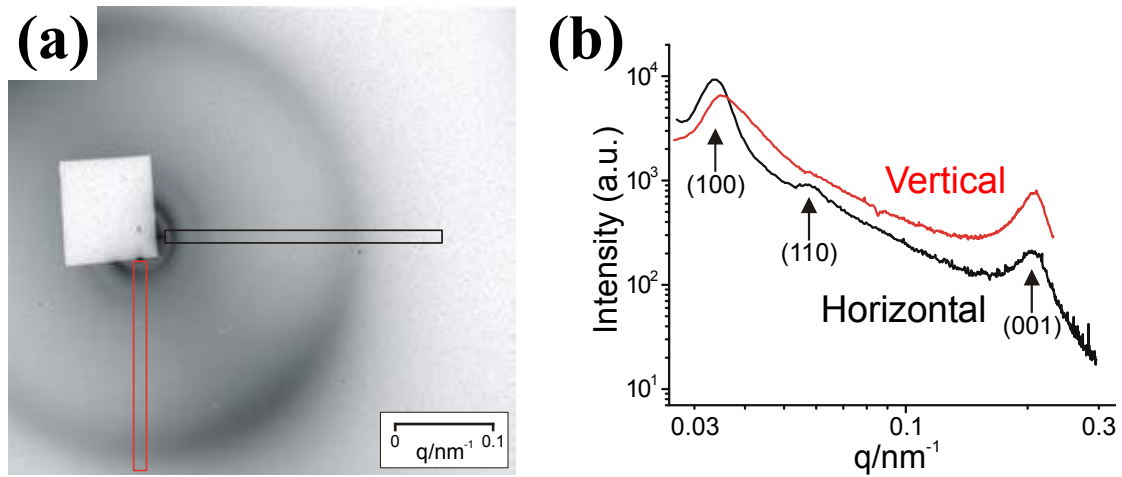


Figure 9.3 – (a) an example of a SAXS pattern, at $y = 2$ mm above the bottom of the tube, and (b) the corresponding horizontal and vertical slices through the pattern. The (100) peak and liquid-like (001) peak are clearly observed, whereas the (110) peak, although not as strong, can still be discerned. In the horizontal direction, the (100) maximum is located at a lower q -value than in the vertical direction, indicating anisotropic deformation of the sediment. The nearest-neighbour distances calculated from $q_{(100)}$ and $q_{(110)}$, and $q_{(001)}$ are given in Fig. 9.4.

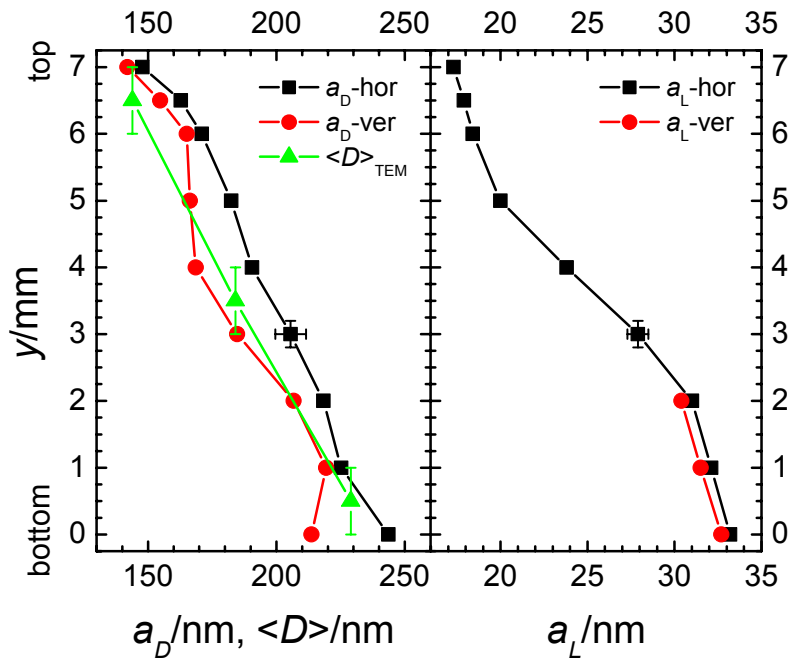


Figure 9.4 – The inter- ($a_D = \frac{4}{3} \pi \sqrt{3} \sqrt{h^2 + hk + k^2} / q_{(hk0)}$) and intra-columnar ($a_L = 2\pi / q_{(001)}$) nearest-neighbour distances and the average platelet diameter $\langle D \rangle$ as a function of height in the sediment. a_D and a_L have been obtained by SAXS measurements and $\langle D \rangle$ by real space imaging with TEM. Error bars denote the typical error in the SAXS measurements.

Chapter 9

0.689 Å) and a sample-detector distance of about 5 m were used. The accessible q -range was 0.026 to 0.37 nm⁻¹ in the horizontal and 0.026 to 0.23 nm⁻¹ in the vertical direction. The setup was calibrated using the fibre diffraction peaks of dry rat-tail collagen fiber, which has strong characteristic peaks at $q = 2\pi n / 65.0$ nm⁻¹ ($n = 1, 2, 3$).

In addition to the SAXS analysis, we have prepared a sample for investigation with transmission electron microscopy (TEM). We filled a cell with the same (10 times concentrated) stock dispersion. After centrifuging the sample, we immersed it in liquid N₂ to instantaneously freeze the complete sample. The sediment was subsequently cut into slices, each 1 mm thick. Care was taken to avoid melting of the sample during this procedure. Each slice was dispersed in a water-ethanol mixture, from which copper grids were prepared for TEM. From three of the slices, taken at heights $y = 0.5, 3.5, \text{ and } 6.5$ mm, TEM micrographs were obtained. Image analysis software was used to determine the average platelet diameter and polydispersity in the fractions.

9.3 Results and discussion

The bright Bragg reflections in the sediment already hint at the presence of a columnar phase. This is confirmed by the SAXS measurements. A typical SAXS pattern is shown in Fig. 9.3, together with horizontal and vertical slices. The maxima in the scattering patterns are indexed by Miller indices (hkl). For a columnar phase (with hexagonal packing) we expect reflections perpendicular to the columns with $q_{(hk0)}$ proportional to $\sqrt{h^2 + hk + k^2}$, while we use l to indicate (liquid-like) order within the columns. The SAXS patterns indeed show maxima with q -ratios $1:\sqrt{3}$, as well as a broad liquid-like peak at large angle. The (200) and (210) higher-order peaks are not observed in this study, in contrast to our study of sterically stabilised gibbsite platelets in Chapter 2. In view of the ring-like diffraction and the fact that the (100) and (001) peaks are visible at the same time, we are led to the conclusion that we deal with a columnar phase that consists of many small domains, yielding powder diffraction. The sediment in Fig. 9.1 indeed appears to consist of numerous small crystallites.

From the scattering maxima, we obtain nearest-neighbour distances between ($a_D = \frac{4}{3}\pi\sqrt{3}\sqrt{h^2 + hk + k^2}/q_{(hk0)}$) and within ($a_L = 2\pi/q_{(001)}$) the columns as given in Fig. 9.4. Following the same procedure as in Chapter 3, the visual observations allow us to make a crude estimate of a_D as 210 and 160 nm in the bottom and top part, respectively, agreeing with the SAXS measurements.

From Fig. 9.4, it appears that both the inter- and intra-columnar nearest-neighbour distances increase upon going down in the sediment. This observation suggests size fractionation, with the largest particles accumulating at the bottom of the vessel. To shed light on this issue, we have studied the sediment at different heights using real space imaging with TEM. Fig. 9.5 shows three representative TEM micrographs that demonstrate

Formation of a columnar phase of charged colloidal platelets in a centrifugal field

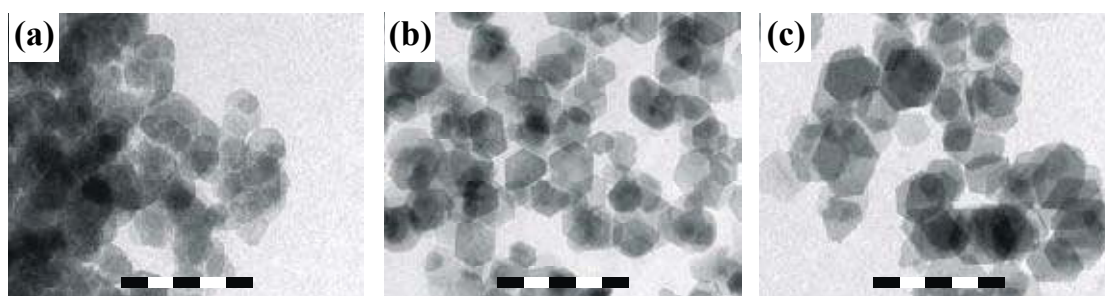


Figure 9.5 – TEM micrographs of three slices at heights (a) $y = 6.5$, (b) 3.5 , and (c) 0.5 mm. The scale bars each denote 500 nm.

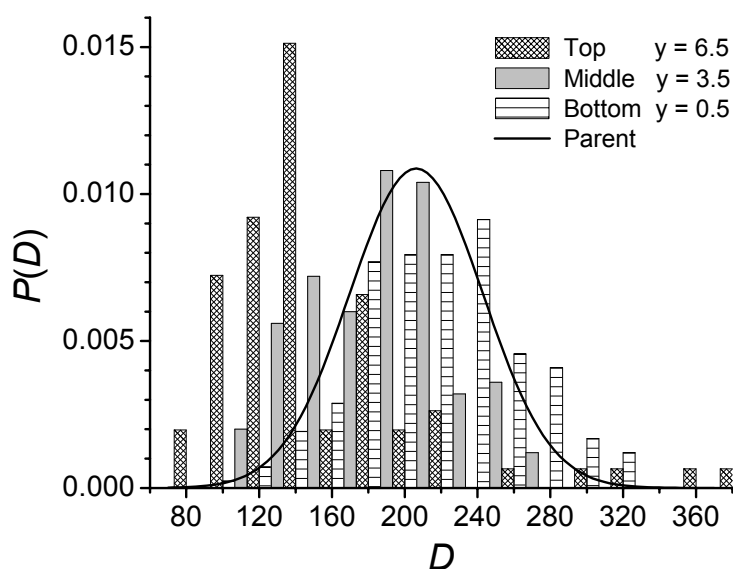


Figure 9.6 – Particle diameter distributions of the three studied sediment fractions as well as the parent suspension (Gaussian fit). (See colour version at page 140.)

Table 9.1 – Average particle diameter $\langle D \rangle$ and diameter polydispersity σ_D (in absolute and relative units) in the parent suspension and the three sediment fractions, as obtained from TEM.

	$\langle D \rangle$	σ_D
parent suspension	202 nm	38 nm (19 %)
top, $y = 6.5$ mm	144 nm	59 nm (41%)
middle, $y = 3.5$ mm	184 nm	38 nm (21%)
bottom, $y = 0.5$ mm	229 nm	44 nm (19%)

Chapter 9

the size fractionation. Fig. 9.6 shows the particle diameter distributions of the parent suspension and the three fractions as obtained from TEM micrographs; Table 9.1 gives the average diameter $\langle D \rangle$ and diameter polydispersity σ_D of these samples. Note that, although the absolute value of the polydispersity does not change very much, relative to the average platelet diameter it decreases by about a factor 2. In another study, this feature is exploited to reduce the size polydispersity of colloidal gibbsite platelets [191]. Due to their rather anisotropic shape, the gibbsite platelets are hardly imaged edgewise with TEM. This makes analysis of the thickness distribution in the sediment practically not possible with this technique. With atomic force microscopy, such an approach would likely be feasible. In Fig. 9.4 the average platelet diameter is plotted as a function of the height in the sediment.

As can be seen in the figure, the average particle diameter is almost equal to the inter-columnar spacing throughout the sediment, suggesting that there is hardly any further compression of the columns possible. However, there appears to be a slight difference in a_D -spacings along the horizontal and vertical direction, at each height. It could point to anisotropic deformation of the columnar crystallites. In the centrifugal field it is possible to have anisotropic deformation because $\xi \sim D$. However, the measurements are performed at normal gravity, where $\xi \gg D$, and one expects isotropic compression. Still, our sediment seems to be stuck because it retains the anisotropic deformation.

Furthermore, the relative change in a_D – over the height of the sediment – is a factor of about 1.5, whereas a_L varies with a factor of 2. If there is compression within the columns, the fractionation in the platelet thickness $\langle L \rangle$ would have to be even stronger than a factor of 2. To draw any further conclusions, we need to measure the average platelet thickness in several sediment fractions.

Recently, there has been a study of the equation of state of a dense columnar liquid crystal of hard (monodisperse) cylindrical disks [49] that gives a relation between the inter- and intra-columnar compression and the density of the columnar phase. It follows that if $a_D \approx \langle D \rangle$, like in our sample, one would expect that the volume fraction approaches that of close packing, $\phi_{cp} \cong 0.91$. However, we find an estimate that is much lower. From the initial gibbsite concentration of 70 g/l and the sample and sediment heights, 57 and 7 mm, respectively, we estimate the gibbsite concentration in the sediment at 570 g/l. Using the mass density of gibbsite (2400 g/l), this yields a gibbsite core volume fraction of $\phi^{core} \approx 0.24$. (The effective volume fraction, taking into account the Debye length, will only be slightly higher due to the presence of a large amount of multivalent ions.)

Although $\phi_{core} < \phi_{cp}$, it appears to be exactly in between the *random*-close-packing volume fractions of hard platelets with aspect ratios of $L/D = 1/10$ ($\phi_{rcp} = 0.32$) and $1/20$ ($\phi_{rcp} = 0.18$) [192]. This suggests that the sediment consists of a significant fraction of

randomly close-packed parts, which explains the relatively high level of background scattering in Fig. 9.3.

In this study, we find strong size fractionation in the gibbsite dispersion at 900 G. The question arises as to whether one expects strong fractionation in the sample studied in Chapter 8. There, we have used the same colloidal dispersion, which showed multiple phases in equilibrium due to sedimentation, albeit at only 1 G. The two important factors that determine the sedimentation behaviour of (colloidal) particles are the sedimentation velocity and the gravitational length scale, both favouring the largest particles at the bottom of the sediment. A comparison of the previous study (Chapter 8) with the current one, however, is not straightforward, although intuitively one may expect stronger fractionation in stronger gravitational fields. In a study of the sedimentation behaviour of polydisperse hard spheres, it was found that the problem of a settling multi-component mixture is difficult to solve [79]. However, detailed results for the density profiles of concentrated bidisperse hard-sphere colloidal suspensions in sedimentation equilibrium have been given [86].

9.4 Conclusion

We have observed green and violet Bragg reflections in sediments of aqueous dispersions of gibbsite platelets, suggesting that a columnar phase is formed.

Moreover, the order of the colours, *i.e.*, violet on top and green at the bottom, opposes earlier experiments employing colloidal spheres (tipula iridescent virus) that show gravitational compression. Hence we suggest strong size fractionation of the platelets, with the largest platelets accumulating at the bottom of the sample.

From small-angle X-ray scattering measurements, we find that the sediment has indeed columnar signature and that the lattice spacing increases upon going down in the sediment. Investigation of three slices of the sediment (taken at different heights) by transmission electron microscopy confirms that size fractionation takes place.

In conclusion, we have shown that through the action of gravity, we are able to produce new phases, as shown in Chapter 8. Moreover, the application of very high gravitational fields does not appear to hinder the formation of a columnar phase.

Chapter 9

References

- [1] J. Perrin, *Mouvement Brownien et Réalité Moléculaire*, Ann. de Chim. et de Phys. **18**, 5 (1909).
- [2] J. Perrin, *Les Atomes* (Libr. Felix Alcan, Paris, 1920).
- [3] B. J. Alder and T. A. Wainwright, *Phase transition for a hard sphere system*, J. Chem. Phys. **27**, 1208 (1957).
- [4] W. W. Wood and J. D. Jacobson, *Preliminary results from a recalculation of the Monte Carlo equation of state of hard spheres*, J. Chem. Phys. **27**, 1207 (1957).
- [5] S. Asakura and F. Oosawa, *On interaction between two bodies immersed in a solution of macromolecules*, J. Chem. Phys. **22**, 1255 (1954).
- [6] A. Vrij, *Pure and Applied Chemistry* **48**, 471 (1976).
- [7] I. Langmuir, *The Role of Attractive and Repulsive Forces in the Formation of Tactoids, Thixotropic Gels, Protein Crystals and Coacervates*, J. Chem. Phys. **6**, 873 (1938).
- [8] H. Zocher, *Über freiwillige Strukturbildung in Solen*, Z. Anorg. Chem. **147**, 91 (1925).
- [9] F. C. Bawden, N. W. Pirie, J. D. Bernal, and I. Fankuchen, *Liquid crystalline substances from virus infected plants*, Nature **138**, 1051 (1936).
- [10] L. Onsager, *Anisotropic Solutions of Colloids*, Phys. Rev. **62**, 558 (1942).
- [11] L. Onsager, *The Effects of Shape on the Interaction of Colloidal Particles*, Ann. N. Y. Acad. Sci. **51**, 627 (1949).
- [12] D. Frenkel and R. Eppenga, *Monte Carlo Study of the Isotropic-Nematic Transition in a Fluid of Thin Hard Disks*, Phys. Rev. Lett. **49**, 1089 (1982).
- [13] J. A. C. Veerman and D. Frenkel, *Phase behavior of disklike hard-core mesogens*, Phys. Rev. A **45**, 5632 (1992).
- [14] M. A. Bates and D. Frenkel, *Nematic-isotropic transition in polydisperse systems of infinitely thin hard platelets*, J. Chem. Phys. **110**, 6553 (1999).
- [15] J. Vieillard-Baron, *The equation of state of a system of hard spherocylinders*, Mol. Phys. **28**, 809 (1974).
- [16] D. Frenkel and B. M. Mulder, *The hard ellipsoid-of-revolution fluid - I. Monte carlo simulations*, Mol. Phys. **55**, 1171 (1985).
- [17] R. H. Marchessault, F. F. Morehead, and N. M. Walter, Nature **184**, 632 (1959).
- [18] J. Bugosh, *Colloidal Alumina - The Chemistry and Morphology of Colloidal Boehmite*, J. Phys. Chem. **65**, 1789 (1961).
- [19] J. Lapointe and D. A. Marvin, *Filamentous bacterial viruses VIII. Liquid crystals of fd*, Mol. Cryst. Liq. Cryst. **19**, 269 (1973).
- [20] T. Folda, H. Hoffmann, H. Chanzy, and P. Smith, *Liquid crystalline suspensions of poly(tetrafluoroethylene) 'whiskers'*, Nature **333**, 55 (1988).
- [21] J. Tang and S. Fraden, *Isotropic-cholesteric phase transition in colloidal suspensions of filamentous bacteriophage fd*, Liq. Cryst. **19**, 459 (1995).
- [22] F. M. van der Kooij and H. N. W. Lekkerkerker, *Formation of Nematic Liquid Crystals in Suspensions of Hard Colloidal Platelets*, J. Phys. Chem. B **102**, 7829 (1998).
- [23] M. P. B. van Bruggen, M. Donker, H. N. W. Lekkerkerker, and T. L. Hughes, *Anomalous stability of aqueous boehmite dispersions induced by hydrolyzed aluminium poly-cations*, Colloids Surf. A **150**, 115 (1999).
- [24] M. P. B. van Bruggen, J. K. G. Dhont, and H. N. W. Lekkerkerker, *Morphology and Kinetics of the Isotropic-Nematic Phase Transition in Dispersions of Hard Rods*, Macromolecules **32**, 2256 (1999).

References

- [25] B. J. Lemaire, P. Davidson, J. Ferré, J. P. Jamet, P. Panine, I. Dozov, and J. P. Jolivet, *Outstanding Magnetic Properties of Nematic Suspensions of Goethite (α -FeOOH) Nanorods*, Phys. Rev. Lett. **88**, 125507 (2002).
- [26] D. van der Beek and H. N. W. Lekkerkerker, *Nematic ordering vs. gelation in suspensions of charged colloidal platelets*, Europhys. Lett. **61**, 702 (2003).
- [27] S. Liu, J. Zhang, N. Wang, W. Liu, C. Zhang, and D. Sun, *Liquid-Crystalline Phases of Colloidal Dispersions of Layered Double Hydroxides*, Chem. Mater. **15**, 3240 (2003).
- [28] B. J. Lemaire, P. Davidson, J. Ferré, J. P. Jamet, D. Petermann, P. Panine, I. Dozov, D. Stoenescu, and J. P. Jolivet, *The complex phase behaviour of suspensions of goethite (α -FeOOH) nanorods in a magnetic field*, Faraday Discuss. **128**, 271 (2005).
- [29] G. Oster, *Two-phase formation in solutions of Tobacco Mosaic Virus and the problem of long-range forces*, J. Gen. Physiol. **33**, 445 (1950).
- [30] U. Kreibig and C. Wetter, *Light Diffraction of in vitro Crystals of Six Tobacco Mosaic Viruses*, Z. Naturforsch. **35 c**, 750 (1980).
- [31] F. P. Booy and A. G. Fowler, *Cryo-electron microscopy reveals macromolecular organization within biological liquid crystals seen in the polarizing microscope*, Int. J. Biol. Macromol. **7**, 327 (1985).
- [32] Z. Dogic and S. Fraden, *Smectic Phase in a Colloidal Suspension of Semiflexible Virus Particles*, Phys. Rev. Lett. **78**, 2417 (1997).
- [33] Y. Maeda and S. Hachisu, *Schiller Layers in β -Ferric Oxyhydroxide Sol as an Order-Disorder Phase Separating System*, Colloids Surf. **6**, 1 (1983).
- [34] M. Wadati and A. Isihara, *Theory of liquid crystals*, Mol. Cryst. Liq. Cryst. **17**, 95 (1972).
- [35] M. Hosino, H. Nakano, and H. Kimura, *Nematic-smectic transition in an aligned rod system*, J. Phys. Soc. Jpn. **46**, 1709 (1979).
- [36] M. Hosino, H. Nakano, and H. Kimura, *Effect of orientational fluctuation on nematic-smectic A transition in the system of hard rod molecules*, J. Phys. Soc. Jpn. **47**, 740 (1979).
- [37] M. Hosino, H. Nakano, and H. Kimura, *Phase Transitions in the Systems of Identical Rigid Molecules in Perfect Alignment-Relations of the Smectic A and Columnar Orderings in Liquid Crystals and the Crystalline Ordering to the Molecular Shape*, J. Phys. Soc. Jpn. **51**, 741 (1982).
- [38] B. Mulder, *Density-functional approach to smectic order in an aligned hard-rod fluid*, Phys. Rev. A **35**, 3095 (1987).
- [39] X. Wen and R. B. Meyer, *Model for smectic-A ordering of parallel hard rods*, Phys. Rev. Lett. **59**, 1325 (1987).
- [40] A. Poniewierski and R. Holyst, *Density-Functional Theory for Nematic and Smectic-A Ordering of Hard Spherocylinders*, Phys. Rev. Lett. **61**, 2461 (1988).
- [41] A. Stroobants, H. N. W. Lekkerkerker, and D. Frenkel, *Evidence for Smectic Order in a Fluid of Hard Parallel Spherocylinders*, Phys. Rev. Lett. **57**, 1452 (1986).
- [42] A. Stroobants, H. N. W. Lekkerkerker, and D. Frenkel, *Evidence for one-, two-, and three-dimensional order in a system of hard parallel spherocylinders*, Phys. Rev. A **36**, 2929 (1987).
- [43] D. Frenkel, H. N. W. Lekkerkerker, and A. Stroobants, *Thermodynamic stability of a smectic phase in a system of hard rods*, Nature **332**, 822 (1988).
- [44] S.-D. Zhang, P. A. Reynolds, and J. S. van Duijneveldt, *Phase behavior of mixtures of colloidal platelets and nonadsorbing polymers*, J. Chem. Phys. **117**, 9947 (2002).
- [45] F. M. van der Kooij, K. Kassapidou, and H. N. W. Lekkerkerker, *Liquid crystal phase transitions in suspensions of polydisperse plate-like particles*, Nature **406**, 868 (2000).
- [46] A. B. D. Brown, S. M. Clarke, and A. R. Rennie, *Ordered Phase of Plate-like Particles in Concentrated Dispersions*, Langmuir **14**, 3129 (1998).

- [47] D. van der Beek and H. N. W. Lekkerkerker, *Liquid Crystal Phases of Charged Colloidal Platelets*, *Langmuir* **20**, 8582 (2004).
- [48] D. van der Beek, A. V. Petukhov, S. M. Oversteegen, G. J. Vroege, and H. N. W. Lekkerkerker, *Evidence of the hexagonal columnar liquid crystal phase of hard colloidal platelets by high resolution SAXS*, to appear in *Eur. Phys. J. E* (2005).
- [49] H. H. Wensink, *Equation of State of a Dense Columnar Liquid Crystal*, *Phys. Rev. Lett.* **93**, 157801 (2004).
- [50] A. M. Wierenga, T. A. J. Lenstra, and A. P. Philipse, *Aqueous dispersions of colloidal gibbsite platelets: synthesis, characterisation and intrinsic viscosity measurements*, *Colloids Surf. A* **134**, 359 (1998).
- [51] F. M. van der Kooij, *Phase behaviour and dynamics of suspensions of hard colloidal platelets*, PhD thesis, Utrecht University, Utrecht, The Netherlands (2000).
- [52] J. L. Barrat and J. P. Hansen, *On the stability of polydisperse colloidal crystals*, *J. Phys. (Paris)* **46**, 1547 (1986).
- [53] P. N. Pusey, *The effect of polydispersity on the crystallization of hard spherical colloids*, *J. Phys. (Paris)* **48**, 709 (1987).
- [54] R. McRae and A. D. J. Haymet, *Freezing of polydisperse hard spheres*, *J. Chem. Phys.* **88**, 1114 (1988).
- [55] P. N. Pusey, in *Liquids, Freezing and Glass Transition, Les Houches Session 51, NATO Advanced Study Institute, Series B: Physics*, edited by J. P. Hansen, D. Levesque and J. Zinn-Justin (North-Holland, Amsterdam, 1991), p. 763.
- [56] P. G. Bolhuis and D. A. Kofke, *Monte Carlo study of freezing of polydisperse hard spheres*, *Phys. Rev. E* **54**, 634 (1996).
- [57] J. Torbet and G. Maret, *Fibres of Highly Oriented Pfl Bacteriophage Produced in a Strong Magnetic Field*, *J. Mol. Biol.* **134**, 843 (1979).
- [58] E. Senechal, G. Maret, and K. Dransfeld, *Long-Range Order of Nucleic Acids in Aqueous Solutions*, *Int. J. Biol. Macromol.* **2**, 256 (1980).
- [59] J. Torbet, J. M. Freyssinet, and G. Hudry-Clergeon, *Oriented fibrin gels formed by polymerization in strong magnetic fields*, *Nature* **289**, 91 (1981).
- [60] J. M. Freyssinet, J. Torbet, G. Hudry-Clergeon, and G. Maret, *Fibrinogen and fibrin structure and fibrin formation measured by using magnetic orientation*, *Proc. Natl. Acad. Sci. USA* **80**, 1616 (1983).
- [61] R. Oldenbourg, X. Wen, R. B. Meyer, and D. L. D. Caspar, *Orientational Distribution Function in Nematic Tobacco-Mosaic-Virus Liquid Crystals Measured by X-Ray Diffraction*, *Phys. Rev. Lett.* **61**, 1851 (1988).
- [62] J. Gregory and K. C. Holmes, *Methods of preparing oriented Tobacco Mosaic Virus Solved for X-ray Diffraction*, *J. Mol. Biol.* **13**, 796 (1965).
- [63] M. Imp rator-Clerc and P. Davidson, *An X-ray scattering study of flow-aligned samples of a lyotropic liquid-crystalline hexagonal phase*, *Eur. Phys. J. B* **9**, 93 (1999).
- [64] A. B. D. Brown and A. R. Rennie, *Monodisperse colloidal plates under shear*, *Phys. Rev. E* **62**, 851 (2000).
- [65] A. V. Petukhov, D. G. A. L. Aarts, I. P. Dolbnya, E. H. A. de Hoog, K. Kassapidou, G. J. Vroege, W. Bras, and H. N. W. Lekkerkerker, *High-Resolution Small-Angle X-Ray Diffraction Study of Long-Range Order in Hard-Sphere Colloidal Crystals*, *Phys. Rev. Lett.* **88**, 208301 (2002).
- [66] A. V. Petukhov, I. P. Dolbnya, D. G. A. L. Aarts, G. J. Vroege, and H. N. W. Lekkerkerker, *Bragg Rods and Multiple X-Ray Scattering in Random-Stacking Colloidal Crystals*, *Phys. Rev. Lett.* **90**, 028304 (2003).

References

- [67] F. M. van der Kooij, M. Vogel, and H. N. W. Lekkerkerker, *Phase behavior of a mixture of platelike colloids and nonadsorbing polymer*, Phys. Rev. E **62**, 5397 (2000).
- [68] A. V. Petukhov, I. P. Dolbnya, D. G. A. L. Aarts, and G. J. Vroege, *Destruction of long-range order recorded with in situ small-angle x-ray diffraction in drying colloidal crystals*, Phys. Rev. E **69**, 031405 (2004).
- [69] P. N. Pusey and W. van Meegen, *Phase behaviour of concentrated suspensions of nearly hard spheres*, Nature **320**, 340 (1986).
- [70] F. M. van der Kooij and H. N. W. Lekkerkerker, *Liquid-Crystal Phases Formed in Mixed Suspensions of Rod- and Platelike Colloids*, Langmuir **16**, 10144 (2000).
- [71] D. A. Kofke and P. G. Bolhuis, *Freezing of polydisperse hard spheres*, Phys. Rev. E **59**, 618 (1999).
- [72] S. R. Williams, I. K. Snook, and W. van Meegen, *Molecular dynamics study of the stability of the hard sphere glass*, Phys. Rev. E **64**, 021506 (2001).
- [73] N. B. Wilding and P. Sollich, *Phase equilibria and fractionation in a polydisperse fluid*, Europhys. Lett. **67**, 219 (2004).
- [74] F. M. van der Kooij and H. N. W. Lekkerkerker, *Liquid-Crystalline Phase Behavior of a Colloidal Rod-Plate Mixture*, Phys. Rev. Lett. **84**, 781 (2000).
- [75] A. V. Petukhov, D. van der Beek, R. P. A. Dullens, I. P. Dolbnya, G. J. Vroege, and H. N. W. Lekkerkerker, submitted to Proc. Natl. Acad. Sci. USA (2004).
- [76] R. C. Williams, *Concerted Formation of the Gel of Hemoglobin S*, Proc. Natl. Acad. Sci. USA **70**, 1506 (1973).
- [77] P. D. Ross and A. P. Minton, J. Mol. Biol. **112**, 437 (1977).
- [78] R. W. Briehl and S. Ewert, *Effects of pH, 2,3-diphosphoglycerate and salts on gelation of sickle cell deoxyhemoglobin*, J. Mol. Biol. **80**, 445 (1977).
- [79] A. Vrij, *Sedimentation equilibrium in concentrated, multicomponent particle dispersions. Hard spheres in the Percus-Yevick approximation*, J. Chem. Phys. **72**, 3735 (1980).
- [80] R. S. Crandall and R. Williams, *Gravitational Compression of Crystallized Suspensions of Polystyrene Spheres*, Science **198**, 293 (1977).
- [81] K. Takano and S. Hachisu, *Pressure of Kirkwood-Alder transition in monodisperse latex*, J. Chem. Phys. **67**, 2604 (1977).
- [82] B. J. Alder, W. G. Hoover, and D. A. Young, *Molecular dynamics. V. High-density equation of state and entropy for hard disks and spheres*, J. Chem. Phys. **49**, 3688 (1968).
- [83] S. Hachisu and K. Takano, *Pressure of disorder to order transition in monodisperse latex*, Adv. Colloid Interface Sci. **16**, 233 (1982).
- [84] R. Piazza, T. Bellini, and V. Degiorgio, *Equilibrium Sedimentation Profiles of Screened Charged Colloids: A Test of the Hard-Sphere Equation of State*, Phys. Rev. Lett. **71**, 4267 (1993).
- [85] M. A. Rutgers, J. H. Dunsmuir, J.-Z. Xue, W. B. Russel, and P. M. Chaikin, *Measurement of the hard-sphere equation of state using screened charged polystyrene colloids*, Phys. Rev. B **53**, 5043 (1996).
- [86] T. Biben, J. P. Hansen, and J. L. Barrat, *Density profiles of concentrated colloidal suspensions in sedimentation equilibrium*, J. Chem. Phys. **98**, 7330 (1993).
- [87] A. A. Brian, H. L. Frisch, and L. S. Lerman, *Thermodynamics and equilibrium sedimentation analysis of the close approach of DNA molecules and a molecular ordering transition*, Biopolymers **20**, 1305 (1981).
- [88] H. H. Wensink and H. N. W. Lekkerkerker, *Sedimentation and multi-phase equilibria in mixtures of platelets and ideal polymer*, Europhys. Lett. **66**, 125 (2004).
- [89] M. A. Bates, *Influence of particle shape on the nematic-isotropic transition of colloidal platelet systems*, J. Chem. Phys. **111**, 1732 (1999).
- [90] J. Kerr, *A new relation between electricity and light: dielectrified media*

- birefringent*, Phil. Mag. **50**, 337 (1875).
- [91] J. Kerr, Rep. Brit. Assoc. Adv. Sci., 568 (1901).
- [92] Q. Majorana, *Sur la biréfringence magnétique*, C.R. Acad. Sci. **135**, 159 (1902).
- [93] Q. Majorana, *Sur le dichroïsme magnétique*, C.R. Acad. Sci. **135**, 235 (1902).
- [94] Q. Majorana, *Su due nuovi fenomeni magneto-ottici osservati normalmente alle linee di forza*, Rend. Accad. Lincei **11-1**, 374 (1902).
- [95] Q. Majorana, *Sul metodo e sulle sostanze da adoperarsi, per osservare la birifrangenza magnetica*, Rend. Accad. Lincei **11-1**, 463 (1902).
- [96] Q. Majorana, *Sulla birifrangenza magnetica e su altri fenomeni che l'accompagnano*, Rend. Accad. Lincei **11-1**, 531 (1902).
- [97] Q. Majorana, *Sulle rotazioni bimagnetiche del piano di polarizzazione della luce*, Rend. Accad. Lincei **11-2**, 90 (1902).
- [98] Q. Majorana, *Sulla rapidità con cui si manifesta la birifrangenza magnetica*, Rend. Accad. Lincei **11-2**, 139 (1902).
- [99] A. Cotton and H. Mouton, *Sur le phénomène de Majorana*, C.R. Acad. Sci. **141**, 317 (1905).
- [100] A. Cotton and H. Mouton, *Sur la biréfringence magnétique. Nouveaux liquides actifs*, C.R. Acad. Sci. **141**, 349 (1905).
- [101] A. Cotton and H. Mouton, *Nouvelles propriétés magnéto-optiques des solutions colloïdales d'hydroxyde de fer*, C.R. Acad. Sci. **142**, 203 (1906).
- [102] A. Cotton and H. Mouton, *Sur les propriétés Magnéto-Optiques des Colloïdes et des Liqueurs Hétérogènes*, Ann. de Chim. et de Phys. **11**, 145 (1907).
- [103] A. Cotton and H. Mouton, *Sur les propriétés Magnéto-Optiques des Colloïdes et des Liqueurs Hétérogènes - Deuxième Partie*, Ann. de Chim. et de Phys. **11**, 289 (1907).
- [104] A. Cotton and H. Mouton, *Nouvelle propriété optique (biréfringence magnétique) de certains liquides organiques non colloïdaux*, C.R. Acad. Sci. **145**, 229 (1907).
- [105] B. J. Lemaire, P. Davidson, J. Ferré, J. P. Jamet, D. Petermann, P. Panine, I. Dozov, and J. P. Jolivet, *Physical properties of aqueous suspensions of goethite (α -FeOOH) nanorods, Part I: In the isotropic phase*, Eur. Phys. J. E **13**, 291 (2004).
- [106] B. J. Lemaire, P. Davidson, D. Petermann, P. Panine, I. Dozov, D. Stoenescu, and J. P. Jolivet, *Physical properties of aqueous suspensions of goethite (α -FeOOH) nanorods, Part II: In the nematic phase*, Eur. Phys. J. E **13**, 309 (2004).
- [107] J. Sugiyama, H. Chanzy, and G. Maret, *Orientation of cellulose microcrystals by strong magnetic fields*, Macromolecules **25**, 4232 (1992).
- [108] S. Fraden, G. Maret, D. L. D. Caspar, and R. B. Meyer, *Isotropic-nematic phase transition and angular correlations in isotropic suspensions of tobacco mosaic virus*, Phys. Rev. Lett. **63**, 2068 (1989).
- [109] S. Fraden, G. Maret, and D. L. D. Caspar, *Angular correlations and the isotropic-nematic phase transition in suspensions of tobacco mosaic virus*, Phys. Rev. E **48**, 2816 (1993).
- [110] H. Nakamura and K. Okano, *Pretransitional Phenomena in the Isotropic Phase of a Lyotropic Liquid Crystal of Bacterial Virus fd*, Phys. Rev. Lett. **50**, 186 (1983).
- [111] J. Tang and S. Fraden, *Magnetic-field-induced isotropic-nematic phase transition in a colloidal suspension*, Phys. Rev. Lett. **71**, 3509 (1993).
- [112] C. Martin, H. Kramer, C. Johnner, B. Weyerich, J. Biegel, R. Deike, M. Hagenbüchle, and R. Weber, *Electric and Magnetic Field Studies on Rodlike fd-Virus Suspensions*, Macromolecules **28**, 3175 (1995).
- [113] J. Torbet and G. Maret, *High-field magnetic birefringence study of the structure of rodlike phages Pfl and fd in solution*, Biopolymers **20**, 2657 (1981).

References

- [114] N. E. Geacintov, F. van Nostrand, M. Pope, and J. B. Tinkel, *Magnetic field effect on the chlorophyll fluorescence in Chlorella*, *Biochim. Biophys. Acta* **226**, 486 (1971).
- [115] J. P. Straley, *The Gas of Long Rods as a Model for Lyotropic Liquid Crystals*, *Mol. Cryst. Liq. Cryst.* **22**, 333 (1973).
- [116] L. D. Landau and E. M. Lifshitz, *The Classical Theory of Fields* (Butterworth-Heinemann, Oxford, 1975).
- [117] A. Guinier and G. Fournet, *Small Angle Scattering of X-rays* (Wiley, New York, 1955).
- [118] B. J. Lemaire, P. Panine, J. C. P. Gabriel, and P. Davidson, *The measurement by SAXS of the nematic order parameter of laponite gels*, *Europhys. Lett.* **59**, 55 (2002).
- [119] P. G. de Gennes, *The Physics of Liquid Crystals* (Clarendon Press, Oxford, 1974).
- [120] J. C. P. Gabriel and P. Davidson, *New Trends in Colloidal Liquid Crystals Based on Mineral Moieties*, *Adv. Mater.* **12**, 9 (2000).
- [121] J. C. P. Gabriel and P. Davidson, *Mineral Liquid Crystals from Self-Assembly of Anisotropic Nanosystems*, *Top. Curr. Chem.* **226**, 119 (2003).
- [122] K. Muta, H. Takezoe, A. Fukuda, and E. Kuze, *Cotton-Mouton effect of alkyl- and alkoxy-cyanobiphenyls in isotropic phase*, *Jpn. J. Appl. Phys.* **18**, 2073 (1979).
- [123] T. W. Stinson and J. D. Litster, *Pretransitional Phenomena in the Isotropic Phase of a Nematic Liquid Crystal*, *Phys. Rev. Lett.* **25**, 503 (1970).
- [124] G. Maret, M. v. Schickfus, A. Mayer, and K. Dransfeld, *Orientation of Nucleic Acids in High Magnetic Fields*, *Phys. Rev. Lett.* **35**, 397 (1975).
- [125] P. Photinos, C. Rosenblatt, T. M. Schuster, and A. Saupe, *Magnetic birefringence study of isotropic suspensions of tobacco mosaic virus*, *J. Chem. Phys.* **87**, 6740 (1987).
- [126] W. L. Bragg and A. B. Pippard, *The From Birefringence of Macromolecules*, *Acta Cryst.* **6**, 865 (1953).
- [127] "Physical and Optical Properties of Minerals", in *CRC Handbook of Chemistry and Physics, Internet Version 2005*, David R. Lide, ed., <<http://www.hbcpnetbase.com>>, CRC Press, Boca Raton, FL, 2004.
- [128] J. Zadoc-Kahn, *Biréfringence magnétique du para-azoxyanisole à des températures supérieures au point de disparition de l'état mésomorphe*, *C.R. Acad. Sci.* **190**, 672 (1930).
- [129] J. Zadoc-Kahn Eisenmann, *Sur les propriétés magnéto-optiques et électro-optiques du para-azoxyanisole*, *Ann. Phys. (Paris)* **6**, 455 (1936).
- [130] P. G. de Gennes, *Phenomenology of short-range-order effects in the isotropic phase of nematic materials*, *Phys. Lett. A* **30**, 454 (1969).
- [131] G. K. L. Wong and Y. R. Shen, *Optical-Field-Induced Ordering in the Isotropic Phase of a Nematic Liquid Crystal*, *Phys. Rev. Lett.* **30**, 895 (1972).
- [132] S. Neveu-Prin, F. A. Tourinho, J.-C. Bacri, and R. Perzynski, *Magnetic birefringence of cobalt ferrite ferrofluids*, *Colloids Surf. A* **80**, 1 (1993).
- [133] J. Ferré and G. A. Gehring, *Linear optical birefringence of magnetic crystals*, *Rep. Prog. Phys.* **47**, 513 (1984).
- [134] M. Surma and M. Cizek, *Magneto-optical and light scattering effects in liquid binary solutions*, *Physica B* **228**, 295 (1996).
- [135] F. D. Bloss, *An introduction to the methods of optical crystallography* (Holt, Rinehart and Winston, New York, 1961).
- [136] J. A. Osborn, *Demagnetizing Factors of the General Ellipsoid*, *Phys. Rev.* **67**, 351 (1945).
- [137] X. Commeinhes, P. Davidson, C. Bourgaux, and J. Livage, *Orientation of Liquid-Crystalline Suspensions of Vanadium Pentoxide Ribbons by a Magnetic Field*, *Advanced Materials* **9**, 900 (1997).
- [138] D. L. D. Caspar, *Adv. Protein Chem.* **18**, 37 (1963).

- [139] S. Bhattacharjee, M. J. Glucksman, and L. Makowski, *Structural polymorphism correlated to surface charge in filamentous bacteriophages*, *Biophys. J.* **61**, 725 (1992).
- [140] Z. Dogic and S. Fraden, *Cholesteric Phase in Virus Suspensions*, *Langmuir* **16**, 7820 (2000).
- [141] G. Maret and K. Dransfeld, in *Strong and Ultrastrong Magnetic Fields and Their Applications*, edited by F. Herlach (Springer-Verlag, Berlin, 1985), Vol. 57.
- [142] A. R. Khokhlov and A. N. Semenov, *Influence of External Field on the Liquid-Crystalline Ordering in Solutions of Stiff-Chain Macromolecules*, *Macromolecules* **15**, 1272 (1982).
- [143] S. Varga, G. Jackson, and I. Szalai, *External field induced paranematic-nematic phase transitions in rod-like systems*, *Mol. Phys.* **93**, 377 (1998).
- [144] S. Varga, G. Kronome, and I. Szalai, *External field induced tricritical phenomenon in the isotropic-nematic phase transition of hard non-spherical particle systems*, *Mol. Phys.* **98**, 911 (2000).
- [145] J. D. Parsons, *Nematic ordering in a system of rods*, *Phys. Rev. A* **19**, 1225 (1979).
- [146] S. D. Lee, *A numerical investigation of nematic ordering based on a simple hard-rod model*, *J. Chem. Phys.* **87**, 4972 (1987).
- [147] S. D. Lee, *The Onsager-type theory for nematic ordering of finite-length hard ellipsoids*, *J. Chem. Phys.* **89**, 7036 (1988).
- [148] H. H. Wensink, *Liquid crystal phase behaviour of colloidal mixtures*, PhD thesis, Utrecht University, Utrecht, The Netherlands (2004).
- [149] B. J. Lemaire, (2004).
- [150] D. van der Beek, T. Schilling, and H. N. W. Lekkerkerker, *Gravity-induced liquid crystal phase transitions of colloidal platelets*, *J. Chem. Phys.* **121** (2004).
- [151] A. J. Hurd, S. Fraden, F. Lonberg, and R. B. Meyer, *Field-induced transient periodic structures in nematic liquid crystals: the splay Fréedericksz transition*, *J. Phys. (Paris)* **46**, 905 (1985).
- [152] Z. Dogic, J. Zhang, A. W. C. Lau, H. Aranda-Espinoza, P. Dalhaimer, D. E. Discher, P. A. Janmey, R. D. Kamien, T. C. Lubensky, and A. G. Yodh, *Elongation and Fluctuations of Semiflexible Polymers in a Nematic Solvent*, *Phys. Rev. Lett.* **92**, 125503 (2004).
- [153] Z. Dogic, J. Zhang, A. W. C. Lau, H. Aranda-Espinoza, P. Dalhaimer, D. E. Discher, P. A. Janmey, R. D. Kamien, T. C. Lubensky, and A. G. Yodh, *Erratum: Elongation and Fluctuations of Semiflexible Polymers in a Nematic Solvent*, *Physical Review Letters* **93**, 219902 (2004).
- [154] F. Lonberg and R. Meyer, *New Ground State for the Splay-Fréedericksz Transition in a Polymer Nematic Liquid Crystal*, *Phys. Rev. Lett.* **55**, 718 (1985).
- [155] E. Guyon, R. Meyer, and J. Salan, *Domain Structure in the Nematic Freedericksz Transition*, *Mol. Cryst. Liq. Cryst.* **54**, 261 (1979).
- [156] C. R. Fincher, *Field-induced textures and elastic constants of nematic polymers*, *Macromolecules* **19**, 2431 (1986).
- [157] M. Grigutsch, N. Klöpper, H. Schmiedel, and R. Stannarius, *Transient structures in the twist Fréedericksz transition of low-molecular-weight nematic liquid crystals*, *Phys. Rev. E* **49**, 5452 (1994).
- [158] M. R. Kuzma, *Nonequilibrium Periodic Structures Induced by Rotating and Static Fields in a Lyotropic Nematic Liquid Crystal*, *Phys. Rev. Lett.* **57**, 349 (1986).
- [159] S. Fraden and R. B. Meyer, *Comment on "Nonequilibrium Periodic Structures Induced by Rotating and Static Fields in a Lyotropic Nematic Liquid Crystal"*, *Phys. Rev. Lett.* **57**, 3122 (1986).
- [160] J. P. Straley, *Frank Elastic Constants of the Hard-Rod Liquid Crystal*, *Phys. Rev. A* **8**, 2181 (1973).
- [161] S. D. Lee and R. B. Meyer, *Computations of the phase equilibrium, elastic constants, and viscosities of a hard-rod nematic liquid crystal*, *J. Chem. Phys.* **84**, 3443 (1986).
- [162] G. J. Vroege and T. Odijk, *Elastic moduli of a nematic liquid-crystalline solution of polyelectrolytes*, *Journal of Chemical Physics* **87**, 4223 (1987).

References

- [163] F. Lonberg, S. Fraden, A. J. Hurd, and R. Meyer, *Field-Induced Transient Periodic Structures in Nematic Liquid Crystals: The Twist-Fréedericksz Transition*, Phys. Rev. Lett. **52**, 1903 (1984).
- [164] G. Srajer, S. Fraden, and R. B. Meyer, *Field-induced nonequilibrium periodic structures in nematic liquid crystals: Nonlinear study of the twist Frederiks transition*, Phys. Rev. A **39**, 4828 (1989).
- [165] H. C. H. Darley and G. R. Gray, *Compostion and Properties of Drilling and Completion Fluids* (Gulf Publishing Company, Houston, Texas, 1988).
- [166] J. C. P. Gabriel, C. Sanchez, and P. Davidson, *Observation of Nematic Liquid-Crystal Textures in Aqueous Gels of Smectite Clays*, J. Phys. Chem. **100**, 11139 (1996).
- [167] L. J. Michot, I. Bihannic, K. Porsch, S. Maddi, C. Baravian, J. Mougel, and P. Levitz, *Phase Diagrams of Wyoming Na-Montmorillonite Clay. Influence of Particle Anisotropy*, Langmuir **20**, 10829 (2004).
- [168] A. Mouchid, A. Delville, J. Lambard, E. Lécolier, and P. Levitz, *Phase Diagram of Colloidal Dispersions of Anisotropic Charged Particles: Equilibrium Properties, Structure, and Rheology of Laponite Suspensions*, Langmuir **11**, 1942 (1995).
- [169] A. Mouchid, E. Lécolier, H. Van Damme, and P. Levitz, *On Viscoelastic, Birefringent, and Swelling Properties of Laponite Clay Suspensions: Revisited Phase Diagram*, Langmuir **14**, 4718 (1998).
- [170] J. O. Fossum, *Physical phenomena in clays*, Physica A **270**, 270 (1999).
- [171] E. Dimasi, J. O. Fossum, T. Gog, and C. Venkataraman, *Orientalional order in gravity dispersed clay colloids: A synchrotron x-ray scattering study of Na fluorohectorite suspensions*, Physical Review E **64**, 061704 (2001).
- [172] A. B. D. Brown, C. Ferrero, T. Narayanan, and A. R. Rennie, *Phase separation and structure in a concentrated colloidal dispersion of uniform plates*, Eur. Phys. J. B **11**, 481 (1999).
- [173] M. Sullivan, K. Zhao, C. Harrison, R. H. Austin, M. Megens, A. Hollingsworth, W. B. Russel, Z. Cheng, T. Mason, and P. M. Chaikin, *Control of colloids with gravity, temperature gradients, and electric fields*, J. Phys. Cond. Matter **15**, S11 (2003).
- [174] V. A. Baulin and A. R. Khokhlov, *Nematic ordering of rigid rods in a gravitational field*, Phys. Rev. E **60**, 2973 (1999).
- [175] J. D. F. Ramsay, A. R. Daish, and C. J. Wright, *Structure and stability of concentrated boehmite sols*, J. Chem. Soc., Faraday Discuss. **65**, 65 (1978).
- [176] J. M. Drouin, T. Chopin, P. Nortier, and H. van Damme, *Rheology and structure of peptized boehmite pastes*, J. Colloid Interface Sci. **125**, 314 (1987).
- [177] J. K. Beattie, J. K. Cleaver, and T. D. Waite, *Anomalous aggregation behaviour of aluminium oxyhydroxides*, Colloids Surf. A **111**, 131 (1996).
- [178] J. Hernandez, *Thèse de Doctorat de l'Université Pierre et Marie Curie*, PhD thesis, Université Pierre et Marie Curie, Paris, France (1998).
- [179] P. Levitz, E. Lécolier, A. Mouchid, A. Delville, and S. Lyonnard, *Liquid-solid transition of Laponite suspensions at very low ionic strength: Long range electrostatic stabilisation of anisotropic colloids*, Europhys. Lett. **49**, 672 (2000).
- [180] F. M. van der Kooij, D. van der Beek, and H. N. W. Lekkerkerker, *Isotropic - Nematic Phase Separation in Suspensions of Polydisperse Colloidal Platelets*, J. Phys. Chem. B **105**, 1696 (2001).
- [181] D. G. Rowan and J. P. Hansen, *Salt-Induced Ordering in Lamellar Colloids*, Langmuir **18**, 2063 (2002).
- [182] A. Stroobants, H. N. W. Lekkerkerker, and T. Odijk, *Effect of Electrostatic Interaction on the Liquid Crystal Phase Transition in Solutions of Rodlike Polyelectrolytes*, Macromolecules **19**, 2232 (1986).
- [183] K. E. Davis, W. B. Russel, and W. J. Glantschnig, *Disorder-to-Order Transition in Settling Suspensions of Colloidal Silica: X-ray Measurements*, Science **245**, 507 (1989).

References

- [184] B. J. Ackerson, S. E. Paulin, and B. Johnson, *Crystallization by settling in suspensions of hard spheres*, Phys. Rev. E **59**, 6903 (1999).
- [185] T. Svedberg and K. O. Pedersen, *Die Ultracentrifuge* (Theodor Steinkopff, Dresden, 1940).
- [186] J. P. Hoogenboom, D. Derks, P. Vergeer, and A. van Blaaderen, *Stacking faults in colloidal crystals grown by sedimentation*, J. Chem. Phys. **117**, 11320 (2002).
- [187] J. P. Hoogenboom, P. Vergeer, and A. van Blaaderen, *A real-space analysis of colloidal crystallization in a gravitational field at a flat bottom wall*, J. Chem. Phys. **119**, 3371 (2003).
- [188] R. C. Williams and K. M. Smith, *A crystallizable insect virus*, Nature **179**, 119 (1957).
- [189] A. Klug, R. E. Franklin, and S. P. F. Humphreys-Owen, *The crystal structure of tipula iridescent virus as determined by Bragg reflection of visible light*, Biochim. Biophys. Acta **32**, 203 (1959).
- [190] H. Maeda and Y. Maeda, *Measurement of Density Distributions for Colloidal β -FeOOH Rods in Suspensions Exhibiting Phase Separation: The Role of Long-range Forces in Smectic Ordering*, J. Chem. Phys. **121**, 12655 (2004).
- [191] J. E. G. J. Wijnhoven, *in preparation*.
- [192] S. R. Williams and A. P. Philipse, *personal communication*.

References

Summary

In this thesis, the liquid crystal phase behaviour of colloidal platelets in external fields was studied. As stated in the introduction to this thesis, the equilibrium phase behaviour of colloidal platelets in the absence of a field is by now reasonably well understood, enabling a study of the phase behaviour of such particles in external fields. We have specifically focussed on morphological, gravitational, magnetic and centrifugal fields.

Part I of this thesis gives a closer look on the liquid crystal phases of the sterically stabilised colloidal gibbsite platelets. It has been observed, both in computer simulation and experiment, that suspensions of plates display the liquid crystalline nematic and columnar phases. In Chapter 2, we make use of a morphological field (the sample walls) to create large oriented domains of the columnar phase with unique orientation. The addition of non-adsorbing polymer to the suspensions appears to aid the formation of such large domains. The domains were studied using small-angle X-ray scattering (SAXS), providing unambiguous evidence for the hexagonal nature of the columnar phase, evidence that had been lacking hitherto.

Chapter 3 focuses on the effect of the earth's gravitational field on the suspension of sterically stabilised gibbsite platelets. We observe that an initially isotropic-nematic sample develops a third, columnar phase at the bottom on prolonged standing. This phenomenon is described using a simple osmotic compression model. We performed Monte Carlo simulations of cut spheres with an aspect ratio of $L/D = 1/15$ and took data from the literature to supply the equations of state required for the model. We find that the three-phase equilibrium is quite well described by our model, be it for an aspect ratio that is somewhat lower than the experimental one. In conclusion, the gravitational field allows sampling of a large range of concentrations in one sample, displaying all possible phases at one time.

In Part II, we have subjected the suspension of the sterically stabilised colloidal gibbsite platelets to external magnetic fields. A first and important observation is that we find significant magnetic-field-induced orientational order in the isotropic phase. First, in Chapter 4, we use small-angle X-ray scattering (SAXS) to measure this field-induced order. In order to analyse our SAXS data, we derive a simple model that relates the scattered intensity of the isotropic phase to the orientational distribution function. Despite its approximations, it describes the observed SAXS patterns reasonably well and it yields a lower bound of the diamagnetic susceptibility anisotropy $|\Delta\chi|$. In Chapter 5, we measure the magnetic-field-induced birefringence of the isotropic phase. Again, we obtain a value of $|\Delta\chi|$, be it higher than in Chapter 4, giving us a range of the diamagnetic susceptibility anisotropy. From it, we take a likely value of $\Delta\chi$, which we subsequently use in the following two chapters.

Summary

Chapter 6 focuses on the isotropic-nematic phase behaviour of our suspension in a magnetic field. We observe a shift of the phase transition densities to lower values, which is described using a Clausius-Clapeyron type approach to the problem. Despite its simplicity, it allows one to estimate the slope of the isotropic branch of the binodal lines.

In Chapter 7, we study the competition between the wall- and magnetic-field-induced order in the nematic phase of our suspension, *i.e.*, the Frederiks transition. The nematic phase appears to have a strong tendency to homeotropic anchoring on the wall. This condition enabled us to induce the Frederiks transition reproducibly. From the uniform Frederiks transition, we determined the bend elastic constant of the nematic phase. In addition, we use a rotating magnetic field to induce non-equilibrium transient stripe patterns in the nematic phase. We measure the periodicity of the patterns as a function of the magnetic field strength and sample thickness and find qualitative agreement with theoretical predictions.

The last part of this thesis, Part III, is devoted to aqueous suspensions of gibbsite platelets. In Chapter 8, we first describe the synthesis of such dispersions. Then, we study the phase behaviour in the absence of an external field. For the first time since Langmuir in 1938, we find isotropic-nematic phase separation in a dispersion of charged plate-like particles. Furthermore, we observe the isotropic-columnar transition, depending on the ionic strength, which is understood on the basis of earlier computer simulations.

We subsequently apply a gravitational field on the suspension and find that the resulting three-phase (isotropic, nematic and columnar) equilibrium is well described by the same osmotic compression model that was developed in Chapter 3.

In the last chapter, Chapter 9, a centrifugal field of 900 G is applied to the aqueous gibbsite platelet dispersion. This appears to be less destructive than one would initially think: the columnar phase is still observed in such extremely strong fields. The order of the colour of the Bragg reflections of the columnar phase suggests size fractionation in the sediment, with the largest particles accumulating at the bottom of the phase. This is confirmed by SAXS measurements and real space imaging using transmission electron microscopy.

Samenvatting

In dit proefschrift wordt het vloeibaar kristallijn fasegedrag van colloïdale plaatjes in externe velden bestudeerd. Het (fase)gedrag van colloïdale plaatjes in afwezigheid van een veld wordt tegenwoordig goed begrepen, wat verdere studie naar de invloed van een extern veld op dit gedrag mogelijk maakt. We hebben met name gekeken naar het effect van morfologische, gravitationele, magnetische en centrifugaalvelden.

Deel I van het proefschrift gaat nog eens nader in op de vloeibaar kristallijne fasen, te weten de nematische en columnaire, die een suspensie van sterisch gestabiliseerde gibbsietplaatjes vertoont. In Hoofdstuk 2 wordt gebruik gemaakt van een morfologisch veld (de wanden van het monster) om grote en specifiek uitgerichte domeinen van de columnaire fase te maken. De toevoeging van niet-adsorberend polymeer blijkt de vorming van zulke grote domeinen te bevorderen. Vervolgens werden deze bestudeerd met kleine-hoek Röntgenverstrooiing (in het Engels afgekort tot SAXS), waaruit ontegenzeggelijk bleek dat wij hier met een hexagonale fase te maken hebben; bewijs dat tot op deze dag ontbrak.

Hoofdstuk 3 richt zich op het effect van het zwaartekrachtsveld van de aarde op eenzelfde suspensie. We nemen waar dat een initieel isotroop-nematisch monster na lange tijd een derde, columnaire fase vormt op de bodem van het monster. Dit fenomeen wordt goed beschreven door een osmotisch compressie-model dat wij hiervoor ontwikkelden. Verder werden er Monte Carlo computer simulaties gedaan aan afgeknotte bollen met een dikte-diameterverhouding van $L/D=1/15$, om hieruit de toestandsvergelijking te verkrijgen. Samen met twee andere toestandsvergelijkingen uit de literatuur werden deze gebruikt in ons model. Dit leidt tot de conclusie dat het drie-fasenevenwicht, zoals experimenteel gevonden, goed wordt beschreven door ons model, zij het voor een iets lagere dikte-diameterverhouding dan de experimentele. Het zwaartekrachtsveld geeft aanleiding tot een concentratiegradiënt in één enkel monster, waardoor alle mogelijke fasen op hetzelfde moment zichtbaar worden.

Deel II van dit proefschrift is gewijd aan de invloed van een magnetisch veld op de suspensie van sterisch gestabiliseerde gibbsietplaatjes. Een belangrijke waarneming is dat isotrope suspensies een significante oplijning vertonen onder invloed van het magnetisch veld. Dit verschijnsel wordt eerst in Hoofdstuk 4 bestudeerd met behulp van SAXS. Om onze data te analyseren hebben wij een eenvoudig model ontwikkeld dat de intensiteit van de verstrooide straling relateert aan de oriëntationele distributiefunctie. Ondanks de benaderingen in dit model beschrijft het de SAXS-patronen redelijk en levert het een ondergrens voor de waarde van de anisotropie van de diamagnetische susceptibiliteit, $|\Delta\chi|$.

In Hoofdstuk 5 wordt het verschijnsel van de magnetisch veld-geïnduceerde oplijning bestudeerd met dubbelbrekingsmetingen aan de isotrope fase. Opnieuw wordt een waarde voor $|\Delta\chi|$ gevonden, ook al is die nu beduidend hoger dan in Hoofdstuk 4. Samen

Samenvatting

resulteert dit in een betrouwbaarheidsinterval voor $\Delta\chi$, waaruit we een meest waarschijnlijke waarde nemen die wij in de twee volgende hoofdstukken gebruiken.

De gevoeligheid van de gibbsietplaatjes voor het magnetisch veld heeft invloed op het isotroop-nematisch fasegedrag; dit wordt in Hoofdstuk 6 bestudeerd. Wij vinden dat de isotroop-nematische faseovergang naar een lagere concentratie schuift als gevolg van het magnetisch veld. Met behulp van een Clausius-Clapeyron-achtige benadering kunnen wij dit beschrijven. Ondanks de eenvoud van deze benadering geeft het de helling van de isotrope tak van de binodaallijnen.

In Hoofdstuk 7 komt de competitie tussen de wand (een morfologisch veld) en het magnetisch veld aan bod. Dit wordt ook wel de Frederiksovergang genoemd. De nematische fase van het sterisch gestabiliseerde systeem van gibbsietplaatjes vertoont een sterke neiging om aan een wand homeotroop te verankeren. Dit stelt ons in staat om de Frederiksovergang op reproduceerbare wijze te induceren. Uit deze experimenten kunnen wij de grootte van de “buig”-elastische constante (in het Engels: bend elastic constant), K_3 , bepalen. Verder gebruiken wij een roterend magnetisch veld om een niet-evenwichtspatroon van strepen te genereren in de nematische fase. De golflengte van deze patronen is gemeten als functie van de dikte van het monster en de magnetische veldsterkte en komt kwalitatief overeen met theoretische voorspellingen.

In het laatste deel van het proefschrift, Deel III, worden waterige suspensies van (geladen) gibbsietplaatjes bestudeerd. Eerst wordt in Hoofdstuk 8 de synthese van zulke suspensies beschreven. Verder kijken wij naar het fasegedrag in afwezigheid van een extern veld. Voor het eerst sinds Irving Langmuir (in 1938) nemen wij de isotroop-nematische faseovergang waar in een suspensie van geladen plaatvormige colloïden. Ook wordt (afhankelijk van de zoutsterkte) de isotroop-columnaire overgang waargenomen, iets dat kan worden begrepen op basis van eerdere computer simulaties.

Vervolgens worden ook deze suspensies blootgesteld aan het aards zwaartekrachtsveld en vinden ook hier een drie-fasenevenwicht (met de isotrope, nematische en columnaire fase) dat goed beschreven kan worden met het osmotische compressiemodel dat wij in Hoofdstuk 3 uiteen hebben gezet.

In het laatste hoofdstuk, Hoofdstuk 9, worden de waterige suspensies aan een centrifugaalveld van 900 G onderworpen. Dit is minder destructief dan men in eerste instantie zou denken: de columnaire fase, met zijn karakteristieke Bragg-reflectiekleuren, wordt dan nog steeds waargenomen. De volgorde van de kleuren in de fase suggereert een groottefractionering van de gibbsietplaatjes, waarbij de grootste onderin zitten. Dit idee wordt bevestigd door metingen met SAXS en elektronenmicroscopie.

Colour versions of selected figures

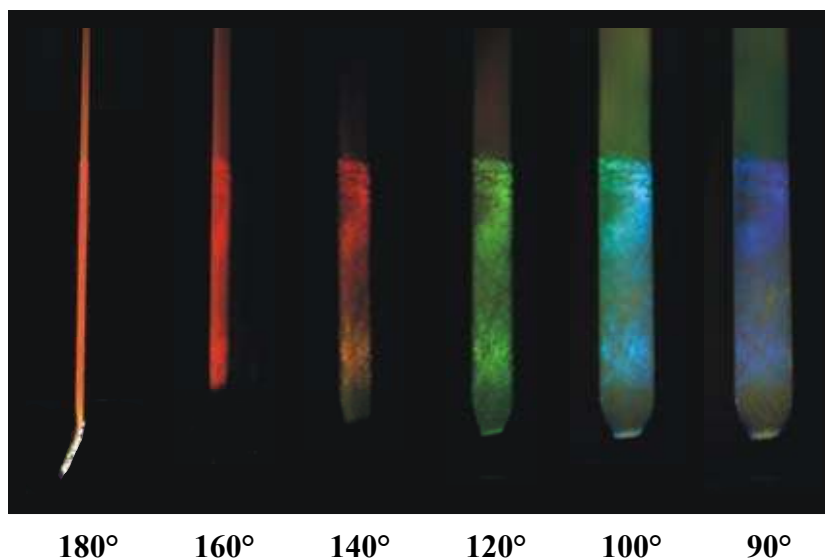


Figure 2.2 – Bragg reflections from the columnar phase of sample C. The upper part of the sample is a nematic phase in equilibrium with the columnar phase. The colour of the reflections (red through blue) varies with the incident Bragg angle 2Θ . The reflections already hint at the presence of a columnar structure and allow making an estimate of the inter-columnar spacing as $\langle d_{(100)} \rangle = 215 \pm 15$ nm, see Table 9.2. Close inspection of the nematic phase reveals a red colour (two most left photographs), indicative of the structure factor peak at about the same position as the $d_{(100)}$ -maximum in the columnar phase.

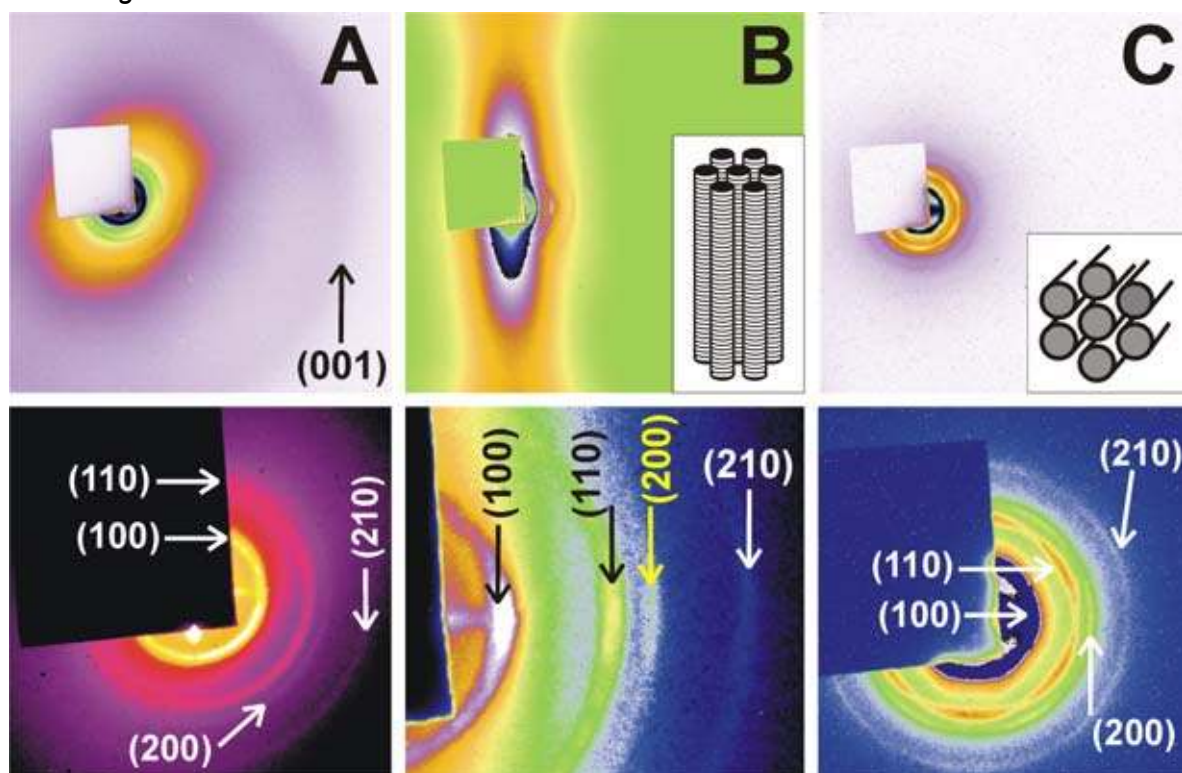


Figure 2.3 – SAXS patterns obtained in the columnar phase of samples A, B and C, along with the assigned Miller indices. The upper panels depict the entire SAXS patterns, while the lower panels present the magnified views of the small scattering angle regions near the beam-stop. Sample A yields ring-like diffraction features typical for diffraction from a powder. In contrast, samples B and C show strong predominant orientation of the columns, either along the vertical direction (in B) or along the X-ray beam (in C), as shown by the inserted sketches. The hexagonal pattern in C points to the presence of the hexagonal columnar phase.

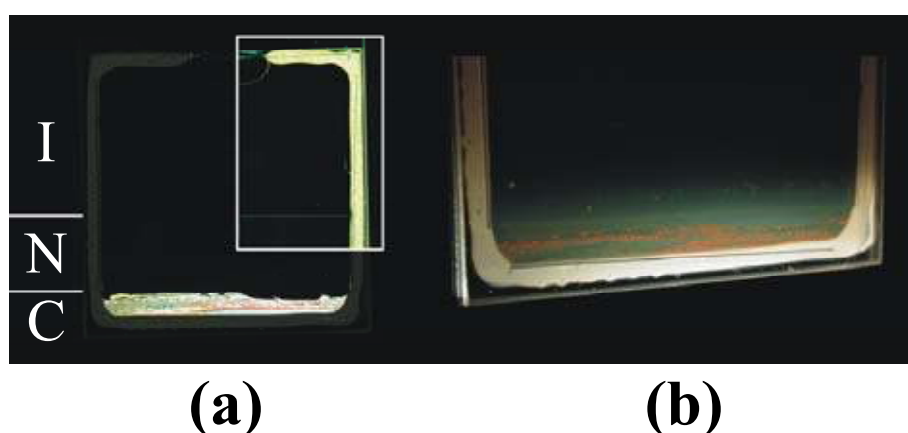


Figure 3.2 – The three-phase sedimentation equilibrium. Photograph (a) depicts the complete sample between crossed polarisers, where the upper right part is digitally enhanced to visualise the I-N interface. The columnar phase contains a dark region at the upper right of the phase, probably due to orientation of the platelets along the sample walls. Although not clearly visible, the N-C interface is horizontal and sharp. (b) shows the columnar phase illuminated with white light to capture the red Bragg reflections.

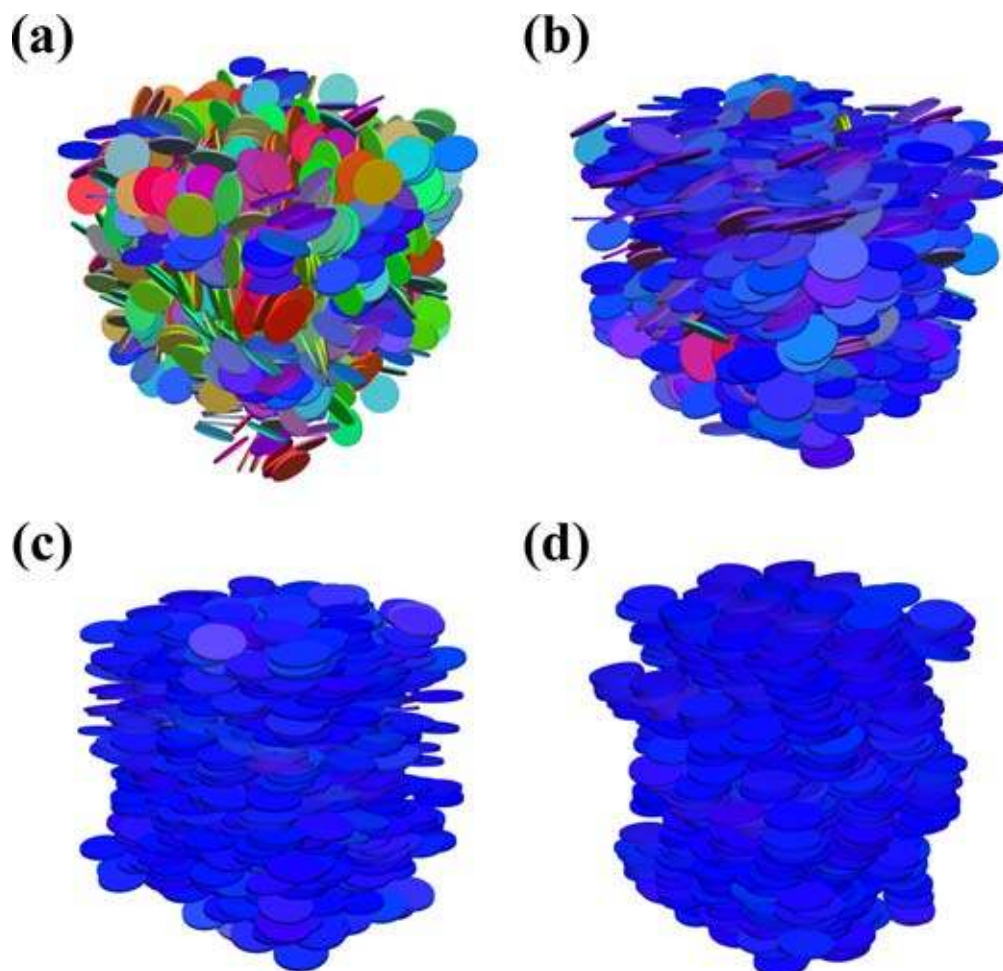


Figure 3.4 – Configuration snapshots from the MC computer simulations, illustrating the positional and orientational order close to the I-N and N-C phase transitions. Shading or colour is used to distinguish between different orientations of the platelets. Snapshots (a) and (b) display the isotropic ($c = 3.39$, $\tilde{\Gamma} = 20$) and nematic phase ($c = 4.62$, $\tilde{\Gamma} = 30$) just below and above the I-N transition, respectively. Clearly, the orientational order has increased, whereas (long range) positional order is still lacking. Snapshots (c) and (d) show the nematic and columnar phase, respectively, near the N-C transition (at state points $c = 7.49$, $\tilde{\Gamma} = 73$ and $c = 8.66$, $\tilde{\Gamma} = 82.5$, respectively). At the N-C transition, there is hardly any gain in orientational order, while the positional order becomes two-dimensional in the columnar phase.

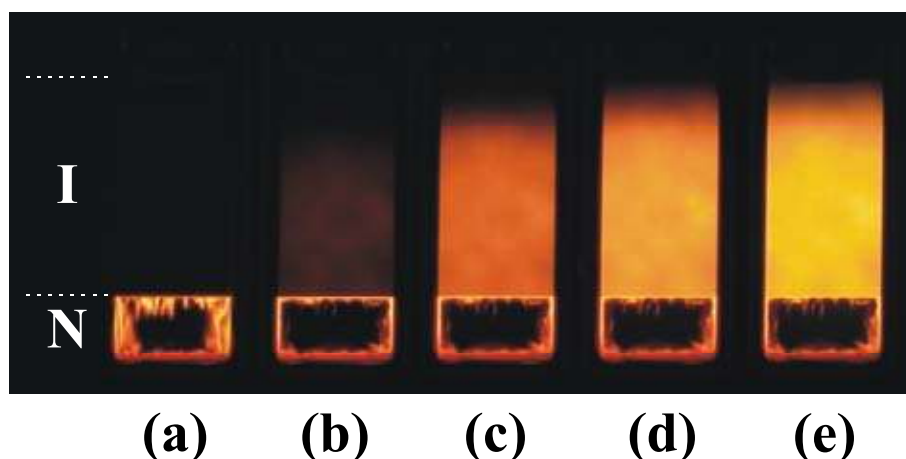


Figure 5.1 – Illustration of the magnetic-field-induced birefringence in the isotropic phase of the suspensions of sterically stabilised colloidal gibbsite platelets. An isotropic-nematic sample with path length $d = 2.00$ mm is placed between crossed polarisers in a horizontal magnetic field (a) 0, (b) 0.5, (c) 1, (d) 1.5, and (e) 2.0 T, generated using a Bruker BE25v Electromagnet. The sample is observed between crossed polarisers, making angles of -45° and 45° with the vertical direction. As can be seen quite clearly, the birefringence in the isotropic phase increases with increasing magnetic field. The black patch in the nematic phase, which increases in size with the field strength, is caused by so-called homeotropic anchoring of the platelets on the front and back walls of the cell. This phenomenon is studied in Chapter 7. The birefringence gradient observed at the top of the sample is due to sedimentation of the particles.

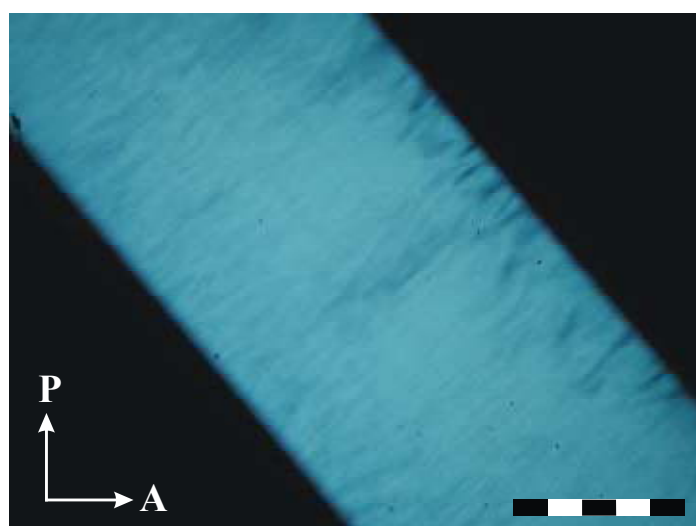


Figure 5.5 – Aligned nematic sample used in the determination of Δn_{sat} . At an angle of 0° with the polariser the sample appeared completely black. The scale bar denotes 1 mm.

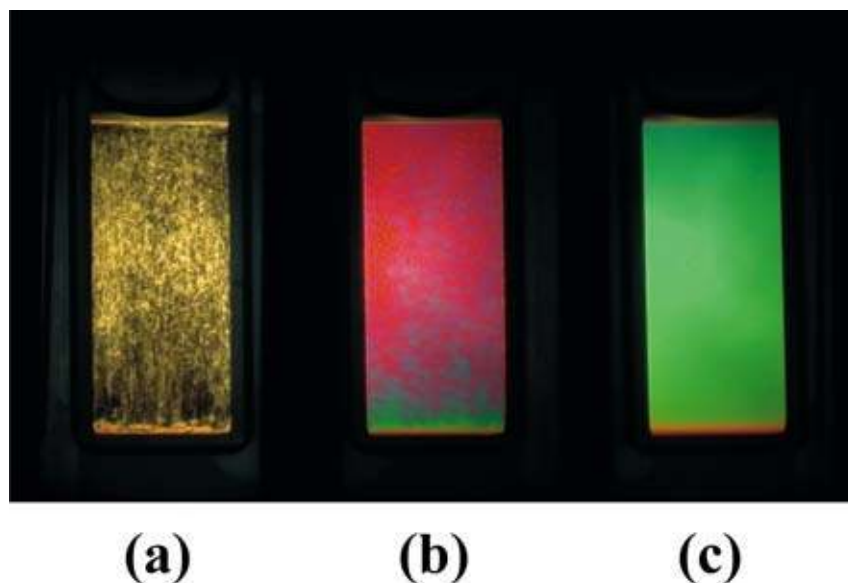


Figure 5.6 – Isotropic-nematic sample in a magnetic field, rotated around its vertical axis at an average rate of 6 revolutions per minute (a) just before starting rotation and after rotating for (b) 1 and (c) 2 minutes. The magnetic field was directed horizontally, $B = 1.4$ T, the polarisers made an angle of -45° and 45° with the vertical direction. Due to this specific geometry, a (uniaxial) nematic phase is prepared with its director along the vertical rotation axis. Using an interference colour chart [132], we find that the green interference colour finally emerging is a “second-order” green, with a retardation $\Delta = 800 \pm 40$ nm. In this specific sample, due to the magnetic field, the amount of nematic phase had increased from 80% to 97%. This phenomenon is described in more detail in Chapter 6. Furthermore, we note that we have in fact induced the Frederiks transition in the sample, *i.e.*, a reorientation of the nematic director field due to a magnetic field.

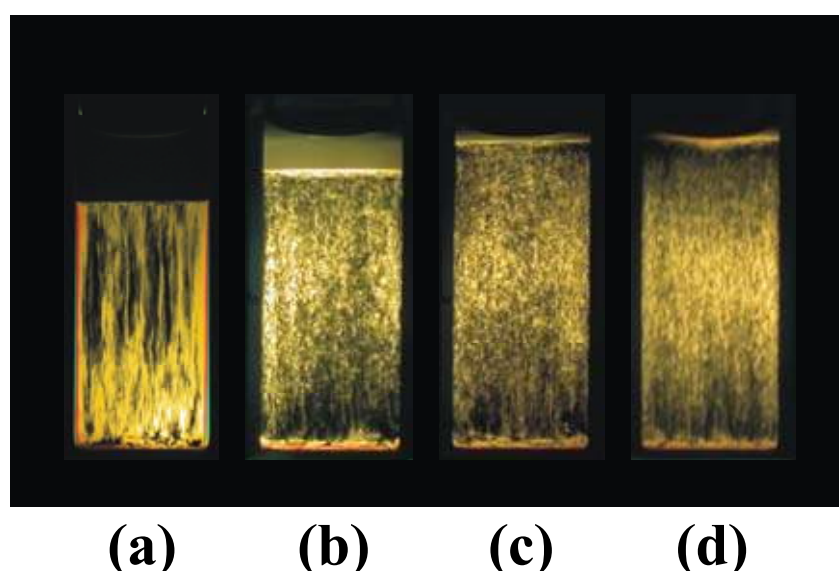


Figure 6.2 – A biphasic sample of a different batch of sterically stabilised colloidal gibbsite platelets photographed between crossed polarisers at increasing magnetic field strength. The amount of nematic phase increases with the field, at the cost of the isotropic (or paranematic) phase. The sample is shown at $B^2 =$ (a) 0, (b) 1, (c) 2, and (d) 3 T², respectively.

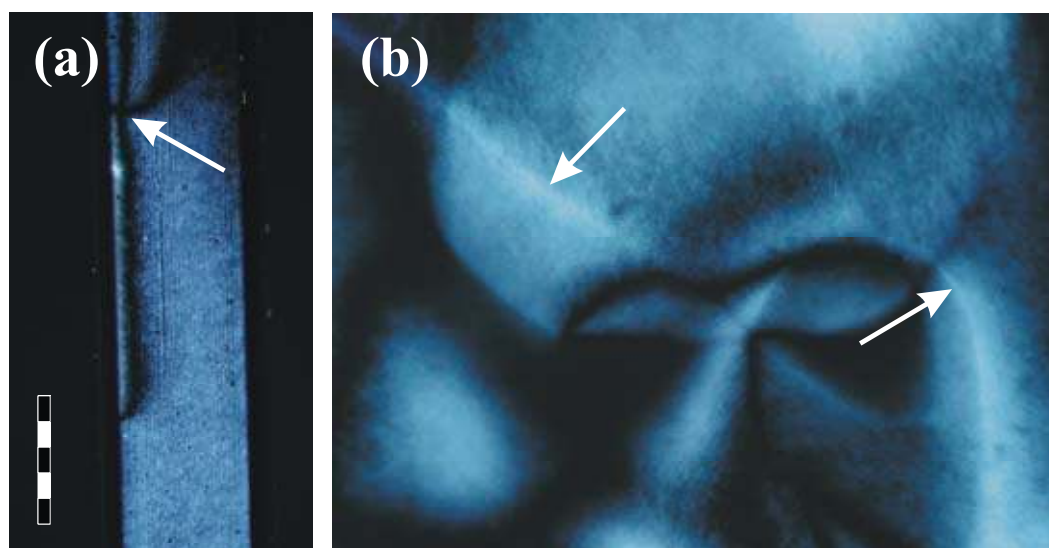


Figure 7.1 – The nematic phase of sterically stabilised colloidal gibbsite platelets shows defects typical for a nematic phase, like the (a) four-brush defect and (b) disclination lines indicated by the white arrows. The scale bar denotes 500 μm and pertains to both micrographs.

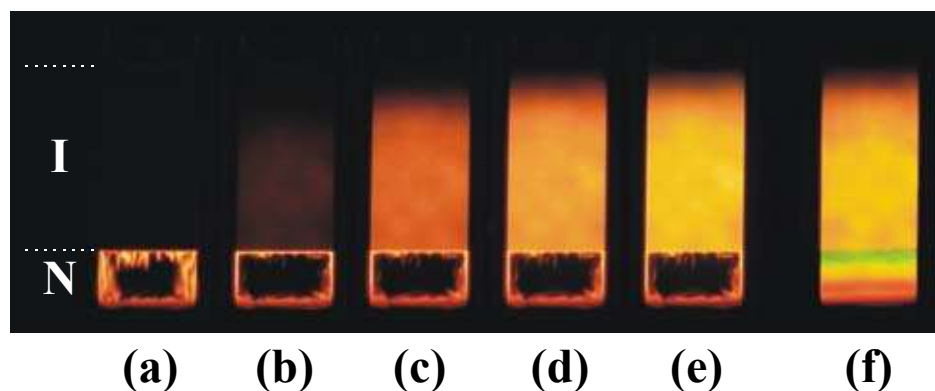


Figure 7.2 – An isotropic-nematic sample of the sterically stabilised colloidal platelets at coexistence between crossed polarisers (that make angles of -45° and 45° with the vertical direction). This demonstrates the wall-imposed director field in the nematic phase and the Frederiks transition. (a) - (e) have been shown earlier in Fig. 5.1 and depict the sample at increasing field strength of 0 to 2.0 T. (f) depicts the sample after rotating it in the horizontal magnetic field of 2.0 T, inducing a reorientation of the nematic director field, *i.e.*, the Frederiks transition. In (a) - (e), the nematic phase contains a black region, seemingly indicating lack of orientational order. However, due to the imposed director orientation by the walls, the sample has become homeotropic in the centre. Clearly, the director field is dominated by the wall that is closest, as indicated by the birefringence at the sides of the phase. At increasing magnetic field, the black patch extends as the horizontal magnetic field stabilises homeotropic alignment.

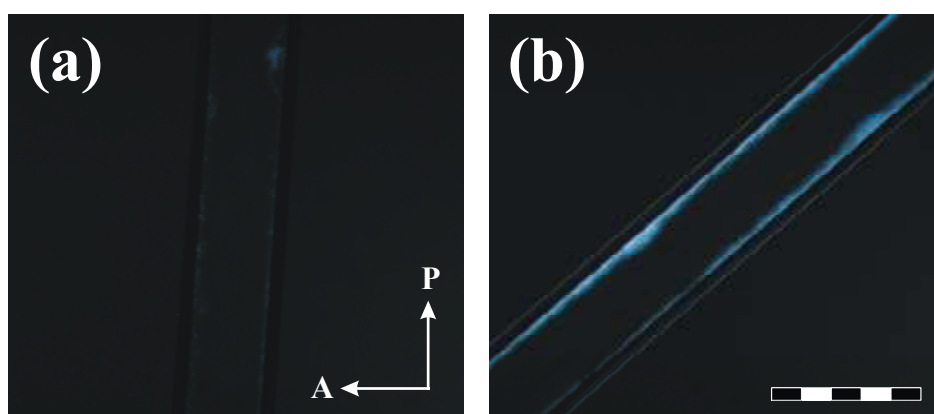


Figure 7.4 – The onset of the uniform Frederiks transition, in a sample with $d = 50 \mu\text{m}$ at $B = 91 \text{ mT}$. The sample is shown at (a) 0° and (b) 45° with respect to the polariser-orientation, as is indicated by the arrows; the scale bar denotes 1 mm . The first signs of birefringence are visible at the edges of the capillary, where they aid the reorientation.

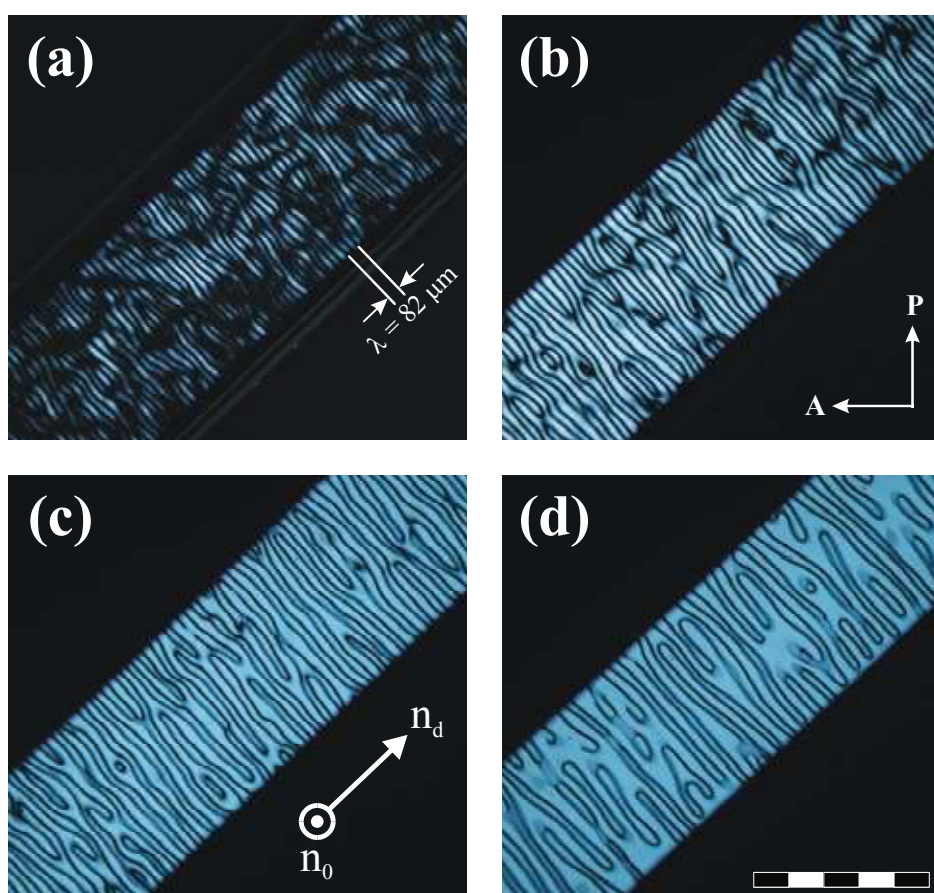


Figure 7.6 – Evolution of the non-uniform Frederiks transition in a sample with thickness $d = 100 \mu\text{m}$ at $B = 0.56 \text{ T}$, rotated around the capillary's long axis at 0.17 Hz , observed at (a) $t = 5 \text{ s}$, (b) 86 s , (c) 200 s , and (d) 554 s . The sample makes an angle of 45° with the polarisers; the scale bar denotes 1 mm . The wavelength of the periodic pattern increases from $82 \mu\text{m}$ at the start to a saturation value of $104 \mu\text{m}$. The evolution of the wavelength in time is depicted in Fig. 7.7.



Figure 7.9 – Early stage of the rotation of a nematic phase in a horizontal magnetic field, used in Chapter 5 to determine Δn_{sat} . Sample thickness $d = 2.00$ mm, $B = 1.4$ T, the scale bar denotes 1 cm. The temporal periodicity observed in this sample hints at the same type of transient pattern as observed in the much thinner samples in this study. However, the initial alignment of this sample was not homeotropic, hence, we do not draw quantitative conclusions from this observation.

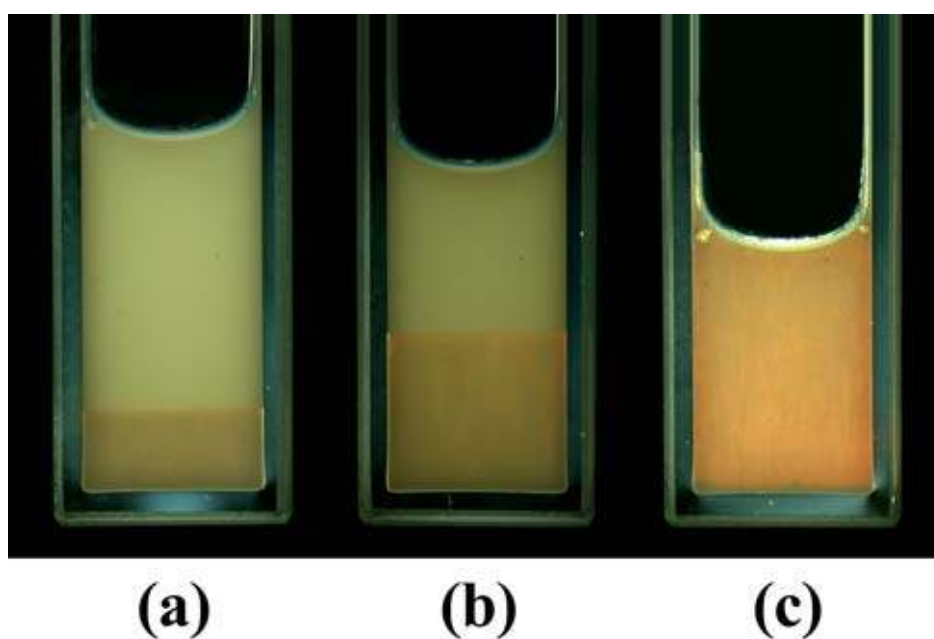


Figure 8.2 – The I-N phase transition observed between crossed polarisers. The ionic strength in these samples is 10 mM and the gibbsite concentration (a) 328 g/l, (b) 356 g/l, and (c) 464 g/l. Sample (c) is well into the nematic phase, in contrast with our earlier study [26] where gelation impeded the formation of a completely nematic phase.

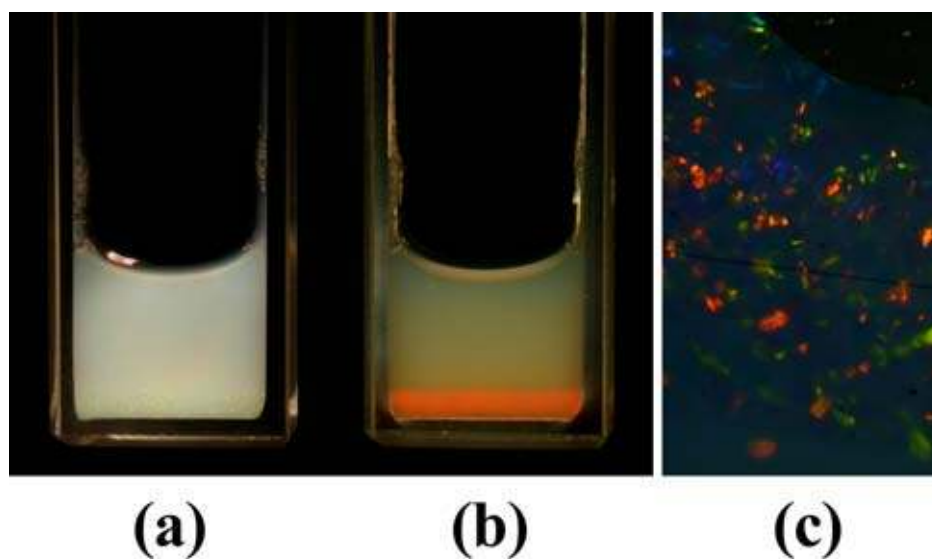


Figure 8.3 – Phase separated sample in I-C equilibrium, (a) illuminated by white light and (b) between crossed polarisers. (c) depicts a close-up of Bragg reflections in another columnar sample. The Bragg reflections stem from the two-dimensional hexagonal lattice of columns of platelets, with a lattice spacing of about 200 nm.

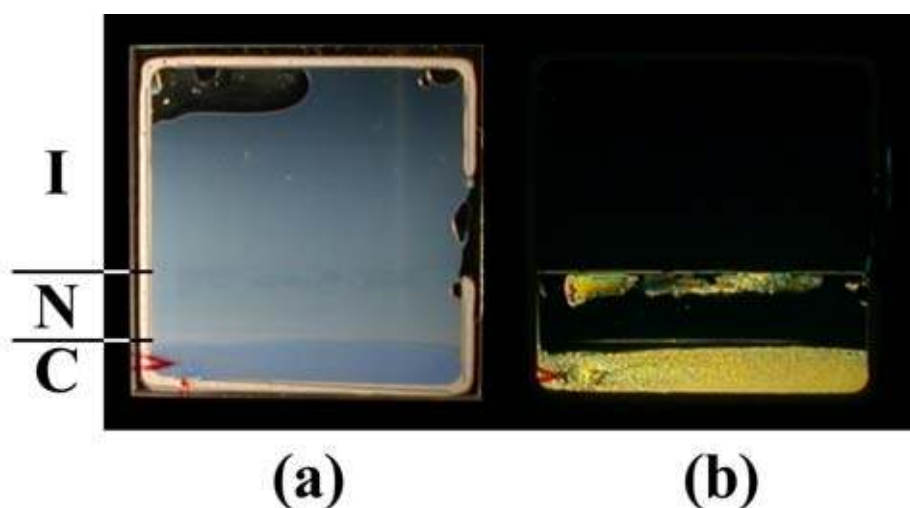


Figure 8.5 – An initially biphasic (I-N) sample that developed a third phase (C) over a timescale of six months. (a) depicts the sample in reflection with white light, and (b) in transmission between crossed polarisers. Again, Bragg reflections can be observed in the columnar phase; see (a). In (b), the major part of the nematic phase appears dark, this is because of the alignment of the platelets along the wall (homeotropic alignment).

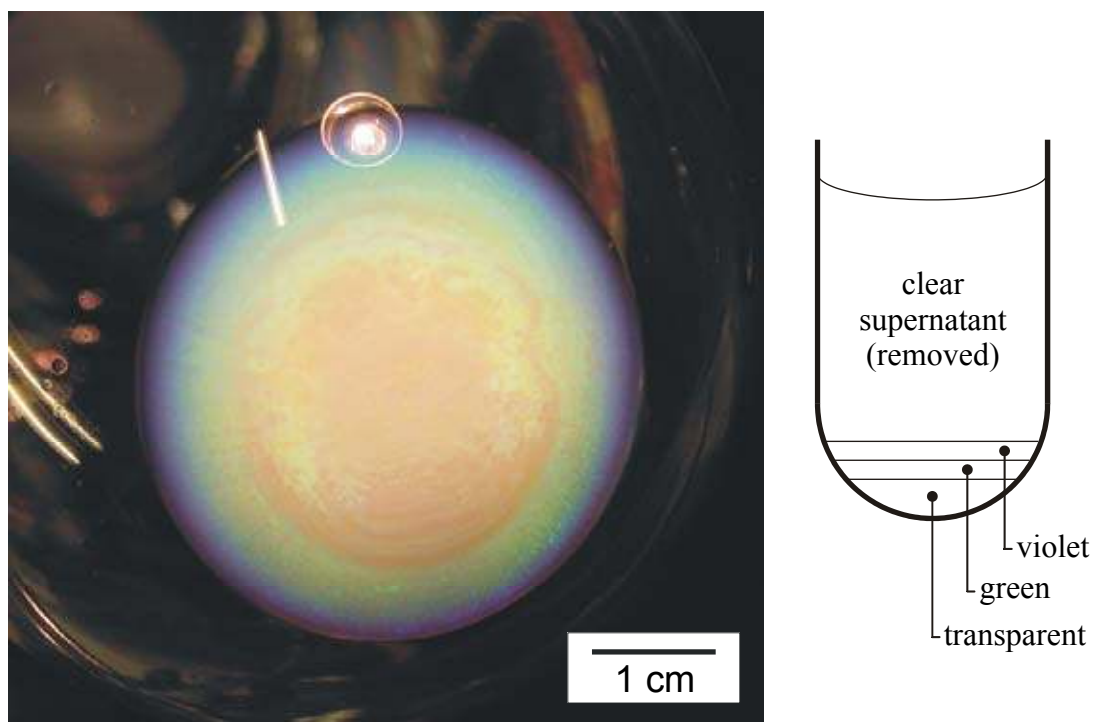


Figure 9.1 – The preparation of charge-stabilised gibbsite platelets involves a sequence of sedimentation and redispersion to remove excess Al_{13} ions. After the first sedimentation step the sediment, as depicted from below on the photograph, shows bright green and violet Bragg reflections, indicative of the columnar phase. The bottom part is a transparent glass-like layer.

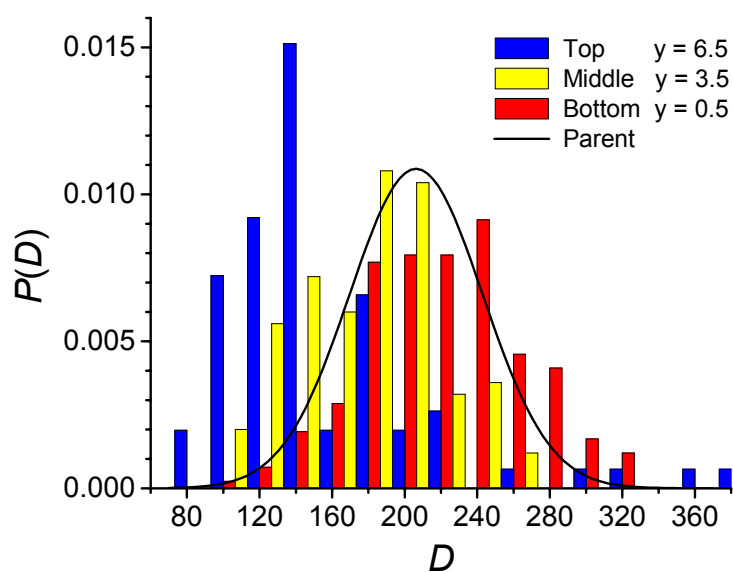


Figure 9.6 – Particle diameter distributions of the three studied sediment fractions as well as the parent suspension (Gaussian fit).

Enkele gedachten achteraf

Tja, daar sta je dan. Zo'n viereneenhalf jaar onderzoek samengeperst in één boekje. Met het risico van commentaar van de moeders in mijn omgeving, wil ik toch wel van een geboorte spreken als het gaat om het gereedkomen van dit proefschrift. Maar, in tegenstelling tot bijvoorbeeld de geboorten van Sam en Tijn is dit er een waarbij meerdere personen de weeën hebben moeten doormaken.

Laat ik als eerste 'geestelijk vader' mijn promotor noemen. Henk, ik ben je dankbaar voor de inzet waarmee je mij de afgelopen jaren hebt begeleid. Je betrokkenheid en enthousiasme hebben mij enorm gestimuleerd en zonder jouw inbreng, op allerlei momenten in mijn onderzoek, was dit proefschrift er niet geweest. De laatste maanden voor de deadline waren hectisch. Ik ben je dan ook zeer erkentelijk voor de tijd die je steeds wist vrij te maken. (Met dank aan het Maarnse thuisfront en de andere AiO's!) Je hebt mij verder de vrijheid gegeven om ouderschapsverlof op te nemen en de laatste twee jaar in deeltijd te werken. "Er is meer in het leven dan het werk" merkte je terecht op, en dat werd nog eens extra duidelijk toen je zelf opa werd van Max. Al met al zijn er de afgelopen jaren wel wat 'kleine wonderdjes' gebeurd en dit proefschrift hoort daar zeker bij.

De drie andere geestelijk vaders van dit werk zijn mijn co-promotoren; in alfabetische volgorde: Patrick, Andrei en Gert Jan.

Patrick, I would like to thank you for your commitment to the work described in this thesis. In particular, you have contributed to Part II on the magnetic field. I am not exaggerating to state that your input has been vital. I have really enjoyed the collaboration, especially during the stay in spring 2003. Thank you for your hospitality at the Laboratoire de Physique des Solides (LPS). I am looking forward to going to Paris again, hopefully we manage to get the Marie Curie fellowship!

Beste Andrei, ontzettend bedankt voor je hulp en bijdragen, in het bijzonder aan de hoofdstukken 2, 4 en 9. Zowel tijdens de meetsessies in Grenoble als tijdens de dataverwerking 'thuis' was je er om mij met SAXS-raad en daad bij te staan. De vele stimulerende discussies blijven mij zeker bij. Spaciba bolshoi!

Gert Jan, dankjewel voor scherpzinnige en kritische blik. Met name in de eindfase was die nodig om mijn stukken op een hoger niveau te brengen. Ik kan slechts hopen dat ik ooit zo kritisch leer zijn op eigen resultaten als jij.

Two other people with whom I had the pleasure to collaborate are Jacques Ferré and Jean-Pierre Jamet of the LPS. I would like to thank you for the opportunity to jointly perform the birefringence measurements that are the basis of Chapter 5 of this thesis.

Hoofdstuk 3 bevat de resultaten van computer simulaties uitgevoerd door Tanja Schilling. Tanja, ik wil je bedanken voor jouw bijdrage aan het hoofdstuk en ons gezamenlijk artikel. Onze contacten – zowel binnen als buiten het werk – heb ik erg prettig gevonden. Misschien dat wij dat nog eens een vervolg kunnen geven!

Enkele gedachten achteraf

De invloed van mijn kamergenoot Rik is terug te vinden in hoofdstukken 4 en 6 van dit proefschrift. Rik, je scherpe inzicht en razendsnelle berekeningen zorgden voor een snelle vooruitgang van het werk. Verder wil ik je bedanken voor de talloze momenten dat ik bij je terecht kon met vragen, met als hoogtepunt natuurlijk de vraag: “Wat is ook al weer de waarde van S_2 in de isotrope fase?”

Essentieel voor het totstandkomen van hoofdstuk 4 was de aanwezigheid van een supergeleidende magneet op de DUBBLE bundellijn in Grenoble en daarvoor komt Wim Bras de dank toe. Wim, bedankt voor je inzet en ondersteuning, zelfs toen de magneet de geest gaf. I would like to thank Igor Dolbnya, a former member of the DUBBLE crew. His expertise has been invaluable during the SAXS measurements.

Tijdens de afgelopen jaren zijn er enkele studenten geweest die hebben bijgedragen aan mijn onderzoek. René, Esther en Paul, bedankt voor de experimenten die jullie hebben uitgevoerd. Paul ziet zijn inzet beloond met een potentiële publicatie, maar dat betekent niet dat de meer exploratieve metingen van René en Esther minder interessant waren.

Van de Van 't Hoffers wil ik in het bijzonder Dirk, Roel en Stefano noemen. Mijn herinneringen gaan terug naar de studentenkamer, toen nog N731, naar een etentje in het IBB-complex en andere gezellige momenten. Jongens, bedankt! En voor de anderen: bedankt voor de gezelligheid en ondersteuning op allerlei vlakken.

Grafische ondersteuning kwam er van Jan, Alois en Ingrid van de Audiovisuele Dienst Chemie. Jullie hebben mijn posters steeds weer bijzonder strak vormgegeven, bedankt!

Aan het eind van deze gedachtegang kom ik natuurlijk bij mijn familie, in meerdere of mindere mate ook ‘geestelijk ouders’ van dit proefschrift. Papa en mama, jullie invloed op dit proefschrift is misschien minimaal, toch hebben jullie mij in de gelegenheid gesteld om ‘gewoon’ naar school te gaan en ‘gewoon’ te gaan studeren, kortom, de mogelijkheid gegeven om te doen wat ik voor ogen had. Bedankt!

Lieve Mieke, als moeder van Sam en Tijn hoef ik je niet te vertellen wat weeën zijn. Ook de barensweeën van dit boekje heb je van zeer dichtbij ondervonden en daarom mag jij de eerste zijn om mee te delen in het plezier van deze geboorte. Ik ben je heel erg dankbaar voor je steun, in het bijzonder gedurende de laatste maanden en ik zie er naar uit om met jou het buitenlands avontuur te beginnen.

Lieve Sam en Tijn, tegen de tijd dat jullie dit lezen ligt 2005 waarschijnlijk al weer ver achter ons. Jullie geboorte was voor mij lang niet zo'n werk als het schrijven van dit boekje, maar heeft voor mij veel meer betekend en nog steeds is jullie aanwezigheid heel bijzonder. Ik heb ontdekt dat het – frustrerend genoeg – onmogelijk is om alles in je leven 100% goed te doen en ik hoop daarom dat jullie, samen met alle anderen om mij heen, toch op z'n minst een redelijk deel van mijn toewijding hebben mogen ervaren... en dit geldt ook voor mijn eigen geestelijk Vader. Eigenlijk is er maar Een zonder wie dit proefschrift er niet zou zijn geweest!

Curriculum Vitae

De schrijver van dit proefschrift zag op dinsdag 7 december 1976 in Sleeuwijk het levenslicht. Hij behaalde zijn VWO-diploma aan het Altena College aldaar en ging daarna, in september 1995, Scheikunde studeren aan de Universiteit Utrecht. In september 2000 haalde hij het doctoraalexamen, met als bijvakken Chemiedidactiek en Computational Physics en als hoofdvak Fysische en Colloïdchemie. Het afstudeeronderzoek betrof een studie naar het fasegedrag van een polydispers systeem van colloïdale plaatjes, waarmee zijn interesse voor de colloïdchemie en -fysica was gewekt.

In oktober 2000 begon hij zijn promotieonderzoek aan het Van 't Hoff Laboratorium voor Fysische en Colloïdchemie van de Universiteit Utrecht op een project gefinancierd door NWO/CW, met als hoofdthema “Colloïdale plaatjes in externe velden”. De hieruit voortvloeiende resultaten zijn beschreven in dit proefschrift, gepubliceerd in vakbladen en gepresenteerd op diverse internationale congressen. De metingen die ten grondslag liggen aan Hoofdstuk 5 van dit proefschrift werden uitgevoerd aan het Laboratoire de Physique des Solides van de Université Paris-Sud in Frankrijk, waarvoor de auteur een maand in Parijs verbleef. Tot oktober 2005 zal hij als post-doctoraal medewerker in dienst zijn van het Van 't Hoff Laboratorium.